Institutt for fysikk og teknologi

Production of strange particles in lead-lead interactions at 158 A GeV/c

by

Kristin Fanebust Hetland

October 2005

Universitetet i Bergen

Bergen, Norway

Institutt for fysikk og teknologi

Production of strange particles in lead-lead interactions at 158 A GeV/c

by
Kristin Fanebust Hetland

a thesis submitted to
Institutt for fysikk og teknologi, Universitetet i Bergen,
in partial fulfilment of the requirements for
the degree of Doctor Scientiarum

October 2005
Universitetet i Bergen
Bergen, Norway

ISBN 82-497-0004-X

Abstract

A new phase of strongly interacting matter consisting of deconfined quarks and gluons has been predicted to exist at very high energy densities. This matter is referred to as a quark gluon plasma. The universe probably went through a quark gluon plasma phase shortly after the "Big Bang". The densities of some neutron stars are large enough for a quark gluon plasma to exist in the core of the stars. In the laboratory, sufficiently high energy densities for a quark gluon plasma to be formed are obtained in relativistic heavy ion collisions. Experiments searching for the new phase of matter and analysing its properties are performed at CERN outside Geneva, Switzerland and at BNL outside New York, USA.

Enhanced production of strange particles is one of the expected observables from a quark gluon plasma. The WA97 collaboration at CERN has measured the production of strange particles (K^0_S, Λ, Ξ and Ω) at central rapidities and high transverse momenta in heavy ion collisions compared to proton induced reactions. Strangeness is found to be enhanced in lead-lead collisions at 158 A GeV/c compared to proton-beryllium and proton-lead collisions at the same beam momenta. The enhancement is found to increase with increasing strangeness content of the particle, up to about a factor 20 for the triply strange Ωs in central lead-lead collisions. The NA57 collaboration extended the WA97 measurements by studying more peripheral collisions and collisions also at 40 GeV/c per nucleon, searching for the *onset* of the strange particle enhancement.

In this thesis, results from Pb-Pb collisions at beam momenta of 158 A GeV/c collected by the NA57 collaboration in 1998 are presented (chapter 5). The author's main contributions to the results are in the correction procedure presented in chapter 4 and in connection with this the examination of the difference in results from WA97 and NA57 presented in section 5.5, and the selection of Λ and $\overline{\Lambda}$ from the 158 A GeV/c lead-lead data sample collected in 1998, and the final analysis of these results (chapter 3 and 5). In chapter 1, a theoretical overview of the physics of relativistic heavy ion collisions is presented. The WA97 and NA57 experiments are described in chapter 2. A discussion of the results of this thesis, and a comparison to other results from the NA57 experiment and to results from other SPS and RHIC experiments, are found in chapter 6. Chapter 7 contains a summary of the WA97/NA57 results and an outlook for relativistic heavy ion physics.

Acknowledgements

The work presented in this thesis has been carried out in the WA97 and NA57 collaborations at CERN, during my period as a PhD student at the Department of Physics and Technology, University of Bergen, from 1996 to 2001, and has been finished with support from my present employer Bergen University College.

Most of all I thank my former supervisor Prof. Tor Fredrik Thorsteinsen. Without his support I would never have started this project. In addition to being an excellent supervisor he also became a good friend, and he has been greatly missed since he passed away in 1999. I would also like to thank his wife Unni for her kind hospitality.

I also thank my present supervisors, Prof. Gunnar Løvhøiden, Prof. Håvard Helstrup and Prof. Dieter Röhrich, for strongly encouraging me to finish this project. They have also been a great help with improving the quality of this thesis.

It has been a pleasure to work in the WA97 and NA57 collaborations, and I would like to thank all the people who took part in the experiments during these years. There are many nice night shifts to remember! A special thank to the spokesmen, Dr. Emanuele Quercigh and Dr. Federico Antinori, for their guidance and stimulating discussions. I would also like to mention Dr. Nicola Carrer and Dr. Giuseppe Bruno who have always been very helpful, answering all my questions about the analysis. It is also a pleasure to thank Michael, Eugenio, Iztok, Alex, Peter and Luitwin from the RD19 collaboration for all the nice coffee breaks and numerous trips *away* from CERN during my many stays there. CERN is not the same without you!

My thanks also to all the Master and PhD students in experimental nuclear physics at the University of Bergen and the University of Oslo for making my studies enjoyable. I have many good memories from travels to CERN, from conferences around the world and from the everyday life at the Physics Department in Bergen. I would especially like to mention Dr. Alv Kjetil Holme, Dr. Odd Harald Odland and Dr. Jørgen Lien.

During the last four years I have had the pleasure to work at Bergen University College. I would like to thank all my colleges there for the nice working environment, and especially Petter Seip whom I have had the pleasure to teach several courses together with.

I would like to thank my parents for always supporting me and for being such excellent babysitters! Finally, I thank my husband Sverre and my two lovely children, Gabriel and Johanna, for all their love and support!

Bergen, October 2005
Kristin Fanebust Hetland

Contents

List of Figures

List of Tables

Chapter 1

The Quark Gluon Plasma

The word "atom" originates from the Greek word "atomos", which means indivisible. The Ancient Greeks believed in the existence of a single, indivisible particle being the building block of the Universe. Much later, the atoms we know today were discovered and were believed to be such indivisible building blocks in nature. In the early part of the 20th century, discoveries revealed that the atom is not an elementary particle after all, but consists of a positively charged nucleus and negatively charged electrons orbiting the nucleus. The nucleus itself was later found to be composed of protons and neutrons. Electrons, protons and neutrons were the new elementary particles, believed to be indivisible. From the middle of the 1940s, many new sub-atomic particles were discovered by studying collisions between known particles at high energy. The new particles were found to be very unstable with short lifetimes. Until the 1960s, physicists were confused by the large number and variety of subatomic particles being discovered. They were trying to find a pattern that would provide a better understanding of the variety of particles.

1.1 Quarks and gluons

In 1964 quarks were introduced independently by Gell-Mann [1] and Zweig [2] as building blocks of hadronic matter. As far as we know today, quarks are indivisible elementary particles. Hadrons are divided into two groups. One group called baryons, consisting of three quarks (qqq) like protons and neutrons. The other group called mesons, consisting of a quark-antiquark pair ($q\overline{q}$) like pions and kaons. Quarks are found in six different flavours, all having spin $\frac{1}{2}$, as shown in table 1.1. The electric charges are given in the table in units of the electron charge, $|e|$. Antiquarks ($\overline{q}$) have the same masses, but opposite electric charges ($-\frac{2}{3}|e|$ or $+\frac{1}{3}|e|$). Particles seen in nature always have a net charge of $n|e|$, where $n = \pm 0, 1, 2, \ldots$ Some examples of particles and their quark contents are given in table 1.2. The corresponding antiparticles have antiquarks instead of quarks, and opposite electric charges. The mass of an antiparticle is the same as for the corresponding particle.

In addition to the electric charge, quarks have a colour charge responsible for the strong interaction. There are three different colour charges, called red, green and blue, and their corresponding anti-colours. A baryon consists of a red, a green and a blue quark to form a colour-neutral (white) particle, while a meson is composed of a colour and its

Quark Flavour	Electric charge/$\lvert e\rvert$	Mass [MeV/c^2]
u (up)	$+\frac{2}{3}$	1.5 - 4
d (down)	$-\frac{1}{3}$	4 - 8
s (strange)	$-\frac{1}{3}$	80 - 130
c (charm)	$+\frac{2}{3}$	1150 - 1350
b (bottom)	$-\frac{1}{3}$	4100 - 4400
t (top)	$+\frac{2}{3}$	$(174.3 \pm 5.1) \cdot 10^3$

Table 1.1: Quark flavours, their relative electric charges and masses [3].

Particle	Quark content	Mass [MeV/c^2]	Electric charge/$\lvert e\rvert$
p	uud	938.27203 ± 0.00008	+1
n	udd	939.56536 ± 0.00008	0
π^+	$u\overline{d}$	139.57018 ± 0.00035	+1
π^-	$\overline{u}d$	139.57018 ± 0.00035	-1
K^0	$d\overline{s}$	497.648 ± 0.022	0
K^+	$u\overline{s}$	493.677 ± 0.016	+1
K^-	$\overline{u}s$	493.677 ± 0.016	-1
Λ	uds	1115.683 ± 0.006	0
Ξ^-	dss	1321.31 ± 0.13	-1
Ω^-	sss	1672.45 ± 0.29	-1

Table 1.2: Example of particles and their quark contents, masses and electric charges [3].

anti-colour quark-antiquark pair, also giving a net colour of white. Only colour-neutral particles exist in nature.

In Quantum Electrodynamics (QED), the field theory of electromagnetic interactions, particles interact by exchanging photons. The photons themselves have no electric charge, and therefore do not interact with each other. The field theory describing strong interaction is called Quantum Chromodynamics (QCD). The quarks interact strongly by exchanging gluons. The gluons are massless and have spin 1, like the photons, but while the photons have no electric charge, the gluons themselves carry colour charge and can thereby interact with quarks and other gluons.

The potential between two quarks at a distance r is of the form

$$V(r) \sim -\frac{\alpha_s(r)}{r} + kr \tag{1.1}$$

where k is a constant and $\alpha_s(r)$ is the strong coupling constant. At short distances, the first term in the potential dominates, and the potential looks similar to the electromagnetic potential between two electric charges. The fact that gluons are coloured means they can interact with each other, causing the lines of colour charge connecting two separating quarks to be stretched and grouped together to form a *string*. Therefore, at larger

distances, $r \gtrsim 1$ fm (10^{-15} m), the second term in equation 1.1 dominates and $V(r) \to \infty$. The constant k can be thought of as a spring constant providing the tension in the string. This property of the strong force binds quarks together into hadrons. A quark can only exist close to other quarks, making the net colour charge of the composite object zero. This is referred to as *QCD confinement*.

When two quarks are forced to separate, it becomes energetically favourable to break the colour string and produce a quark-antiquark pair. Two new colour neutral objects are created from the original colour neutral object. This is the reason why no *free* quarks are observed at normal temperatures and densities.

At very small distances, $r \to 0$, the coupling between the quarks becomes small, $\alpha_s(r) \to 0$. The potential between the quarks decreases with the distance and at infinitely small distances the quarks are considered to be free. This is called *asymptotic freedom*.

1.2 Hot and dense nuclear matter

The observation that QCD is an asymptotically free theory, led to the suggestion that a critical behaviour at high temperature and/or density is related to a phase transition [4]. The phase transition between confined and deconfined matter is expected to happen at a critical temperature and energy density. Below this limit quarks are confined and only hadronic matter can be observed. Above the critical temperature and energy density quarks are no longer confined in hadrons and we have a new state of matter called quark gluon plasma (QGP). In this state, quarks and gluons can be seen as *free* particles. At high temperature and/or baryon density, QCD is characterized by an approximate chiral symmetry which is a symmetry between right handed and left handed terms in the Lagrangian. The symmetry is exact only at vanishing quark masses. At normal temperature and baryon density, this chiral symmetry is spontaneously broken and the quark masses originate as a direct consequence of this mechanism.

If we look for quark gluon matter in nature, we expect to find it in the early universe where the temperature is extremely high, and in the core of neutron stars where the density is above the critical density, but with a low temperature. To study the phase transition in the laboratory, the only possibility is to study collisions between heavy ions at relativistic energies. Relativistic heavy ion collisions are described in section 1.3.

The strong coupling constant, α_s, increases with distance or, correspondingly, decreases with momentum transfer. For *hard processes*, i.e. processes with large momentum transfer and small α_s, perturbative QCD calculations can be applied. The *soft processes* which have small momentum transfer and large α_s, can not be described by perturbative QCD. One way to overcome this problem is to calculate QCD on a discrete lattice in space and time. Lattice QCD makes use of Monte Carlo techniques and is therefore ideal for numerical calculations on powerful computers. To get good results, a high density of space-time points is needed. Due to limited computer power, calculations so far have been done only on limited topics and mostly assuming massless particles or zero net-baryon density, i.e. vanishing baryochemical potential. Lately, lattice calculations at finite chemical potential (e.g. [5] and references therein) have been performed.

If the u, d and s quarks are assumed to have physical values of their masses, lattice QCD calculations at zero chemical potential indicate that there is a rapid crossover

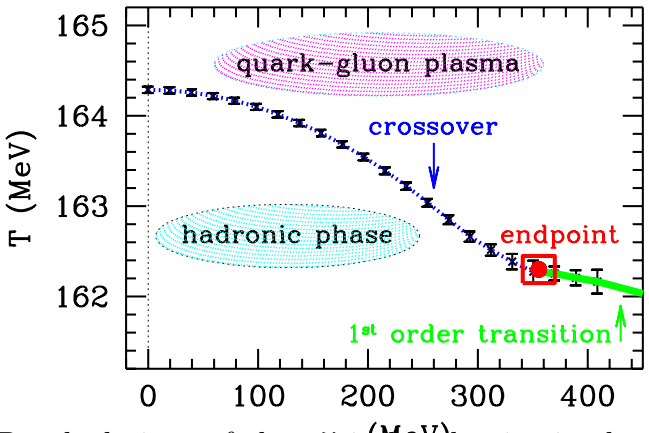

Figure 1.1: Lattice QCD calculations of the critical end-point in the QCD phase diagram [6].

between hadronic and quark gluon matter [5] around a critical temperature of about 165 MeV [6]. In a crossover the observables change rapidly, but no singularities appear. At large chemical potential and finite temperature, a first order phase transition is predicted by several models [5]. A first order phase transition leads to a discontinuity of the energy density, $\epsilon(T)$. To combine the first order phase transition at large chemical potential with the crossover at zero chemical potential, a critical end-point is introduced. At this point the phase transition is expected to be of second order, meaning that the second derivative of the free energy, the specific heat, is discontinuous. Recent calculations estimate the temperature, T, at the critical point to be around 162 MeV, and the chemical potential, μ_B, to be around 400 MeV [6] (see figure 1.1).

Figure 1.2 shows a phase diagram of QCD. In the left figure, the solid line indicates a first order transition from hadronic to quark gluon matter at high baryochemical potential μ_B, and the long-dashed line indicates a crossover region at low μ_B. The short-dashed line indicates a phase transition between normal and colour superconducting quark gluon matter (not discussed in this thesis). The right figure shows the prediction for the transition from hadronic matter to quark gluon matter calculated from lattice QCD, together with the experimentally measured chemical freeze-out parameters. The freeze-out curve is a fit to the datapoints. The experimental freeze-out parameters originates from the final stage of the expansion of the hot collision zone, and the baryochemical potential is therefore assumed to be higher at an earlier stage. As can be seen from the figure, the QCD phase diagram has been explored by using different collision energies. Higher collision energies leads to increased temperatures and a lower baryochemical potential. Values of $\mu_B \approx 400$ MeV, where the location of the critical end-point has been predicted, can be explored by using beam momenta around 40 A GeV/c [7].

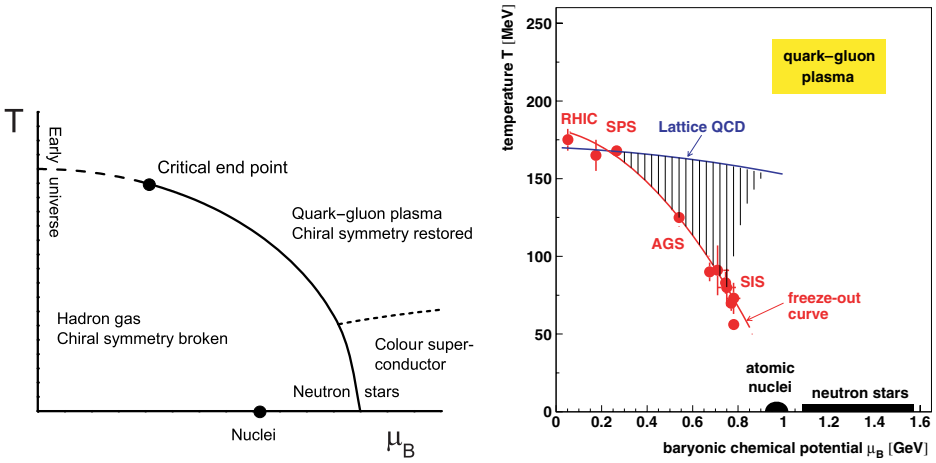

Figure 1.2: The QCD phase diagram [7].

1.3 Heavy ion collisions

Colliding heavy ions is the only way to produce sufficiently high temperatures and densities for a quark gluon plasma to be formed in the laboratory. Figure 1.3 illustrates the geometry in a heavy ion collision. Two nuclei collide with an impact parameter, b, defined as the distance between the centres of the colliding nuclei measured perpendicular to the beam axis. Nucleons in the overlapping region are called participants, while the remaining nucleons are called spectators. The participants form a hot and dense fireball that interacts strongly, while the spectators lose some of their original momenta but continue away from the hot collision zone. Head-on collisions, with an impact parameter close to zero, have the maximum number of participants, and the maximum size and density of the fireball. If the volume and the lifetime of the fireball are sufficiently large, the system can reach a state of thermal equilibrium, and a quark gluon plasma may be formed if the energy density is above the critical value.

A quark gluon plasma is most likely to be formed in central collisions, i.e. when the impact parameter is small. Unfortunately, the impact parameter can not be measured directly in an experiment, so the centrality has to be estimated from other measurable quantities. Such quantities are for instance the number of charged particles produced in the collision or the transverse energy. A central collision produce more charged particles and give higher transverse energy than a peripheral collision. The number of participants can be estimated from the measured quantity using for instance a Glauber model. (See section 5.2 for a description of the method used by WA97 and NA57.)

The main facilities for studying heavy ion collisions are localized at BNL (Brookhaven National Laboratory) in the USA, and at CERN (European Organization for Nuclear Research) outside Geneva, Switzerland. The accelerators at the two laboratories provide different energy regimes, from the AGS (Alternating Gradient Synchrotron) at BNL, via

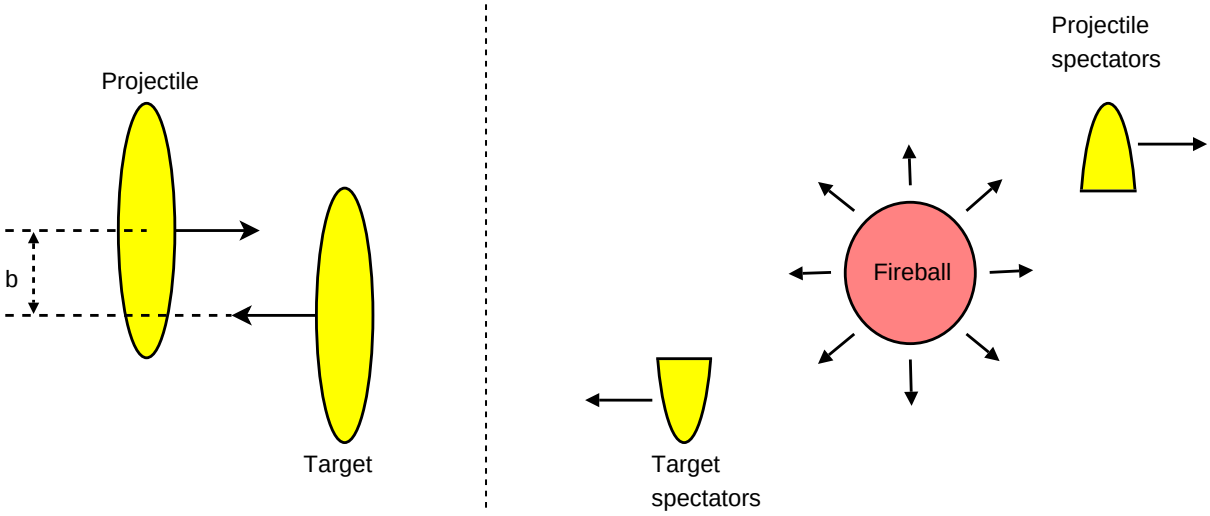

Figure 1.3: Geometric illustration of a heavy ion collision, before the collision (left) and after the collision (right). The projectile collide with the target with an impact parameter b. The illustration is made in the center-of-mass system.

the SPS (Super Proton Synchrotron) at CERN, to RHIC (Relativistic Heavy Ion Collider) at BNL. In the future, heavy ion collisions will also be studied at the LHC (Large Hadron Collider) at CERN. The RHIC and the LHC are colliders, with two beams accelerated in opposite directions and collided with each other. In the other accelerators the beam impinges on a fixed target. The accelerator facilities and their maximum energies for the heaviest accelerated ions are summarized in table 1.3.

Accelerator	Heaviest ions	Max. p_{beam}/A (GeV/c)	Max. $\sqrt{s_{NN}}$ (GeV)
AGS	Au	10.7	4.7
SPS	Pb	158	17.3
RHIC	Au	100	200
LHC	Pb	2750	5500

Table 1.3: Accelerator facilities for heavy ions.

1.3.1 Kinematic variables

When describing the kinematics of relativistic heavy ion collisions, it is convenient to use quantities that are invariant under Lorentz transformations. The movement of a particle along the beam axis can be described in terms of the Lorentz additive parameter rapidity, y, rather than velocity or longitudinal momentum. Rapidity is defined as

$$y = \tanh^{-1}\left(\frac{v_{\mathrm{L}}}{c}\right) = \frac{1}{2}\ln\left(\frac{E + p_{\mathrm{L}}c}{E - p_{\mathrm{L}}c}\right) \tag{1.2}$$

where E is the energy of the particle, v_{L} is the velocity of the particle along the beam axis, p_{L} is the momentum of the particle parallel to the beam axis, and c is the speed

of light in vacuum. In the nonrelativistic regime rapidity is numerically close to the value of the speed in units of c. A rapidity distribution has the same shape in the laboratory and the centre-of-mass systems, only the absolute values are shifted. The rapidity distribution for different particles gives information about where the particles originate from. Target spectators have a rapidity close to the target rapidity, $y_{\mathrm{lab}} = 0$ in a fixed target experiment, while spectators from the beam have a rapidity close to the rapidity of the beam. Particles from the fireball, the participants, have a rapidity close to the rapidity of the centre-of-mass.

At relativistic energies ($E \gg m$) rapidity can be approximated by pseudorapidity, η, which is independent of the mass of the particle, and therefore independent of particle type. This is useful when no particle identification is available. Pseudorapidity is defined as

$$\eta = -\ln \tan\left(\frac{\theta}{2}\right) \tag{1.3}$$

where θ is the angle between p_{L} and the total momentum p.

When transformations are made along the beam direction, the momentum of a particle transverse to the beam axis, p_{T}, is also invariant under Lorentz transformations. Another frequently used parameter is the transverse mass, m_{T}, defined as

$$m_{\mathrm{T}} = \sqrt{p_{\mathrm{T}}^2 + m^2} \tag{1.4}$$

where m is the mass of the particle, and $c = 1$. The temperature of the system can be extracted from the transverse mass distribution (see e.g. section 1.4.1).

1.3.2 Nuclear stopping

When two nucleons interact they lose kinetic energy. The loss of kinetic energy is referred to as *stopping*. The kinetic energy is deposited in a small volume giving a large energy density. The amount of stopping increases with increasing number of nucleon-nucleon collisions.

At relatively low energies, like at AGS, the nucleons pile up at mid-rapidity, leaving a baryon rich interaction zone. This scenario resembles the picture of the hydrodynamical Landau model [8]. At high energies, like at RHIC, or at the future LHC, the nuclei manage to escape from the interaction region even if the energy loss due to nucleon-nucleon collisions is very high. In this case the interaction zone has a large energy density, but is almost baryon free. Such transparent interactions are described by the hydrodynamical Bjorken model [9].

The net-baryon rapidity distribution gives information about nuclear stopping. In a model assuming full stopping, like the Landau model, a gaussian rapidity distribution around the central rapidity is expected. In the other extreme, assuming full transparency like the Bjorken model, the central rapidity distribution for net-baryons is assumed to be zero, i.e. vanishing baryochemical potential. Experimental results showing rapidity distributions of net-protons from central heavy ion collisions at AGS, SPS and RHIC at centre-of-mass energies of 4.7, 17.3 and 200 GeV respectively, are shown in figure 1.4. The figure indicates that the Landau model can be applied at AGS energies. At SPS energies, there is a dip in the centre of the distribution indicating some degree of transparency.

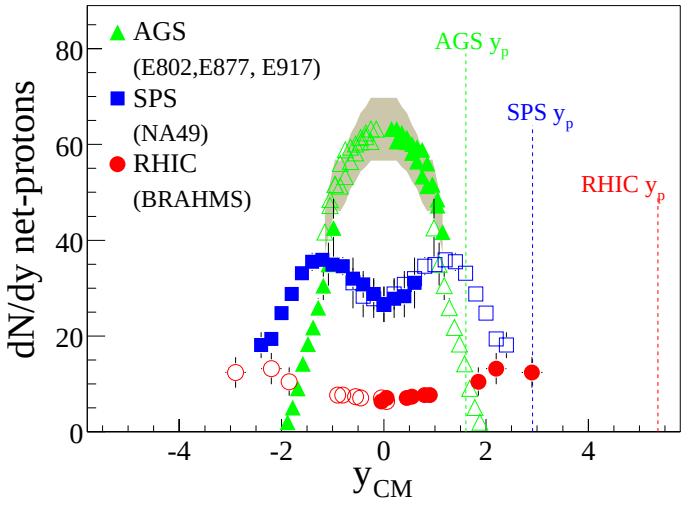

Figure 1.4: Rapidity distributions for net-protons at AGS, SPS and RHIC energies [10]. y_p is the rapidity for the incoming projectile.

A broad minimum spanning several units of rapidity indicates that collisions are quite transparent at RHIC energies.

1.3.3 Evolution in space and time

An illustration of the evolution of a heavy ion collision in space and time, assuming that the system goes through a quark gluon plasma phase, is shown in figure 1.5. Initially there is a pre-equilibrium phase dominated by hard scatterings. As the particles interact, the temperature increases and exceeds the critical temperature, T_c, where a transition to a quark gluon plasma is expected. As the quark gluon plasma cools down, it eventually again reaches the critical temperature T_c and a transition into a hadron gas takes place. In this phase, elastic and inelastic interactions change the kinetic properties of the particles and the particle composition of the system. As the system expands, the density decreases and the particles eventually stop interacting. This defines the freeze-out of the particles. It is distinguished between chemical and kinetic freeze-out. When the particle composition is no longer changed by inelastic interactions, it is called chemical freeze-out (T_{ch}). A thermal freeze-out (T_{fo}) happens when the kinematic distributions are no longer changed by elastic interactions. Different particles may freeze-out at different times. The particles after freeze-out can be observed experimentally.

1.4 Experimental observables

The lifetime of a quark gluon plasma is expected to be in the order of a few fm/c, or about 10^{-23} seconds. The only way to retrieve information about the QGP phase, is to detect and analyse the final state particles that are frozen out from the hot collision zone, or direct photons or dileptons that are not affected by final state interactions. Experimental

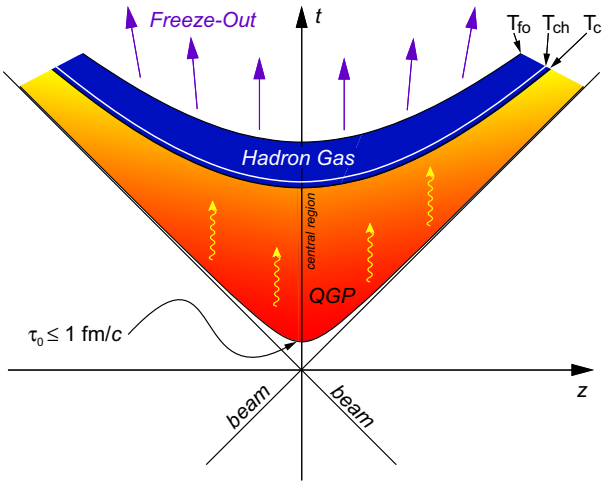

Figure 1.5: Space-time evolution of heavy ion collisions assuming that the system passes through a QGP phase [11].

observables from a quark gluon plasma are compared to predictions from different models describing heavy ion collisions.

The different experimental observables give information about different stages of the collision. Some observables are weakly affected by the interactions that take place after the collision, and can therefore give important information about the early stage of the collision. Other signals are related to the chemical or the thermal freeze-out. Some experimental observables are discussed in the following sections.

1.4.1 Temperature and radial flow

Hagedorn first introduced the connection between the freeze-out temperature of a thermal source and the transverse mass [12]. In p-p collisions the transverse mass spectra of all produced particles can be described using one common inverse slope, T, by the equation

$$\frac{1}{m_{\mathrm{T}}}\frac{\mathrm{d}N}{\mathrm{d}m_{\mathrm{T}}} \propto \exp(-\frac{m_{\mathrm{T}}}{T}) \tag{1.5}$$

In p-p collisions the inverse slope is interpreted as the temperature of the system. Going to nucleus-nucleus collisions this picture is more complicated, and the inverse slope parameter can no longer be directly interpreted as the temperature of the system. In A-A collisions T is found to increase with the particle mass [13], as can be seen in figure 1.6. This effect can be interpreted as a common transverse flow of all particles in the source in addition to the thermal motion [14]. If the source expands with a common transverse velocity, the transverse mass of the particles is higher for heavier particles. An exception is observed for the multistrange particles Ξ and Ω. Their inverse slopes fall below the line drawn through the π, K and p points. This has been interpreted as an early freeze-out of multistrange hadrons [15].

Statistical models can describe the final state of high energy collisions using a small number of macroscopic parameters. It is assumed that the final state is in thermal and

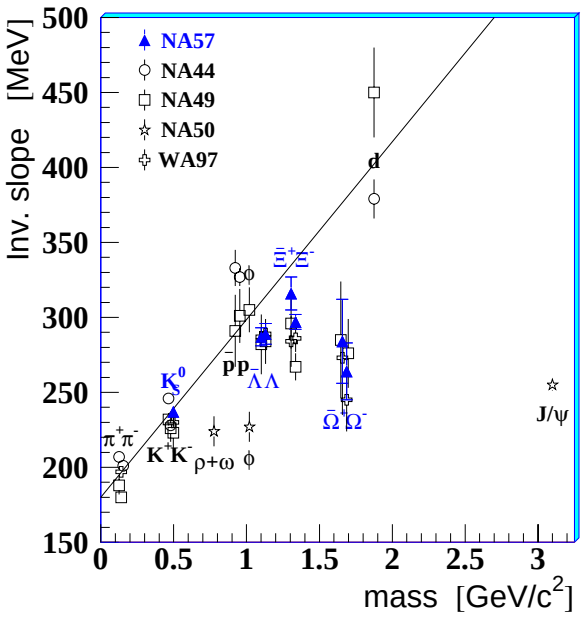

Figure 1.6: Inverse slopes as a function of the particle rest mass in Pb-Pb interactions at 158 A GeV/c [16]. The line through the π, K and p points are drawn to guide the eye.

chemical equilibrium and that it can be described using thermodynamics. The models describe the system as a whole, but the information about single particles is lost.

The statistical hadronization model in [14] also describes the m_{T} distributions. The model assumes that particles decouple from a system in local thermal equilibrium with temperature T. The system is assumed to expand both in the longitudinal and in the transverse direction. Two parameters can be extracted from a fit of the model to the experimental spectra, the thermal freeze-out temperature T and the average transverse flow velocity $\langle\beta_{\perp}\rangle$. The model is often referred to as the *Blast-wave model*.

Results from the STAR experiment at RHIC are shown in figure 1.7 [17]. Blast-wave fits for π, K and p are shown for 9 different centrality classes, class 1 being the most central class. They observe that the temperature decreases with centrality, while the average transverse flow is increasing. This may indicate a more rapid expansion in central collisions compared to peripheral collisions. For the most central class they observe an average transverse flow of about $0.6c$ and a freeze-out temperature around 90 MeV. Fits for the particles ϕ and Ω, containing only strange quarks, are shown for the most central class. The fits have large uncertainties but indicate that these particles freeze out at a higher temperature and with a lower average transverse flow than the other particles. The thermal freeze-out temperature of ϕ and Ω are close to the chemical freeze-out temperature calculated by statistical models, while their average transverse flow is about $0.5c$. This suggests that the particles with no quarks in common with the colliding nucleons decouple almost immediately after hadronization, but already with a significant amount of radial flow. The flow must be accumulated prior to chemical freeze-out, maybe in a partonic phase.

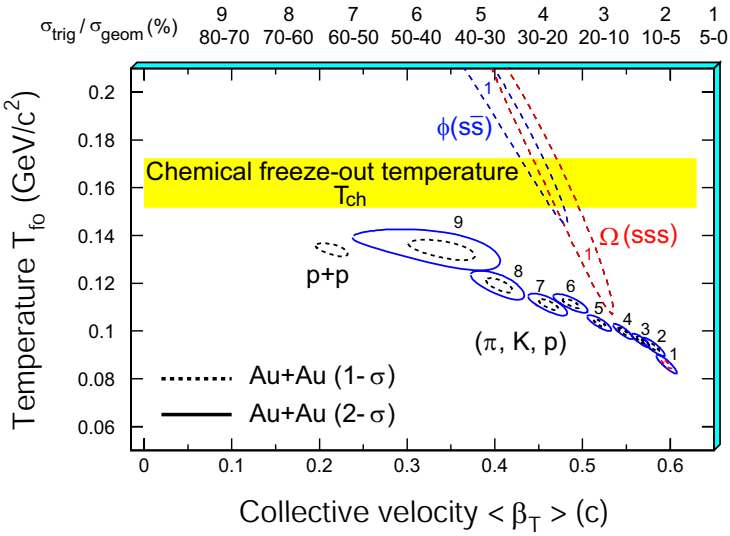

Figure 1.7: Blast-wave fit to the m_{T} spectra measured by STAR at $\sqrt{s_{NN}} = 200$ GeV Au-Au collisions [17]. The numerical labels above the plot indicate the centrality selection (9 classes). Results for π, K, and p are shown for 9 centrality classes. For ϕ and Ω, only the most central results are shown. Results from p-p collisions are also shown. The chemical freeze-out temperature at about 160 MeV is indicated by the yellow (shaded) band.

1.4.2 Directed and elliptic flow

Pressure gradients within the fireball leads to collective motion or flow. Flow can be described by hydrodynamical models assuming an initial system in equilibrium. To be able to describe the system in terms of thermodynamical quantities, it has to be established that the particles undergo enough interactions to reach thermal equilibrium.

The overall azimuthal angular distribution with respect to the reaction plane can be expressed as the Fourier series [18]

$$E\frac{\mathrm{d}^3N}{\mathrm{d}^3p} = \frac{1}{2\pi}\frac{\mathrm{d}^2N}{p_{\mathrm{T}}\mathrm{d}p_{\mathrm{T}}\mathrm{d}y}\left(1 + \sum_{i=1}^{\infty} 2v_n \cos[n(\phi - \Psi_r)]\right) \tag{1.6}$$

where ϕ is the azimuthal angle of the outgoing particle compared to the reaction plane Ψ_r. The reaction plane is defined by the beam axis and the impact parameter. The Fourier coefficients, $v_n = \langle\cos[n(\phi - \Psi_r)]\rangle$ (n denotes the harmonic), is calculated as the mean over all particles in all events.

The first Fourier coefficient, v_1, is referred to as *directed flow*. It describes the sideward motion of the fragments in ultra-relativistic nuclear collisions. The amount of directed flow is closely related to the equation of state (EoS) of the matter. Creation of a quark gluon plasma leads to a softening of the EoS and less directed flow. As a consequence of the softer EoS a *wiggle* effect has been predicted around central rapidity [19] where the quark gluon plasma is expected to be formed. Directed flow has been measured by STAR at $\sqrt{s_{NN}} = 200$ GeV [20] and by NA49 at $\sqrt{s_{NN}} = 17.3$ GeV [21] as a function of pseudorapidity. The pseudorapidity dependence of v_1 in the target/projectile fragmentation regions are found to be very similar at RHIC and SPS energies. At mid-rapidity the RHIC

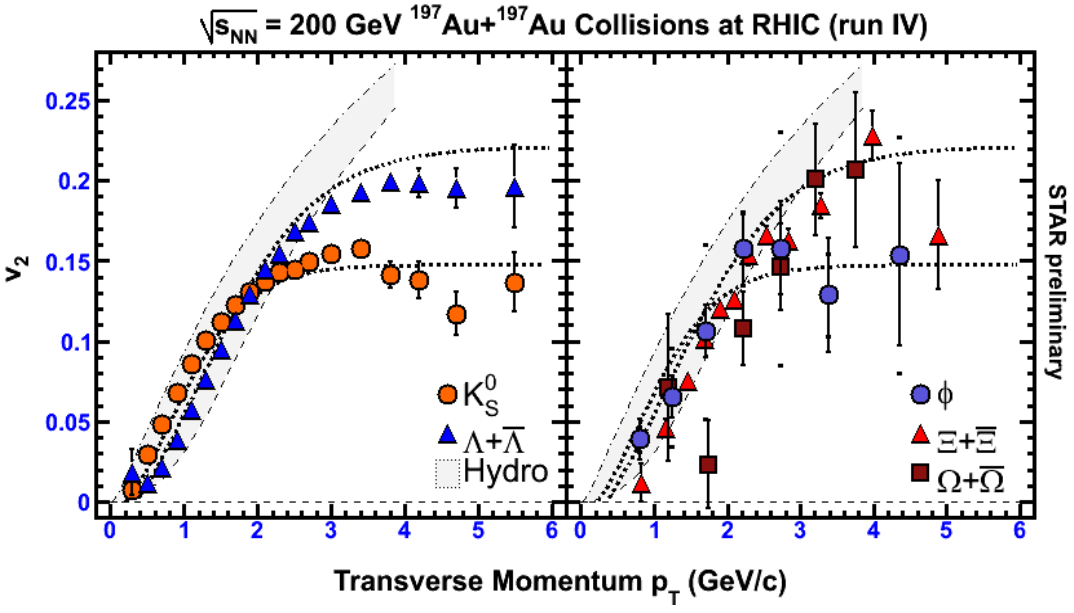

Figure 1.8: Elliptic flow near mid-rapidity in Au-Au collisions at $\sqrt{s_{NN}} = 200$ GeV as a function of p_{T} [23]. Experimental results are compared to hydrodynamical calculations.

data are much flatter than the SPS data. STAR has also measured the directed flow at $\sqrt{s_{NN}} = 62.4$ GeV [22]. At this energy v_1 is not completely flat around mid-rapidity, but shows a slower decrease than in the forward region. No v_1 wiggle effect is observed around central rapidity, but can not be ruled out due to statistical uncertainties. As expected, directed flow is found to decrease with the centrality of the collisions [22].

The second Fourier coefficient, v_2, is referred to as *elliptic flow*. When two nuclei collide with non-zero impact parameter, the initial overlap region is spatially deformed (almond shaped). The particle momenta, however, are assumed to be azimuthally uniform. If the particles do not interact during the expansion of the source, the spatial asymmetry will have no effect on the momentum distribution and this will still be uniform. If the observed momentum distribution is asymmetric, this is evidence that the produced particles have interacted. In addition, it indicates that the interactions took place at an early stage, since the expansion of the source will more or less erase the spatial asymmetry. Elliptic flow for strange particles measured by the STAR experiment at RHIC [23] close to mid-rapidity is presented in figure 1.8. The data are compared to the predictions from a hydrodynamical model. It can be seen that the amount of elliptic flow at RHIC is close to the hydrodynamical limit even for strange particles, indicating a system in equilibrium at an early stage of the collision.

Figure 1.9 shows the elliptic flow at different energies. At the SPS the elliptic flow is about a factor two smaller than at RHIC (see e.g. [24] and references therein). This is lower than what has been predicted by hydrodynamical models. At even lower energies (SIS/Bevalac and lower AGS) the elliptic flow is negative. At these energies the target and projectile spectators are shadowing the emission of particles.

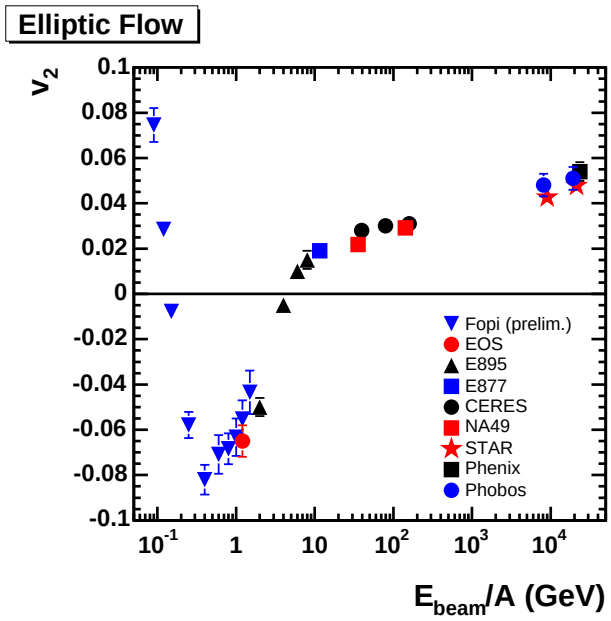

Figure 1.9: Elliptic flow of charged particles near mid-rapidity as a function of energy [24].

1.4.3 Interferometry

In the 1950s Hanbury-Brown and Twiss (HBT) developed a method for measuring the stellar radii by two-photon intensity interferometry [25]. In a similar way, identical particle interferometry, e.g. $\pi\pi$ correlations, gives information on the reaction geometry in a collision between particles [26]. The method exploits the fact that the probability of detecting two particles in coincidence is enhanced for small momentum differences between the particles. The size of the particle source can be related to the momentum range of this enhancement. In addition, HBT interferometry provides information about the lifetime and flow patterns of the fireball [27].

The correlation function for two pions can be expressed as

$$C_2(p_1, p_2) = \frac{P_2(p_1, p_2)}{P_1(p_1)P_1(p_2)} \tag{1.7}$$

where p_1 and p_2 are the four-momenta of the two pions, P_2 is the probability of detecting two pions with the corresponding momenta in the same event, and P_1 is the probability of detecting a single pion with the given momentum. If there is no correlation, $C_2 = 1$. The probability function can also be expressed as

$$C_2(q) = 1 + \lambda|\rho(q)|^2 \tag{1.8}$$

where $q = p_2 - p_1$ is the four-momentum difference and $\rho(q)$ is the Fourier transform of the space-time source density. The factor λ is introduced to correct for the fact that the source might not be completely incoherent.

Different parametrizations have been introduced for the correlation functions. One of them is the 'cartesian' Pratt-Bertsch parametrization [28, 29], expressed in the *out-side-longitudinal* system. The *longitudinal* direction is in the direction along the beam axis. In

the transverse plane the *out* direction is chosen to be parallel to the transverse component of the pair momentum, and the *side* direction is the remaining cartesian component.

HBT parameters are calculated as a function of the collision energy for mid-rapidity, low p_{T} $\pi^-\pi^-$ correlations from central Au-Au, Pb-Pb and Pb-Au collisions from AGS to RHIC energies [30]. None of the calculated radii are changing significantly in this energy regime. The longitudinal radius R_l increases slightly with increasing collision energy, reflecting a slightly larger freeze-out volume. The ratio between the *out* and the *side* direction is a sensitive probe of the equation of state in hydrodynamical models [31, 32]. For a hadronic scenario the ratio has been predicted to be $\sim 1.0 - 1.2$, while it has been predicted to be $\sim 1.5 - 10$ in a QGP scenario. The experimentally measured ratio is not increasing at RHIC energies compared to results at lower energies, and is compatible with the predictions for a hadronic scenario.

1.4.4 Strangeness

Enhanced production of strange particles in a quark gluon plasma compared to a hadron gas was suggested by Rafelski and others in the early 1980's [33, 34]. The mass threshold for production of strangeness in a quark gluon plasma is reduced compared to a hadron gas. In addition, there is a large abundance of gluons taking part in the production of strange-antistrange quark pairs.

The colliding nuclei contain only light quarks and no strange or antistrange quarks. All strange particles seen in the detectors are therefore produced in the collision. Since strangeness is a conserved quantity, a particle containing an anti-strange quark has to be produced whenever a particle containing a strange quark is produced. In hadronic matter, strangeness is for instance produced in these reactions:

$$\pi + \pi \rightarrow K + \overline{K} \qquad (Q = 2m_K - 2m_\pi \approx 710 \text{ MeV})$$

$$N + N \rightarrow N + \Lambda + K \qquad (Q = m_\Lambda + m_K - m_N \approx 670 \text{ MeV})$$

$$\pi + N \rightarrow K + \Lambda \qquad (Q = m_K + m_\Lambda - m_\pi - m_N \approx 530 \text{ MeV})$$

The values in parenthesis are the Q-values for the reactions, i.e. the threshold value for the energy needed to produce the new particles. In hadronic matter a multi-strange particle can be produced by first producing a singly-strange particle. The production of multi-strange particles therefore requires a long time scale in addition to high energy. At high densities, close to the phase boundary, multi-strange particles might be produced in multi-hadron reactions [35]. This leads to a shorter time scale for the production of multi-strange hadrons in a hadron gas.

In a quark gluon plasma there will be a lot of gluons and light (u and d) quarks. A light quark and an antiquark can react and produce a strange-antistrange quark pair,

$$q + \overline{q} \leftrightarrow s + \overline{s} \tag{1.9}$$

where q refers to a light quark, i.e. u or d quark. If the mass of a light quark, m_q, is neglected, the energy needed is only the mass excess of the two strange quarks, $2m_s \approx 2 - 300$ MeV. Due to Pauli blocking, production of $u\overline{u}$ and $d\overline{d}$ pairs requires more energy

than only the mass excess, $2m_q$, which favours production of strange quark pairs. In addition, strange quarks may be produced by gluon fusion and by gluon decay,

$$g + g \leftrightarrow s + \overline{s} \tag{1.10}$$

$$g \leftrightarrow s + \overline{s}. \tag{1.11}$$

Gluon decay requires a massive gluon. A finite mass for gluons suppresses gluon fusion, and leave gluon decay as a dominating process for production of strange-antistrange quarks [36]. With a massless gluon, the gluon fusion dominates the strange-antistrange quark pair production. Because of the large density of gluons in the plasma, the two gluon channels are the dominant processes. The relative importance of the two gluon processes varies with the gluon mass, but the total rate stays almost constant [36]. The production of strangeness in a quark gluon plasma therefore requires less energy and occurs with a larger probability (due to the large amount of gluons) than in a hadron gas. The largest enhancement is expected for multi-strange particles, which in a quark-gluon plasma are formed simply by combining several strange quarks in one particle at freeze-out.

Statistical models and particle ratios

Statistical models (see for instance [37] for an overview) assume that the system is in thermal and chemical equilibrium at chemical freeze-out, and that hadrons and resonances are not interacting anymore. The models do not have any description of the system before freeze-out. A statistical model can be used to calculate the number density of a particle species for a given chemical freeze-out temperature and baryochemical potential. The ratios predicted by the model are compared to experimentally measured ratios for a given data set. The temperature and the chemical potential are varied until the minimum difference between the measured and calculated ratios are found.

Due to the short lifetime of the system, there may not be enough time to fully saturate the strangeness content. The system can still be thought of as being in equilibrium if the produced strangeness is evenly distributed, but the strangeness phase space will not be saturated. This effect is often accounted for in the models by a strangeness saturation factor γ_s, where $\gamma_s \leq 1$. At RHIC energies γ_s is found to be very close to unity [11]. At the top SPS energy γ_s is found to be around 0.8-0.9, and close to unity at central rapidity [38].

Figure 1.10 shows the results of a fit using the statistical model described in [39] for SPS data at 158 A GeV/c. The model describes the experimental data well for a temperature of $T = 170$ MeV and a baryochemical potential of $\mu_B = 255$ MeV. Statistical models seems to work well also for other colliding systems and at other energies, for instance at RHIC energies [40, 37]. It is shown that statistical models work well for systems all the way down to collisions between elementary particles [41]. The fitted chemical freeze-out temperatures for different systems are shown in figure 1.11. The temperature flattens out at about 170 MeV when the collision energy increases, independent of the size of the colliding system. All the experimental ratios are found from an average over many events. It is possible that the fits do not represent true temperatures and chemical potentials if each event is not a statistically independent system.

A grand canonical approach is used in the statistical models. This is valid for large systems where the quantum numbers are conserved on average. In a small system where

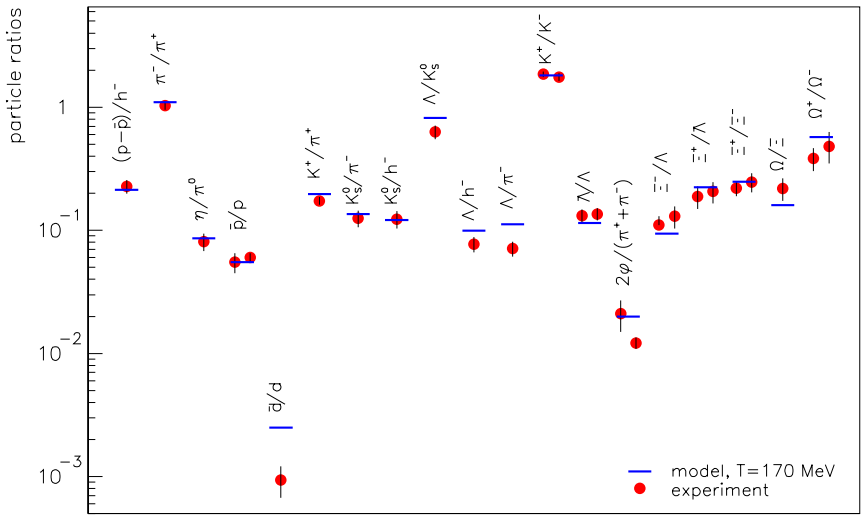

Figure 1.10: Particle ratios from statistical model compared to experimental ratios from SPS experiments at 158 A GeV/c [37].

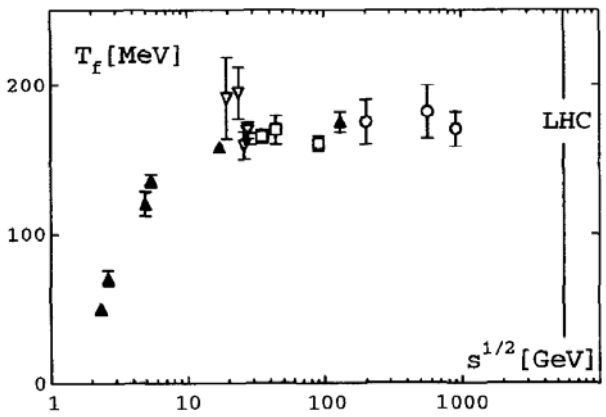

Figure 1.11: Chemical freeze-out temperature as a function of collision energy, for e^+e^- (squares), pp (open triangles), $p\overline{p}$ (circles) and AA (filled triangles) collisions [41].

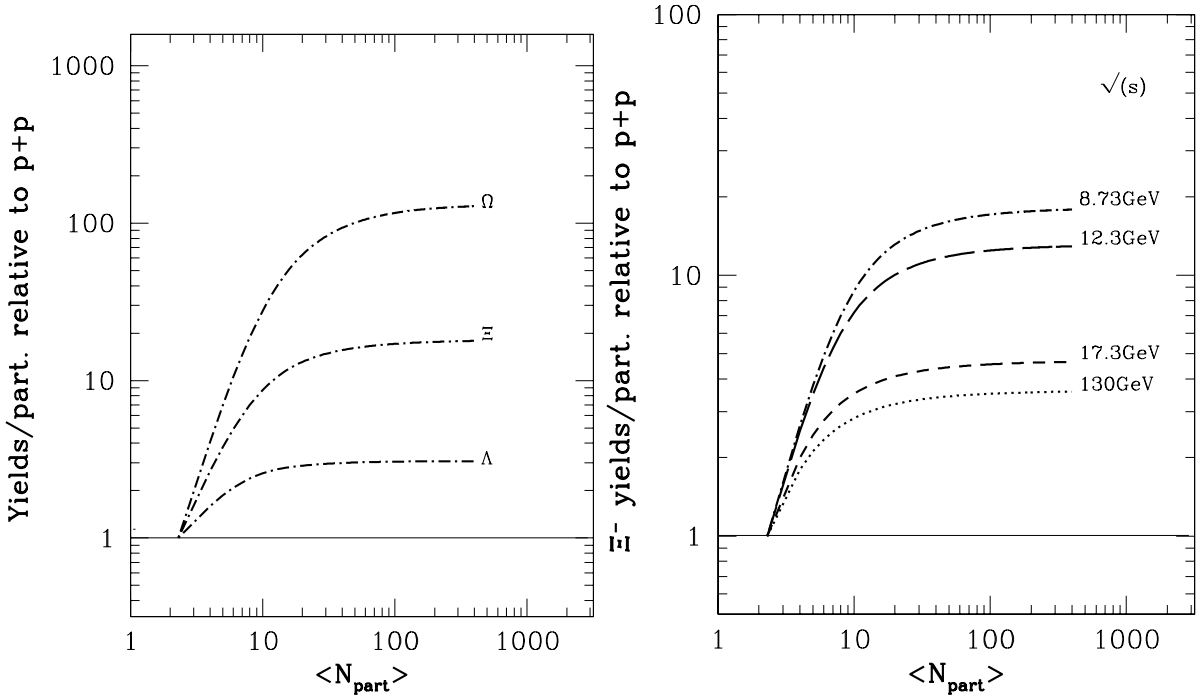

Figure 1.12: Left, the predicted centrality dependence of strangeness enhancement for Λ, Ξ and Ω at 40 A GeV/c. Right, the predicted centrality dependence of Ξ^- enhancement at different collision energies [42].

the canonical approach should be used, all quantum numbers have to be conserved explicitly. This means that in addition to sufficient energy, there has to be available phase space for strangeness production. Due to the lack of available phase space this results in a *suppression* of strangeness in small systems. When the volume becomes larger the suppression is expected to disappear and the strangeness production becomes constant. The volume is believed to be directly proportional to the number of participants in the collision. The strangeness *suppression* in small systems contributes to the strangeness *enhancement* in large systems. Figure 1.12 (left) shows the enhancement for Λ, Ξ and Ω in Pb-Pb collisions compared to p-p collisions using a beam momentum of 40 A GeV/c ($\sqrt{s}$ = 8.73 GeV), predicted by a statistical model including canonical suppression in small systems [42]. As shown, the enhancement is expected to be increasing with the strangeness content of the particle, and the largest enhancement is expected for the triply strange Ω. The enhancement is increasing with the size of the system (N_{part}), and is saturating for sufficiently large systems indicating that the grand canonical limit is reached. The predicted enhancements for the top SPS energy of 158 A GeV/c show the same pattern [43], but is expected to be lower [42]. In general it is predicted that the strangeness enhancement is decreasing with increasing energy (see figure 1.12, right).

Experimental results shown in chapter 5 and 6 of this thesis show that there *is* a strangeness enhancement and it is in fact increasing with increasing strangeness content of the particle. The enhancement increases with the size of the system. However, there is no evidence for a saturation, except maybe for $\overline{\Lambda}$s, and the measured enhancements

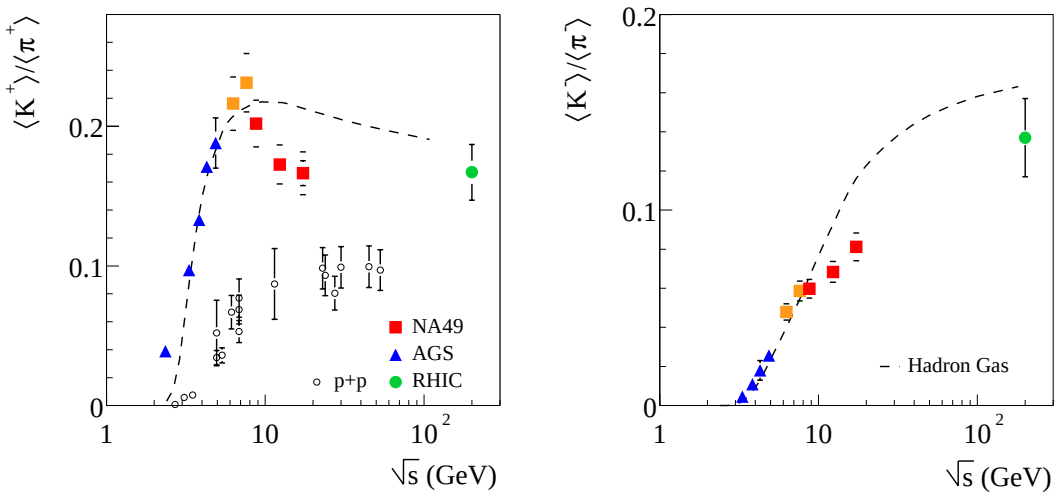

Figure 1.13: The K^+/π^+ (left) and K^-/π^- (right) ratios in central Pb-Pb and Au-Au collisions as a function of the collision energy [45]. Results from p-p collisions (open circles) are also included. The curves are predictions from a hadron gas model [46].

are not decreasing with increasing energies. One possible explanation is that the volume is not proportional to the number of participants. Another possibility is that the fitted temperature used to calculate the enhancement factors is not correct.

Strangeness enhancement and baryon density

Figure 1.13 shows the energy dependence of the K^+/π^+ and K^-/π^- ratios. The K^+/π^+ ratio shows a dramatic change around a beam momentum of 30 A GeV/c ($\sqrt{s_{NN}}$ = 7.62 GeV) [44]. It is tempting to believe that this discontinuity indicates a phase transition. If the system is in a hadronic phase, the chiral symmetry is broken and the strange quark mass has its constituent value. In this scenario the K/π ratio is expected to increase with increasing collision energy. If the chiral symmetry is restored and the quark masses decrease as a result of this, the K/π ratio is expected to be roughly independent of the collision energy. The K^+/π^+ ratio is compatible with this interpretation indicating a phase transition around $\sqrt{s_{NN}} = 7.62$ GeV. However, the K^-/π^- ratio shows a continuous rise with increasing collision energy.

The interpretation of the *horn* in figure 1.13 at lower SPS energy is debated. When increasing the collision energy, the baryon density of the fireball is decreasing. The quark contents of the K^+ and K^- mesons are $u\overline{s}$ and $\overline{u}s$ respectively. The K^-/K^+ ratio is therefore effectively $\overline{u}/u$ (since $s/\overline{s} = 1$), and is therefore depending on the baryon density. The experimentally measured K^-/K^+ ratio is shown in figure 1.14 as a function of the $\overline{p}/p$ ratio for different collision energies from AGS to RHIC. The $\overline{p}/p$ ratio is a measure on the baryon density or baryochemical potential (shown at the top of figure 1.14). The data show that the K^-/K^+ ratio is indeed varying with the baryon density. Included in the figure is also a prediction from a statistical model by Becattini *et al.* [47]. The model describes the data well. The BRAHMS experiment at RHIC has also measured the rapidity dependence of the K^+/π^+ and K^-/π^- ratios [48]. They find that the K^+/π^+

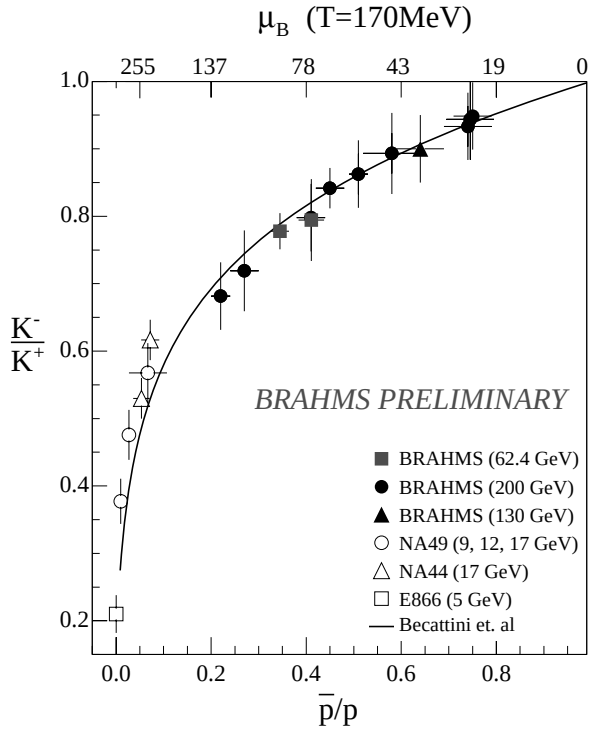

Figure 1.14: Correlation between strange meson and baryon-antibaryon ratios [49].

ratio increases and the K^-/π^- ratio decreases at high rapidities due to an increase of the baryon density (see figure 1.15). This behaviour is similar to what is observed by going from RHIC to SPS energies, and indicates that this is only an effect of the increased baryon density.

The Wroblewski factor, λ_s, is defined as [50]

$$\lambda_s \equiv \frac{2\langle s\bar{s}\rangle}{\langle u\bar{u}\rangle + \langle d\bar{d}\rangle} \tag{1.12}$$

where the quantities in brackets refer to the newly formed quark-antiquark pairs. This factor gives the ratio of produced strange quarks to produced non-strange quarks. Quarks that were present in the target and projectile are not included in the Wroblewski factor. Lines of constant λ_s in the $T - \mu_B$ plane, calculated from the thermal model in [46], are shown in figure 1.16 together with the freeze-out curve [51]. The calculated Wroblewski factor increases quickly up to AGS energies, and reaches a maximum around lower SPS energies ($T \approx 130$ MeV and $\mu_B \approx 500$ MeV). As the collision energy increases, the change in T is small whereas μ_B is decreasing resulting in a decreasing λ_s. From this prediction of the Wroblewski factor, the thermal model calculations [46] show a broad maximum in the K^+/π^+ ratio as shown by the curve in figure 1.13. The predicted maximum is at the same energy as observed by the NA49 experiment, but is not as sharp as the measured horn. The thermal model predictions for the K^-/π^- ratio shows the same trend as the data, but overpredicts the ratio at the higher energies.

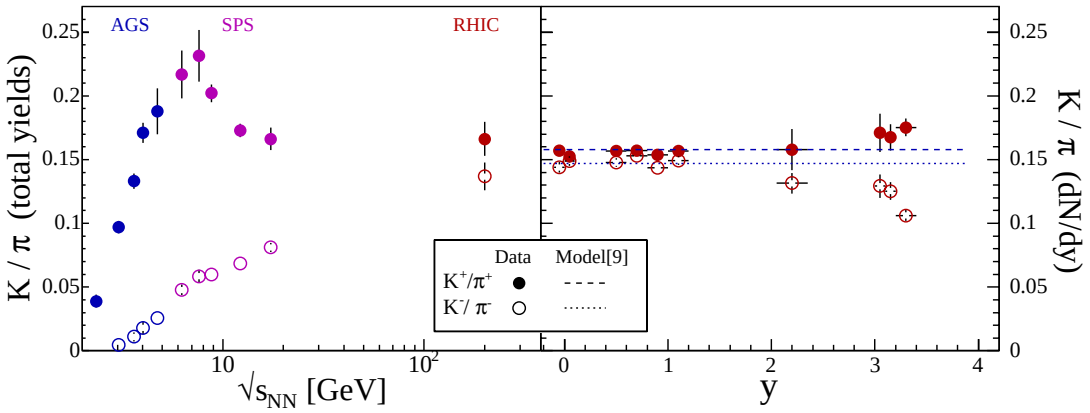

Figure 1.15: K/π ratios in full phase space as a function of $\sqrt{s_{NN}}$ (left) and rapidity (right) [48].

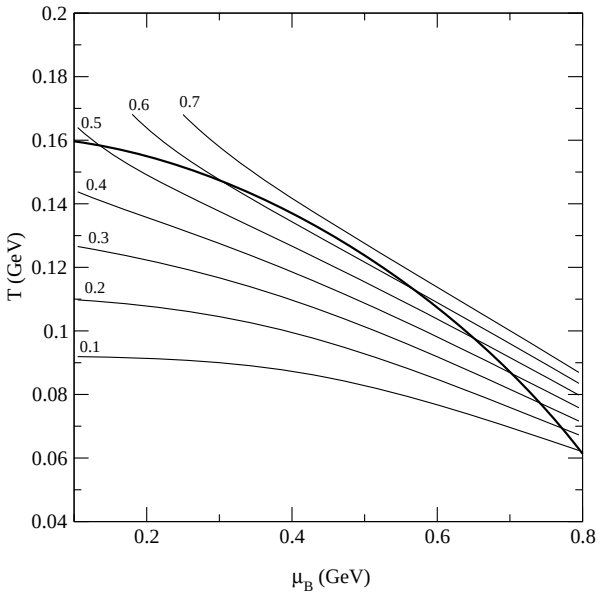

Figure 1.16: Lines of constant Wroblewski factor in the $T - \mu_B$ plane together with the freeze-out curve [46].

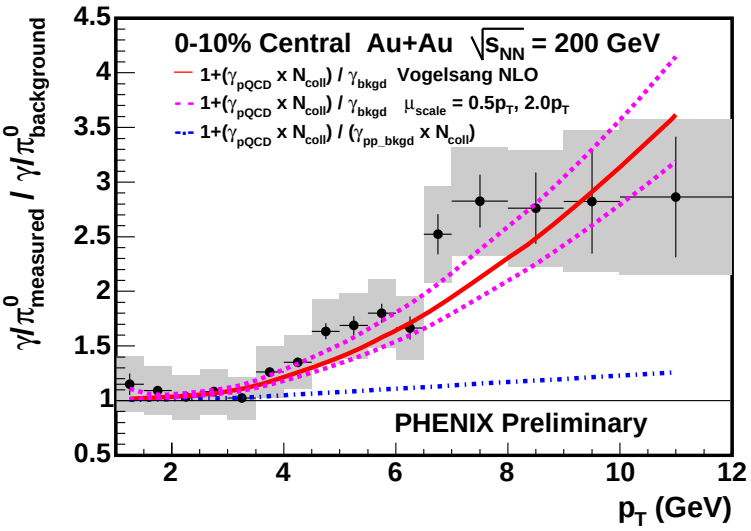

Figure 1.17: Excess of photons in central Au-Au collisions at RHIC [54].

1.4.5 Electromagnetic observables

Photons and leptons are affected by electromagnetic interactions only, and can therefore pass through the strongly interacting matter of the fireball virtually unchanged. The electromagnetic observables therefore provides information about the earliest stages of the collision.

Direct photons produced in the fireball mainly via the $q\overline{q} \rightarrow \gamma\gamma$ and $gq \rightarrow \gamma q$ channels carry information about the temperature at the initial stage of the collision. It has also been estimated that photon production at sufficiently high initial temperatures is higher in quark matter than in hadronic matter [52]. However, direct photons are very difficult to identify because of the large background from hadronic reactions, especially $\pi^0 \rightarrow \gamma\gamma$. Results from the WA98 experiment at CERN indicates an excess of photons in central Pb-Pb collisions at 158 A GeV/c [53]. Direct photons have also been measured by the PHENIX experiment at RHIC for central Au-Au collisions at $\sqrt{s_{NN}} = 200$ GeV [54]. Figure 1.17 shows the measured γ/π^0 ratio relative to the expected γ/π^0 ratio for the background measured by PHENIX. The results are compared to perturbative QCD calculations and found to be consistent with these. The dot-dashed curve in the figure indicates the expected enhancement if there was no suppression of mesons in the medium (see section 1.4.7).

Like photons, *dileptons* produced in the quark gluon plasma can provide information about the initial state. Again, the difficult task is to sort out the dileptons produced in the plasma from the large background of leptons produced in processes like photon conversions, pion annihilation, resonance decays, $\pi\rho$ and Drell-Yan interactions.

The NA38/NA50 experiments at CERN have measured an excess of dimuons in the intermediate mass region between the ϕ and the J/Ψ in central A-A collisions [55]. The excess is found to increase with the centrality of the collisions. The results are also confirmed by the NA60 experiment for In-In collisions at 158 A GeV/c [56]. NA60 have

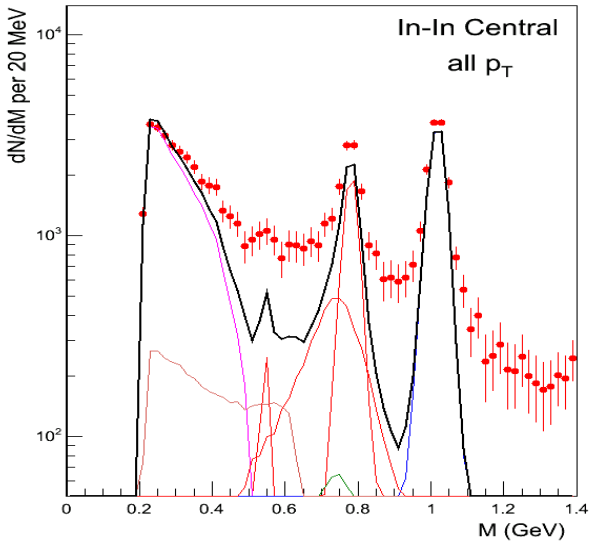

Figure 1.18: Excess of lepton pairs in the low mass region in central In-In collisions at the SPS [56].

concluded that the enhancement is consistent with prompt dimuons, while enhancement due to enhanced production of open charm particles is ruled out.

An excess of electron pairs in the low mass region 0.2-0.6 GeV/c^2 has been measured by the CERES/NA45 experiment at CERN in Pb-Au collisions at 40 and 158 A GeV/c [57]. An excess of lepton pairs is lately also seen in central In-In collisions at 158 A GeV/c by NA60 [56] (see figure 1.18). The excess is rising with centrality. The shape of the excess is found to be consistent with broadening of the ρ mass, whereas a mass shift of the ρ is ruled out ($m_\rho = 775.8 \pm 0.5$ MeV [3]).

1.4.6 J/Ψ suppression

The J/Ψ meson is a bound state of a charm and an anti-charm quark ($c\overline{c}$). It has been predicted that colour screening would prevent $c\overline{c}$ binding in a quark gluon plasma, and that J/Ψ suppression in nuclear collisions should provide an unambiguous signature of a quark gluon plasma formation [58]. The J/Ψ meson has a large bound state radius and in a plasma the c and $\overline{c}$ quarks effectively do not "see" each other. Instead of binding to each other, they therefore find a different quark and open charm particles, such as D mesons ($c\overline{q}$ or $\overline{c}q$), are produced. The Ψ' has an even larger bound state radius than the J/Ψ and should therefore also be suppressed in a quark gluon plasma [58].

The NA38 [59] and NA50 [60] experiments identify the J/Ψ meson through its decay into muon pairs ($\mu^+\mu^-$). This accounts for 5.9% of the J/Ψ decays. J/Ψ has been found to be suppressed in O-U, S-U and Pb-Pb collisions, and the suppression is found to increase with centrality [61, 62]. However, there are now several theoretical models, also without QGP formation, that are able to explain the NA38/NA50 results (e.g. [63, 64]). The NA60 collaboration measures an anomalous J/Ψ suppression also in In-In collisions at 158 A GeV/c [56]. The suppression is found to be depending on the centrality of the

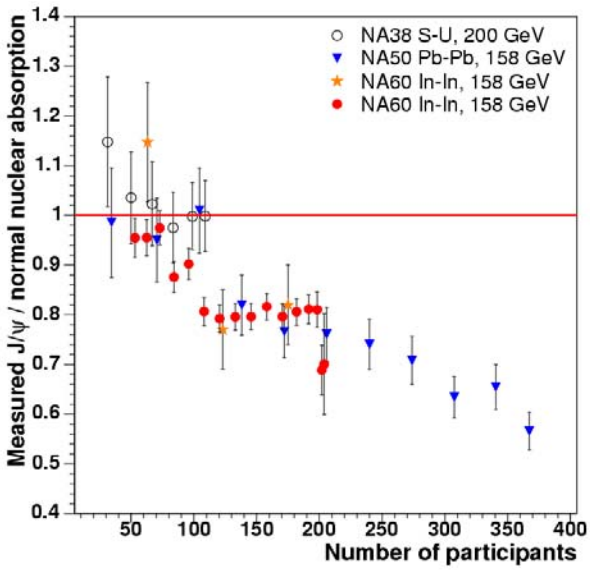

Figure 1.19: J/Ψ production relative to the nuclear absorption, versus number of participants [56] measured by the NA38, NA50 and NA60 experiments.

collisions, with an onset around $N_{part} = 90$. J/Ψ suppression is observed already in p-A collisions due to absorption of the J/Ψ as it passes through the nuclear matter. This absorption is also affecting the number of J/Ψs observed in A-A collisions. The J/Ψ production, compared to the expected production in case of pure nuclear absorption, measured by NA38, NA50 and NA60 is presented as a function of number of participants in figure 1.19.

A statistical recombination model (see e.g. [37] and references therein) suggests that the suppression of J/Ψ is overcome by statistical recombination of J/Ψ mesons from the same or different $c\overline{c}$ pairs at freeze-out. The effect of the recombination is an *enhanced* production of J/Ψ in a quark gluon plasma compared to a hadronic scenario.

The PHENIX experiment has measured the J/Ψ production at RHIC [65]. In central Au-Au collisions at $\sqrt{s_{NN}} = 200$ GeV the suppression is found to be similar to the suppression found by NA50 at the SPS [66]. The results is in agreement with models including both colour screening and recombination.

1.4.7 High p_{T} suppression

Partons resulting from hard scatterings during the initial collision between two nuclei are probes that are directly sensitive to the properties of the matter created in the collision. A colour charged parton passing through colour charged matter may interact and lose energy through gluon bremsstrahlung. As a result, the yield of high p_{T} hadrons produced from the fragmentation of these partons are expected to be suppressed at RHIC and LHC energies [67]. In contradiction, if the parton passes through hadronic matter which is colour neutral, it does not interact strongly with the matter and loses much less energy.

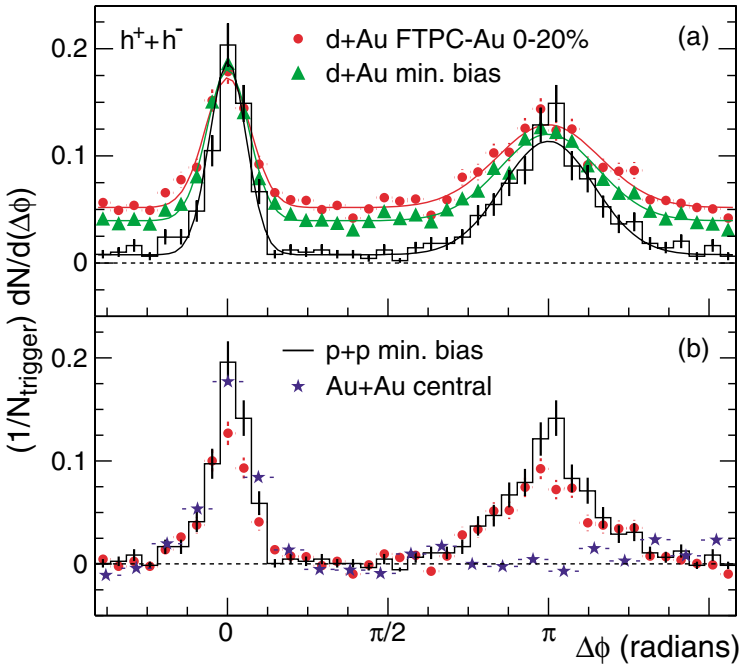

Figure 1.20: Two-particle azimuthal distributions for a) minimum bias and central d-Au collisions and p-p collisions, and b) central Au-Au collisions compared to central d-Au collisions and p-p collisions measured by the STAR experiment at RHIC [68].

One way of studying the suppression of high p_{T} hadrons is to measure the two-particle azimuthal distribution. The high p_{T} parton fragments into a jet of hadrons, i.e. a group of high p_{T} particles emitted in a narrow cone. The high p_{T} parton scattering processes and the production of jets can be described by perturbative QCD. The jets are produced in pairs that are emitted back-to-back. If a jet is produced close to the surface of the fireball in a nucleus-nucleus collision, it may escape from the collision zone and be detected as high p_{T} particles. The other jet has to pass through the coloured matter of the fireball and is therefore expected to lose energy. The two-particle azimuthal distribution for p-p, d-Au and Au-Au collisions measured by STAR [68] is shown in figure 1.20. A *leading particle* from a jet is measured at the *near-side*, $\Delta\phi = 0$. The azimuthal angle of other high p_{T} hadrons are measured relative to this particle. As can be seen from the figure *away-side* jets, $\Delta\phi = \pi$, are observed both in p-p and in d-Au collisions at RHIC. In central Au-Au collisions, the away-side jets are quenched and the peak at $\Delta\phi = \pi$ disappears.

Another method for observing the high p_{T} suppression is to measure the *nuclear modification factor*

$$R_{AB}(p_{\mathrm{T}}) = \frac{\mathrm{d}^2 N_{AB}^{C}/\mathrm{d}p_{\mathrm{T}}\mathrm{d}y}{\langle N_{coll}\rangle/\sigma_{inel}^{pp}\mathrm{d}^2\sigma^{pp}/\mathrm{d}p_{\mathrm{T}}\mathrm{d}y} \tag{1.13}$$

where $\langle N_{coll}\rangle$ is the mean number of binary collisions in the A-B collision, σ_{inel}^{pp} is the inelastic cross section for p-p collisions, $\mathrm{d}^2 N_{AB}^{C}/\mathrm{d}p_{\mathrm{T}}\mathrm{d}y$ is the measured differential particle yield per event in A-B collisions, and $\mathrm{d}^2\sigma^{pp}/\mathrm{d}p_{\mathrm{T}}\mathrm{d}y$ is the measured differential cross section from p-p collisions. If A-B collisions are a superposition of N_{coll} independent

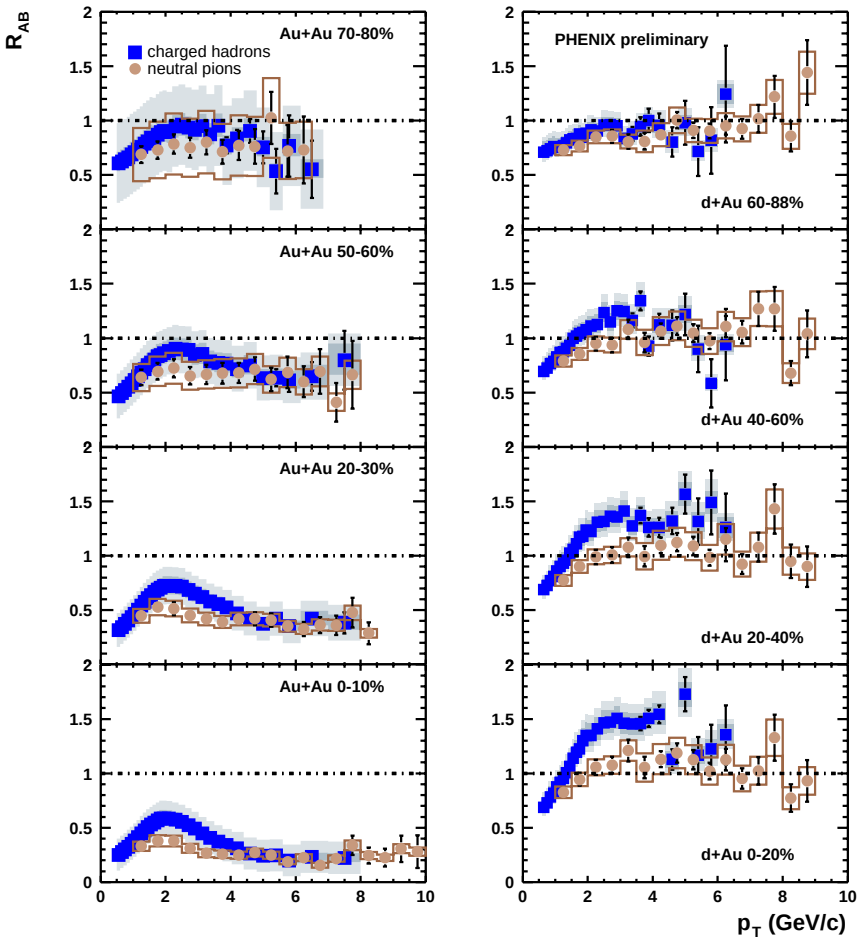

Figure 1.21: Centrality dependence of the nuclear modification factor in Au-Au (left) and d-Au (right) collisions measured by PHENIX [69].

nucleon-nucleon collisions, the nuclear modification factor should be equal to unity. If it scales with the number of participants it should be less than unity since $N_{part} \leq N_{coll}$.

Nuclear modification factors, R_{AB}, for Au-Au and d-Au collisions at $\sqrt{s_{NN}} = 200$ GeV measured by PHENIX [69] are shown in figure 1.21. R_{AB} are measured for both charged hadrons and π^0 and is given as a function of p_{T}. The results are presented for different centrality classes. A suppression of high p_{T} particles in central Au-Au collisions is observed, probably due to partons losing energy in the dense medium. In peripheral Au-Au collisions R_{AB} is consistent with unity. In d-Au collisions no quark gluon plasma is expected to be formed. This collision system is studied to make it possible to distinguish between initial and final state effects. The measured nuclear modification factors for central d-Au collisions shows a clear difference from central Au-Au collisions. No high p_{T} suppression is observed in d-Au collisions, indicating that the high p_{T} suppression in central Au-Au collisions comes from final state effects. This supports the picture of medium-induced energy loss. The enhancement at intermediate p_{T} is due to multiple soft scattering of incoming nucleons or partons, referred to as the *Cronin effect*.

All four RHIC experiments observe a suppression of high p_{T} particles in Au-Au col-

lisions compared to p-p collisions [70], indicating that some kind of coloured matter is created. It is not clear whether the matter is deconfined or consists of confined coloured matter. Elliptic flow measurements at RHIC indicate that the observed matter is behaving like a perfect liquid. Shuryak and Sahed [71] have suggested that the new matter is a strongly coupled quark gluon plasma (sQGP), consisting of confined coloured matter.

Chapter 2

The WA97 and NA57 experiments

The WA97 [72] and NA57 [73] experiments operated at the Super Proton Synchrotron (SPS) facility at CERN. They were both fixed target experiments designed to study the central fireball region created in ultrarelativistic heavy ion collisions. The WA97 experiment had its first period of data taking in 1994, and was located in the OMEGA facility in the West Area at CERN. Due to the decommissioning of the OMEGA spectrometer in 1996, a new but similar experiment, NA57, was set up in the North Area at CERN in 1997. The NA57 experiment collected data from 1998 to 2001.

NA57 is the last in a series of experiments. The series began in 1987, when the WA85 experiment [74] started collecting data. This experiment was replaced by the WA94 experiment [75] in 1991, and later by WA97 and NA57. The common denominator for all four experiments is the study of strangeness enhancement in ultrarelativistic heavy ion collisions (see section 1.4.4). The differences between the four experiments are in the collision systems and beam energies, and most of the detectors have been replaced during the years. WA85 studied sulphur-tungsten collisions, while WA94 studied sulphur-sulphur collisions. The WA97 and NA57 experiments are described in detail in this chapter.

The WA97 experiment was designed to look for strange particle enhancement as a signature of a quark gluon plasma phase. A quark gluon plasma is expected to be formed only if the energy density is large. In the laboratory the largest energy density is obtained in central heavy ion collisions with a large beam energy. Lead ions are the heaviest accelerated particles at the SPS, and WA97 therefore studied central lead-lead interactions at a beam momentum of 158 A GeV/c, which is the maximum for lead ions in the SPS. As reference data for the lead-lead measurements, both proton-lead and proton-beryllium collisions were studied. The proton beam momentum was 158 A GeV/c. The main result from WA97 is that the production of strange baryons and anti-baryons in Pb-Pb collisions at 158 A GeV/c, is enhanced with respect to p-Be collisions at the same beam momentum [76]. The enhancement increases with the strangeness content of the baryon. The observed behaviour has been predicted as a consequence of the quark gluon plasma phase transition [33]. The results are further described in chapter 5.

The NA57 experiment was designed to look for the *onset* of the strange particle enhancement. This is done in two ways. The first approach is to study the enhancements for different collision energies per incoming nucleon. NA57 has therefore collected data at both 40 and 158 A GeV/c, while WA97 collected data at 158 A GeV/c only. The other approach is to study the enhancements for more peripheral collisions.

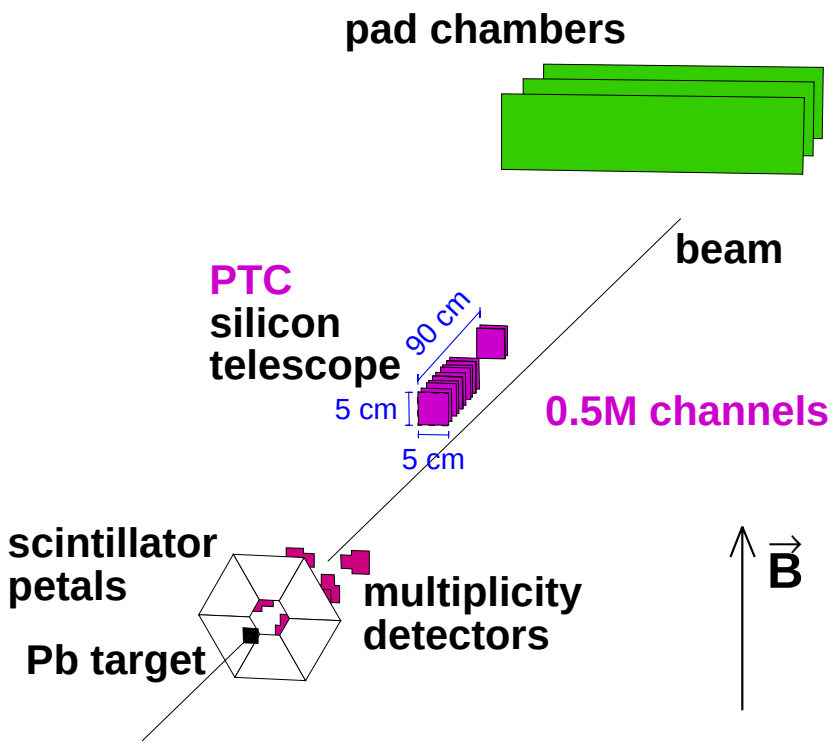

Figure 2.1: The WA97 experimental setup.

When studying strangeness enhancement, multistrange particles like the Ξ or the Ω are of special interest. The Ω is very rare, so a large number of events has to be collected in order to gain a reasonable sample. Therefore WA97 and NA57 chose to build a small detector that covered only a narrow phase space, about one unit of rapidity around the central rapidity and relatively high p_{T}. Hyperons (especially the Ωs) are mostly created in the central collision zone. To study the overall properties of heavy ion collisions, a large acceptance detector is needed, but with a small, central detector, a comparatively large sample can be obtained in a reasonable time even for proton-induced reactions.

2.1 The WA97 experiment

A sketch of the setup of the WA97 experiment is shown in figure 2.1. The target, the scintillator petals, the multiplicity detectors and the silicon telescope are all placed in a magnetic field. This means that the tracks from charged particles are bent, and their momenta can be calculated. The main detector in the experiment is the silicon telescope, used for track finding. The pad chambers, which are placed outside the magnet, are used together with the last part of the silicon telescope, as a lever arm to improve the momentum resolution of the high-momentum tracks. The multiplicity detectors are used for offline analysis of the charged particle multiplicity of an event. The fast scintillator petals are used for triggering purposes together with a number of beam counters that are not shown in the figure.

2.1.1 The Omega spectrometer

The Omega spectrometer was a general purpose facility located in the West experimental area of the CERN SPS. The spectrometer was decommissioned in 1996 for economic reasons. The superconducting Omega magnet consisted of two Helmholtz coils producing a close to uniform magnetic field of 1.8 T. Inside the magnet there was an area of about 36 m^2 where the target and most of the detectors used for track identification were placed. A more detailed picture of the WA97 setup is shown in figure 2.2.

The center of the magnet defines the origin of the coordinate system of the experiment. The x axis points downstream along the beam direction. The positive z direction is upwards (towards the ceiling), and the direction of the y axis is defined by requiring a right-handed coordinate system. The main component of the magnetic field is in the z direction.

During the experiment both field directions, up and down, of the magnet were used. This was done to reduce systematic errors and to help the detailed alignment of the detectors.

2.1.2 The target

A lead target was used with the lead beam, and beryllium and lead targets were used with the proton beam. When using a lead beam the lead target was 0.4 mm thick, which corresponds to 1 % of an interaction length. In 1994 the experiment started out with the target placed 120 cm upstreams from the first plane of the telescope (x = -120 cm). During the run, the target was moved to x = -90 cm to increase the acceptance. It turned out that the number of tracks in the telescope were quite manageable, so from 1995 the target was moved to x = -60 cm, i.e. 60 cm in front of the first pixel plane in the telescope.

When using a proton beam, the target was always placed 90 cm upstreams from the first pixel plane. The lead and the beryllium targets in this case had a thickness corresponding to 8 % of their respective interaction lengths. For beryllium this corresponds to a thickness of approximately 3.2 cm.

2.1.3 Multiplicity detectors

There were two sets of multiplicity counters in WA97. A set of six scintillators, the petals, were placed 10 cm downstream from the target (see figures 2.1 and 2.2). These detectors were used in the trigger to select the most central events. The trigger corresponded to selecting approximately the most central 40% of the Pb-Pb collisions. The petals were covering a pseudorapidity range of $1 < \eta < 2$.

Two stations of multiplicity microstrip detectors (MSD) were placed just behind the petals (20 and 55 cm behind the target). Each station consisted of 3 arms, one down and two to the sides (see figure 2.3). The upper arm was left out to avoid too much material in front of the silicon telescope. The strip dimensions were chosen to keep the occupancy approximately uniform in all strips. The two planes covered the pseudorapidity region $2 < \eta < 3$ and $3 < \eta < 4$ respectively. Information from the MSD was used to calculate a more accurate multiplicity of charged particles in the offline analysis.

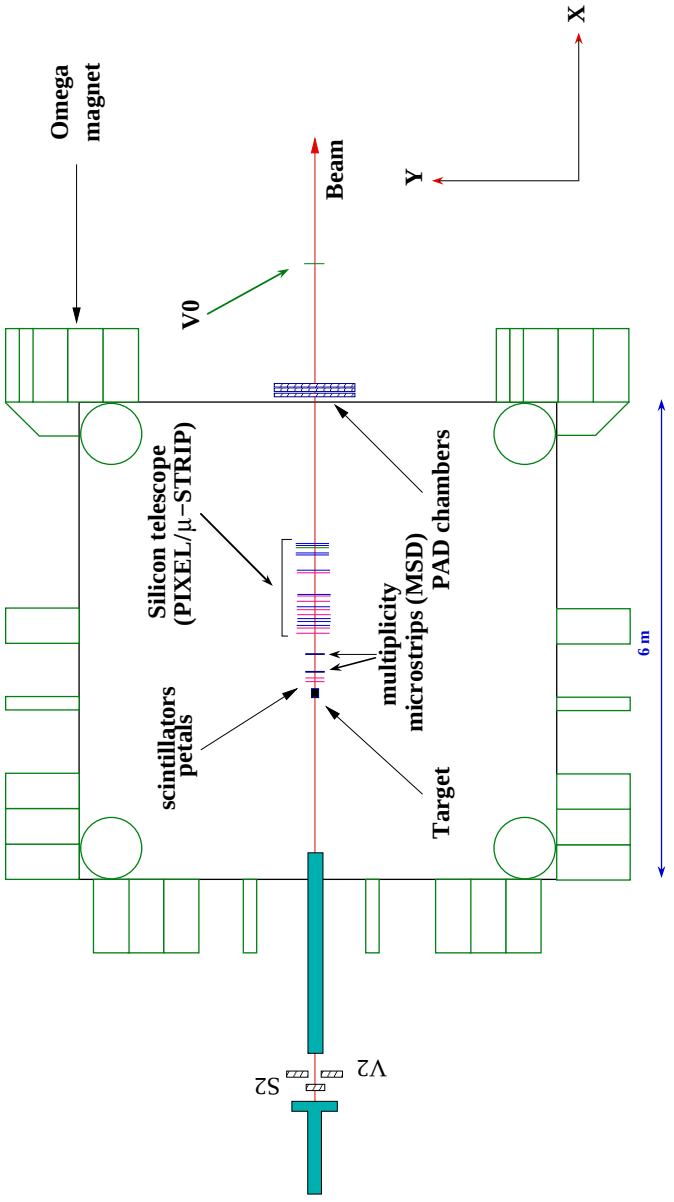

Figure 2.2: The WA97 experimental setup (detailed).

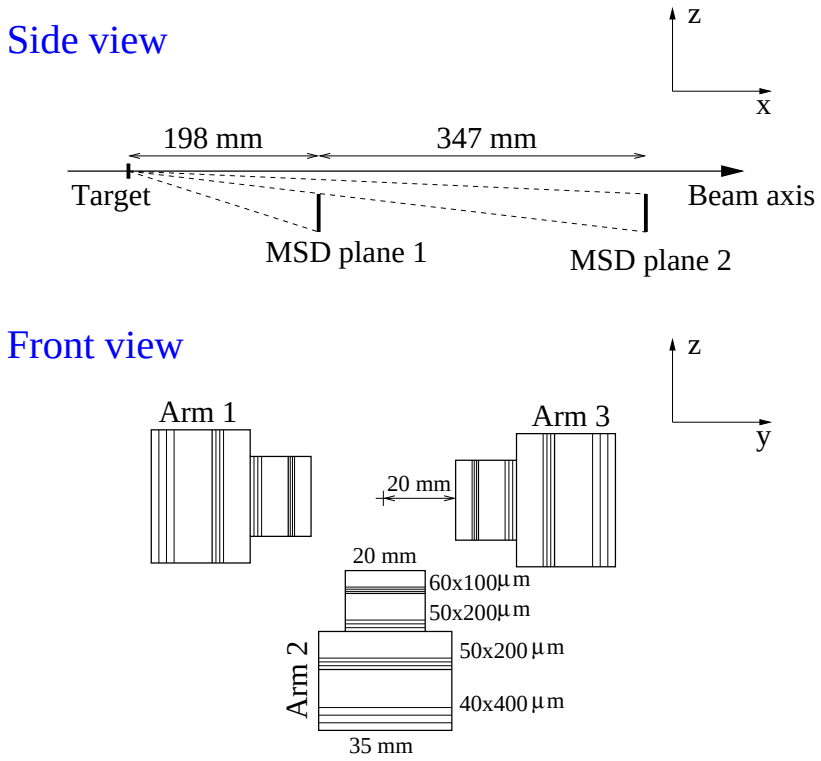

Figure 2.3: The WA97 multiplicity microstrip detectors.

2.1.4 The silicon telescope

The telescope was composed of silicon pixel planes and silicon microstrip planes. The first part (30 cm) of the silicon telescope in WA97 consisted of densely packed planes of silicon detectors, and provided information used to reconstruct tracks from charged particles passing through. This is called the compact part of the telescope. The last part was used together with the pad planes as a lever arm to get an improved momentum resolution for high momentum tracks. There was a gap of 30 cm between the compact part of the telescope and the first plane in the lever arm.

The WA97 silicon telescope was placed above the beam line and inclined to point back to the target. The inclination angle was chosen in such a way that there was a good acceptance for the decay particles from hyperons produced at central rapidity and $p_{\mathrm{T}} > 0.5$ GeV/c. Each plane had a sensitive area of 5×5 cm^2, and the total length of the telescope was 90 cm.

Silicon microstrip detectors

The silicon microstrip detectors had a pitch of 50 μm, and each detector plane had 1024 channels and a size of 5×5 cm^2. There were y- and z-planes. The y-planes had vertical strips and gave xy coordinates. The z-planes had horizontal strips and gave xz coordinates. A three-dimensional track from a charged particle is reconstructed by combining hits from y- and z- planes.

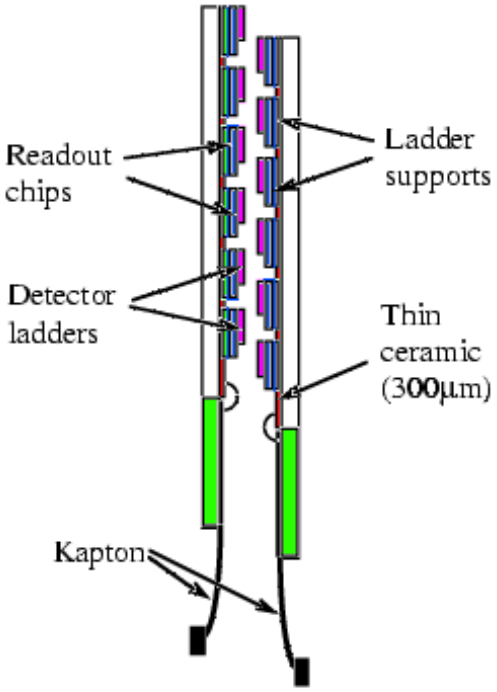

Figure 2.4: The WA97 silicon pixel detectors.

Silicon pixel detectors

During the first WA97 run in 1994, four OMEGA-2 pixel planes [77] were placed in the silicon telescope [78]. The pixel detectors provided two-dimensional readout, and each hit gave a space point, where the x coordinate was given by the x position of the plane.

Each pixel plane consisted of two arrays mounted face-to-face, and one array shifted about 4 mm with respect to the other. Each array consisted of six ladders (see figure 2.4), with six readout chips per ladder. There was a small overlap between the ladders in the two arrays in order to make sure that the whole 5×5 cm^2 area of a plane was covered. A ladder was built from 96 columns and 64 rows of rectangular diodes, ion-implanted on a high-resistivity n-type silicon substrate. Each diode was a pixel in the detector. Each pixel had a size of 500 μm $\times$ 75 μm, and in one single plane there was altogether more than 73,000 pixels.

The support for the planes was u-shaped, with no material on the lower edge nearest to the beam. The thickness of material in the sensitive region of one plane corresponded to about 1.7% of a radiation length.

Due to the rectangular shape of the diodes, they gave a better resolution in one space coordinate than the other. Therefore, there was a mixture of orientations of the planes, some simply rotated 90° compared to the others. The planes are referred to as y and z pixel planes. In the offline analysis, the information from the pixels were originally (for historical reasons) used after the initial track finding was done using information from the microstrip planes. The pixels only helped in finding the most correct combination of hits in the microstrip planes. This method was changed already in the analysis of the 1995 data sample. At this time more microstrip planes had been exchanged by new pixel planes,

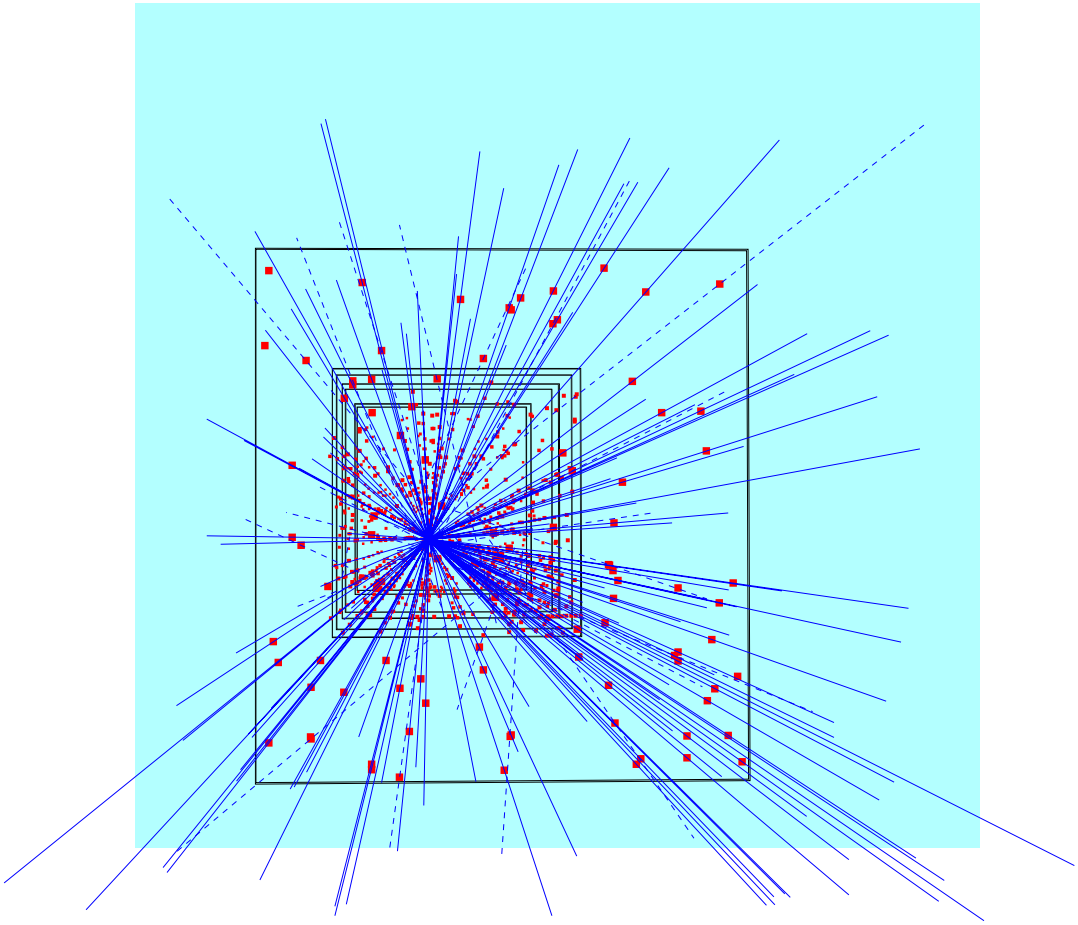

Figure 2.5: 153 reconstructed tracks in the WA97 pixel telescope in a no-field event.

and the track finding was performed using the pixels. After this, the information from the microstrip planes were used only to improve the resolution in the coordinate where the pixels had the poorest (500 μm) resolution. Figure 2.5 shows tracks reconstructed using information from the pixel planes in WA97.

2.1.5 Lever arm

The last stations in the silicon telescope and the three pad chambers that were placed outside the OMEGA magnet, were not used in the track finding. Tracks from the compact part of the telescope were extrapolated to these detectors. Hits that matched the tracks were included in the track information to get an improved momentum resolution for high momentum tracks.

The pad chambers were three multi-wire proportional chambers with pad cathode read-out. Each chamber had a sensitive area of 810×192 mm^2, and the cathode was divided into pads of size 4×12 mm^2.

2.1.6 Trigger

S2, V2 and V0 shown in the setup in figure 2.2 are beam counters used for triggering information. S2 was placed in the beam upstream of the target and gives information about the beam. V2 was a square veto counter with a hole in the center to allow the beam to pass through. To trigger on a clean beam, a hit in S2 was required together with no hit in V2, and also no further hit in S2 during the next 30 ns to avoid beam particles hitting the target too close in time. The V0 counter was placed downstream of the target, after the pad chambers, in the prolongation of the beam line. If there was an interaction in the target, no particles are expected to follow the beam line and hit the V0 counter. Absence of a hit in V0 was therefore required to trigger on an event. Finally, the petals described in section 2.1.3 were used to trigger on the centrality of the event.

2.1.7 The beam telescope

During the p-Be run in 1996 a set of five microstrip planes formed a beam telescope. The planes were placed before the target and stored the parameters of the beam track for each triggered interaction. The information was used in combination with telescope tracks to reconstruct the exact vertex position inside the 3.2 cm thick beryllium target (see section 3.2.2).

2.2 The NA57 experiment

After the decommissioning of the OMEGA spectrometer, most of the experimental programme of WA97 was continued in the North Area at CERN in the NA57 experiment. The new experiment was also optimized to measure strange particles. The geometrical acceptance of NA57 is similar to WA97, covering about one unit of central rapidity, and transverse momenta down to a few hundred MeV/c [79]. The multiplicity detectors used by WA97 were reused by NA57 and the tracking was still done by the silicon telescope. Some important changes were done that are summarized here:

- A new beam line with a smaller spot size than in WA97
- A different magnet
- A new telescope layout with silicon pixel planes only
- A new data acquisition system, and thereby a new data format

The new beam line had its last beam detector (S2) far away from the target. The beam line had better shielding and vacuum all the way to the target, resulting in less empty target contamination. As a consequence of the new data acquisition and the new telescope layout, significant changes had to be made in the alignment, track finding and event reconstruction software.

NA57 collected Pb-Pb data at both 40 and 158 A GeV/c beam momentum, together with a sample of p-Be reference data at 40 GeV/c. For proton reference data at 158 GeV/c, the WA97 p-Be and p-Pb data samples are used. The NA57 experimental layout is shown in figure 2.6.

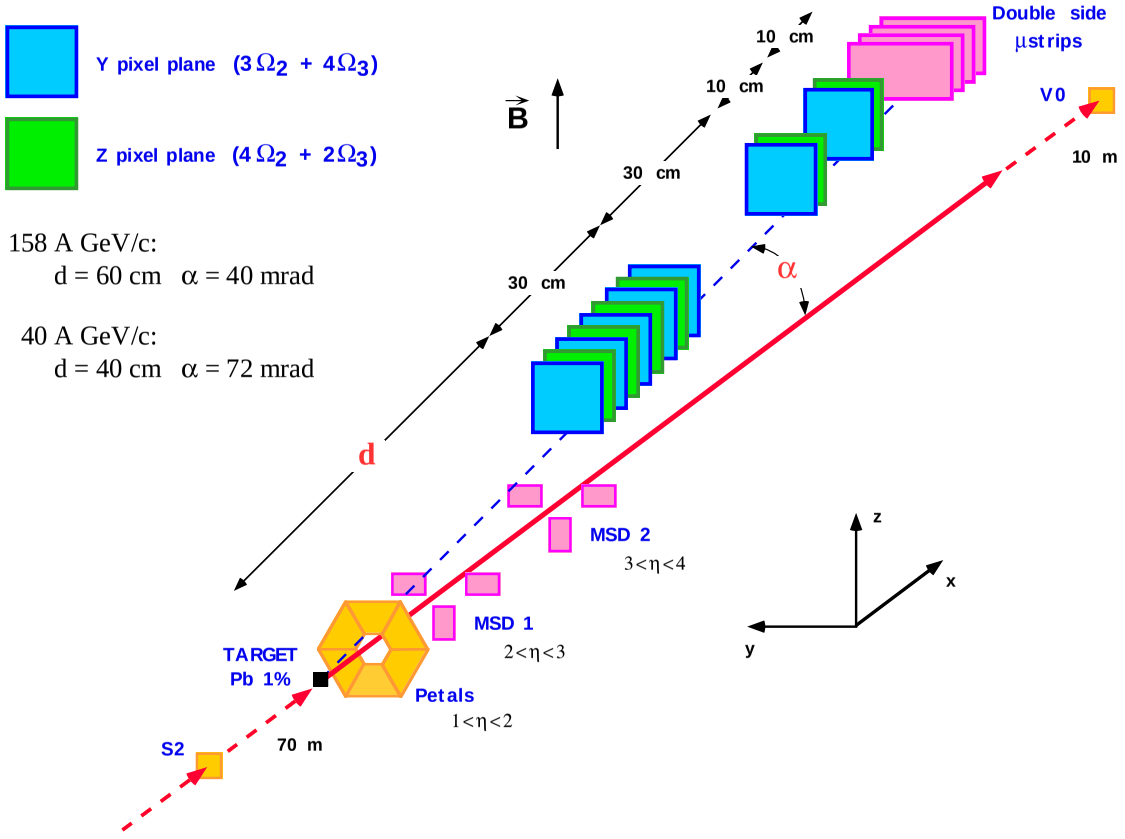

Figure 2.6: The NA57 experimental layout.

Figure 2.7: The GOLIATH magnet with the silicon telescope mounted on rails.

2.2.1 The Goliath magnet

NA57 uses the GOLIATH magnet, which provides a slightly weaker and less uniform field than the OMEGA magnet used by WA97. The gap is 1.05 m and the maximum field is 1.4 T. The GOLIATH magnet is also physically smaller than the OMEGA magnet. The OMEGA magnet was big enough to walk inside, and detectors were mounted directly inside the magnet. In the GOLIATH magnet, the detectors are mounted on an optical bench that can be moved in and out from the magnet on rails (see figure 2.7).

2.2.2 The Beam

In NA57 there is a new beam line with a smaller spot size compared to WA97, both in vertical and horizontal direction. The amount of material in the beam line has been kept to a minimum in order to minimize interactions outside the target. This allows for an extended centrality range.

2.2.3 The target

No changes were done to the lead and beryllium targets compared to WA97 (see section 2.1.2). At 158 A GeV/c the target was positioned 60 cm in front of the first pixel plane of the telescope. At 40 A GeV/c the distance was reduced to 30 cm.

2.2.4 The multiplicity detectors

The Pb-Pb data sample was collected using a centrality trigger, based on the scintillator petals described for WA97 (section 2.1.3) placed 10 cm downstream of the target. The trigger in NA57 selects the most central 60% of the collisions. More precise centrality information, used for off-line analysis, is provided by two planes of silicon microstrip detectors (MSD), also used by WA97 (section 2.1.3).

2.2.5 The silicon telescope

The main tracking device is the silicon telescope. In NA57 the silicon microstrip planes used by WA97 (section 2.1.4) are all replaced by silicon pixel detectors. The sensitive area of a plane is also here 5×5 cm^2. About half of the pixel planes used by NA57 were OMEGA-2 planes, already described in section 2.1.4. The other half of the planes were new OMEGA-3 planes [80]. The most visible difference being the pixel size that has changed from 500 μm $\times$ 75 μm to 500 μm $\times$ 50 μm. An OMEGA-3 ladder has 96×127 pixels, and four ladders in each array, altogether about 97,000 pixels per plane.

2.2.6 Lever arm

The last part of the silicon telescope is used as a lever arm to improve momentum resolution for the high momentum tracks. In addition, four double-sided microstrip planes were installed from 1998. The active area for each microstrip plane is 73×40 mm^2, and there are 768 read-out strips implanted on each side with a 95 μm pitch. The strips are tilted with respect to the short side of the detector by a small angle of 17.5 mrad. The internal angle between the strips on the two sides is therefore 35 mrad. The RMS resolution of the detectors is about 27 μm in the bending plane (y) and about 1 mm in the non-bending plane (z).

2.2.7 Trigger

Triggering in NA57 was essentially done the same way as in WA97 (section 2.1.6), except there was no V2 counter. Placed upstream from the target, S2 was used to trigger on a beam particle, and also to avoid triggering on an event where two beam particles were too close in time. An absence of a signal in V0 was required in order to trigger on events with interaction in the target. Finally, the Petals were used for centrality selection (see section 2.2.4).

2.2.8 Data acquisition

The data acquisition system used by NA57 is called DATE (Data Acquisition and Test Environment) [81] and is provided by the ALICE DAQ group. DATE is further developed and will be used as the data acquisition system for the ALICE experiment. The NA57 experiment provided a real-life testbed for the development of the system.

2.3 Running periods for WA97 and NA57

The WA97 and NA57 collaborations have collected data from 1994 to 2001. Information of the running periods is listed in table 2.1.

Experiment	Year	Beam momentum	Collision system
WA97	1994	158 A GeV/c	Pb-Pb
	1995	158 A GeV/c	p-Pb and Pb-Pb
	1996	158 A GeV/c	p-Be and Pb-Pb
NA57	1998	158 A GeV/c	Pb-Pb
	1999	40 A GeV/c	p-Be and Pb-Pb
	2000	158 A GeV/c	Pb-Pb
	2001	40 A GeV/c	p-Be

Table 2.1: Running periods for the WA97 and NA57 experiments.

Chapter 3

Event reconstruction

In this chapter the general procedure for track reconstruction is described. The procedure is in principle the same for the WA97 and the NA57 experiments, but some differences are pointed out. The cuts made during the analysis are slightly different for the different data sets. In this thesis the cuts for Pb-Pb data collected in 1998 are discussed in some detail. The results shown in chapter 5 also include other data sets, with similar cuts.

The aim for the analysis in the two experiments is to find the number of strange particles produced in the collisions. The measured strange particles are K^0_S, Λ, Ξ, Ω and their corresponding antiparticles. All particles are identified by analysing their decay into charged particles (branching ratios in parenthesis):

$$\begin{aligned}
K^0_S &\longrightarrow \pi^+ + \pi^- \qquad (\text{BR} = 68.9\ \%) \\
\Lambda &\longrightarrow p + \pi^- \qquad (\text{BR} = 63.9\ \%) \\
\Xi^- &\longrightarrow \Lambda + \pi^- \qquad (\text{BR} = 99.9\ \%) \\
&\qquad\ \hookrightarrow p + \pi^- \\
\Omega^- &\longrightarrow \Lambda + K^- \qquad (\text{BR} = 67.8\ \%) \\
&\qquad\ \hookrightarrow p + \pi^-
\end{aligned}$$

The antiparticles are identified by looking at the corresponding decay channels. The decays are illustrated in figure 3.1. By this method, neutral particles like K^0 and Λ, may be identified via their decays to charged particles. The strange particles are required to decay before the tracking detectors, so the vertices are reconstructed by extrapolating the charged tracks.

The decay tracks have to be reconstructed among ~ 1000 charged particles produced in a central lead-lead interaction. Due to the small size of the tracking detectors, and since the detectors are lifted above the beam line, only about 20 charged particles pass through the silicon telescope per event in Pb-Pb collisions at 158 A GeV/c.

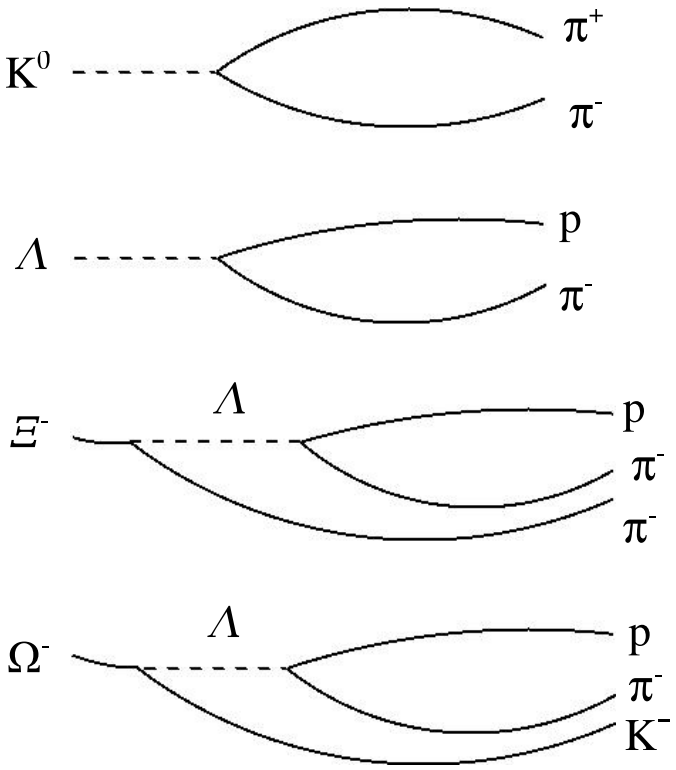

Figure 3.1: Decay topologies for strange particles studied by the WA97 and NA57 experiments.

The offline analysis is divided into steps. The event multiplicity is calculated from information stored in the multiplicity microstrip detectors (see section 2.1.3). Hits from charged particles traversing the silicon telescope are combined to give tracks. V^0 candidates are found by combining two oppositely charged tracks, and some of them are identified as K^0s or Λs. Some of the Λs, when combined with another charged track, give cascade candidates (Ξ or Ω). Some of the cascade candidates pass all selection criteria and a Ξ or an Ω is identified. All results are corrected for inefficiencies and geometrical acceptance before final yields are presented.

3.1 Track finding

A general track reconstruction program called ORHION is developed for the two experiments. The tracking is done using data from the silicon telescope. Charged particles passing through the telescope leave hits in the silicon pixels. The hit information from the pixel detectors gives space points. These points are combined to tracks using the ORHION program. Positively and negatively charged particles bend in opposite directions in the magnetic field, and the electric charge of the particle is found from looking at the bending direction of the track. The momentum of the particle is calculated from the curvature of the track.

The main component of the field is in the z direction (towards the ceiling). Charged particles therefore have trajectories with a helical shape represented by an arc of a circle in the x-y projection, while it is approximated by a straight line in the x-z projection (x being along the beam axis). The procedure for finding a track is to start with combining one hit from the first pixel plane with one hit from the last pixel plane. A hit in the defined mid plane compatible with a particle passing through the telescope is then searched for. If such a hit is found, hits in the other planes are searched for and then added to the track candidate. If the required number of hits is associated with the track candidate, a three-dimensional curve is fitted to the hits, and this curve defines a track. The momentum of the track is calculated from its curvature. Hits included in the track fitting are marked and can not be reused during the rest of the track finding. When all possible tracks with a hit in the first and the last plane are found, also shorter tracks are searched for. In WA97, having only four pixel planes, information from the silicon microstrip detectors was used to improve the track parameters. NA57 had more pixel planes, and the microstrip detectors were not in use.

Each track is required to pass through a certain number of detector planes. This number is optimized for each data sample. If too few hits are required per track, a lot of *ghosts* (fake tracks) are found and stored for further analysis, resulting in a larger fraction of background. On the other hand, if too many hits are required per track, a lot of real tracks are not found due to detector inefficiencies. The number of required hits per track is an example of a parameter that has to be optimized before the analysis starts. A Pb-Pb event with hits and reconstructed tracks in the x-y and x-z projections is shown in figure 3.2. Each hit and each track is given a number, and the positions of the pixel planes are indicated by the dotted lines. The direction of the beam is shown below the figure.

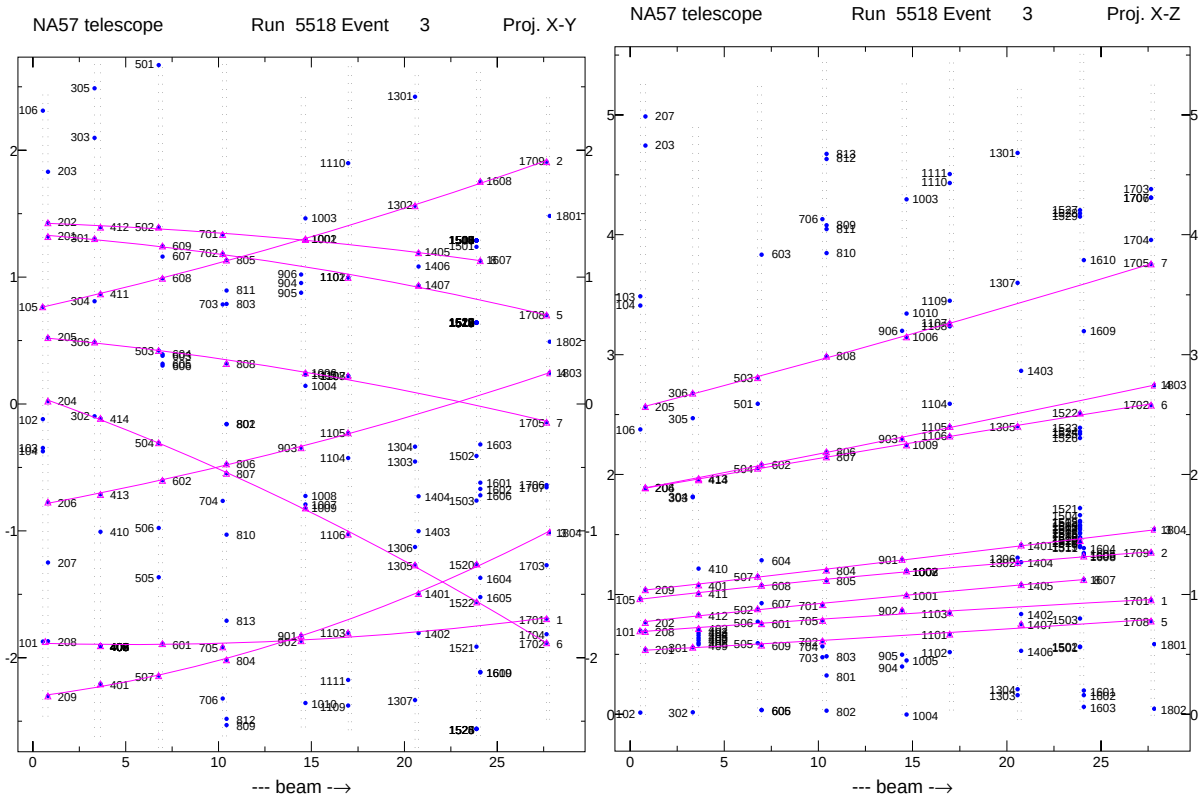

Figure 3.2: Track finding in ORHION. An event display of the planes in the silicon telescope shows hits and fitted tracks in the x-y projection (left) and in the x-z projection (right).

3.2 Reconstruction of primary vertex

The primary vertex is defined as the position where the interaction between the projectile and the target happened. The trajectory of a particle produced in the collision comes from the primary vertex, whereas a secondary particle does not come from the primary vertex. Background reduction is obtained e.g. by extrapolating the secondary particle tracks back to the target plane and requiring a certain distance to the primary vertex.

The philosophy for defining the primary vertex was different for the WA97 and NA57 experiments, and since this has an influence on the results, the methods are described in some detail.

3.2.1 Primary vertex for Pb-Pb collisions

In Pb-Pb collisions there are many charged particles coming from the target. By extrapolating the tracks from the charged particles back to the target plane, an estimate of the position for the primary vertex is found.

WA97

In the Pb-Pb data from the WA97 experiment a primary vertex is found for each event. All charged tracks are traced back to the target plane, and a mean y and z position for all tracks coming from the target is calculated. In a second iteration, all tracks with an impact parameter [1] in the target plane that is too far from the temporary mean position are excluded from the calculation of the final mean position.

NA57

The NA57 experiment is very similar to the WA97 experiment, but as described in section 2.2 it moved from the West Area to the North Area at CERN. The beam line was therefore different for the two experiments. The beam line in the North Area gave a more narrow beam than the beam line in the West Area, and the beam was also moving less during a burst. As a result, the primary vertex position was changing less from event to event in NA57 than in WA97. In WA97 it was necessary to calculate an event by event vertex position. This was not the case in NA57.

In addition, the algorithm of finding a primary vertex for each event becomes inefficient in the new centrality range covered by NA57, where the multiplicity of tracks in the silicon telescope is low. The primary vertex position used in NA57 is therefore an average vertex position for each run. A run is here about half an hour of data taking, or about 200 000 events stored in one single file. The run by run vertex positions are calculated using the same algorithm as for the WA97 event by event vertex positions, but using only high multiplicity events from the selected time period.

The distribution of the event by event vertex positions from the high multiplicity events is fitted with a Gaussian distribution in y and z, and the mean positions are given

[1] The impact parameter is here defined as the distance (perpendicular to the beam direction) between the extrapolated line of flight of a particle and the primary vertex.

as y_{run} and z_{run}. The sigmas of the Gaussian fits are given as $\sigma_{y_{run}}$ and $\sigma_{z_{run}}$, and the values are typically of the order of $\sigma_{y_{run}} \simeq 350\mu$m and $\sigma_{z_{run}} \simeq 650\mu$m.

3.2.2 Primary vertex for p-A collisions

Different methods are used for finding the position of the primary vertex when analysing p-Be and p-Pb collisions. In the thick beryllium target ($\sim$ 3.2 cm) the x-position of the vertex varies from event to event, whereas the x-position in the thin lead target ($\sim$ 0.4 mm) is assumed to be fixed. For p-Be collisions in WA97, a beam telescope consisting of silicon microstrip detectors was placed before the target. Combination of tracks from the beam telescope and the normal tracking telescope were used to localize the primary vertex. This analysis is described in [82]. The beam telescope was not used by NA57. Instead, the position of the primary vertex was found by combining a run-by-run vertex position with the extrapolation of a V^0 line of flight for each event. For the p-Pb data samples, similar methods to the NA57 run by run vertex method are used.

3.3 Reconstruction of V^0 candidates

A V^0 topology is a combination of two charged tracks intersecting in a point at a certain distance from the target. It can in principle represent any neutral particle decaying into two charged particles. In WA97 and NA57 V^0s that can be identified as Λs, $\overline{\Lambda}$s or K^0s are searched for. These particles are again used for identifying Ξs, Ωs and their antiparticles according to the decay topologies shown in figure 3.1. A neutral particle can not be detected directly by the silicon detectors, but the two charged decay particles can be detected and combined to a reconstructed V^0.

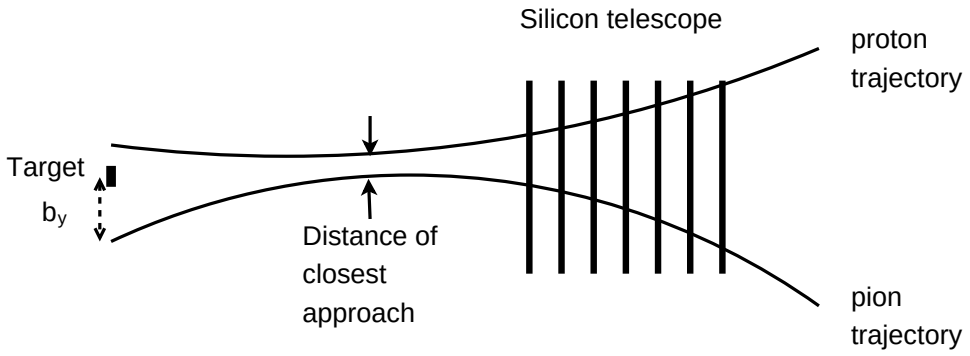

Figure 3.3: Distance of closest approach.

The search for V^0s is included in the ORHION program. This part of the program uses a minimising routine in order to find the *distance of closest approach*. This parameter is defined as the distance that separates the closest points on the two oppositely charged tracks (see figure 3.3). The decay vertex of the V^0 candidate is determined to be half way along the line that joins the two points. A loose cut on the distance of closest approach is made at this stage. The cut is made only to have a coarse selection of events containing

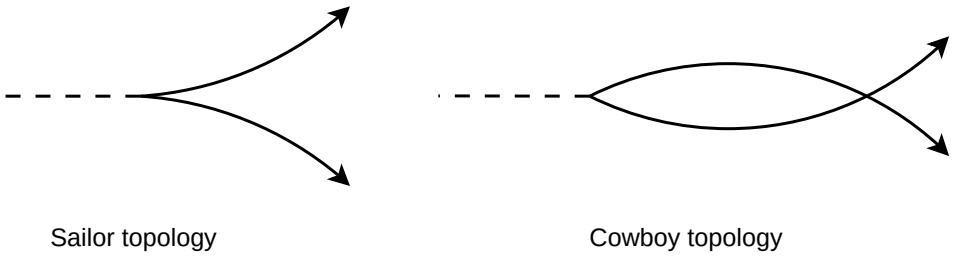

Figure 3.4: Possible configurations for the decay of a V^0.

V^0s, since only these events are stored on tape for further analysis. The cuts used for identifying the different particles may differ slightly, so the cuts should not be too strict at this stage. The maximum distance is normally set to ~ 1 mm (see also section 3.4.1).

Two different topologies are possible for a V^0 candidate. They are called sailor and cowboy topologies (see figure 3.4). In the sailor topology the two tracks leave the decay vertex in the bending direction of the magnetic field. The particles intersect only once in the bending plane. In the cowboy topology the two tracks leave the decay vertex in the opposite direction to which they bend in the magnetic field. The track projections in this case intersect a second time in the bending plane. The experimental setup of WA97 and NA57 favours the cowboy topology since the two tracks in this case are less separated when reaching the relatively narrow telescope. All tracks are normally required to pass through the first and the last plane of the compact part of the telescope, and this is difficult to obtain in the case of sailor topology. The sample of V^0s with a sailor type decay therefore has a low signal/background ratio. To eliminate some background, the V^0 decay is required to be of the cowboy type.

It is required that the V^0 decays at a minimum distance from the target (10 cm for Pb-Pb data in 1998). This is to avoid the large amount of background coming from the combination of any two charged particles produced in the collision. The cut is further described in section 3.4.1.

The transverse momentum of the charged decay particles with respect to the line of flight of the the V^0 is denoted q_{T}. A K^0_S decaying into two charged pions has $q_{\mathrm{T}} \leq 0.206$ GeV/c, and a Λ decaying into a proton and a pion has $q_T \leq 0.101$ GeV/c (see also section 3.4.2). It is required by the ORHION program that $q_T \leq 0.4$ GeV/c. This cut only deselects background outside the Λ and K^0 mass peaks, and does not remove any background from the signal area. However, only geometrical cuts should have been applied in the reconstruction program.

In figure 3.5, the invariant mass $M(p,\pi)$ is plotted for V^0 candidates selected by the ORHION program. The arrow is pointing at the Λ mass ($m_\Lambda = 1.115683$ GeV/c^2). From the measured momenta of the decay particles and assuming their masses, the invariant mass is calculated by

$$M_{invariant} = \sqrt{(E_1 + E_2)^2 - p^2} \tag{3.1}$$

E_1 and E_2 are the energies of the two charged decay particles. p is the momentum of the reconstructed particle calculated by $p^2 = (p_{x1} + p_{x2})^2 + (p_{y1} + p_{y2})^2 + (p_{z1} + p_{z2})^2$, p_{x1} etc. being the momentum components of the charged decay particles. If the reconstructed

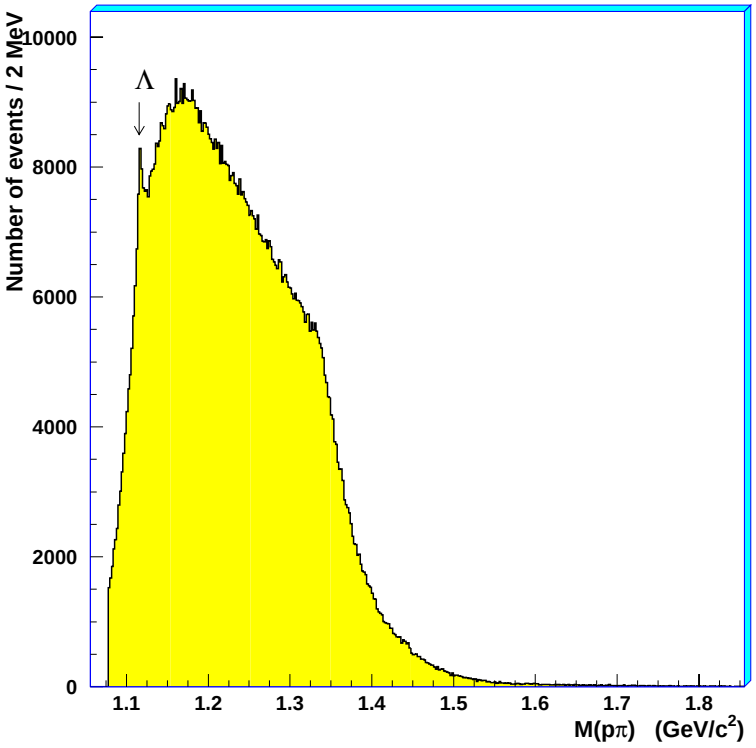

Figure 3.5: The invariant mass $M(p, \pi)$ for V^0 candidates after a coarse selection in the ORHION program.

tracks originate from the decay of the assumed particle, the invariant mass is the correct mass of the particle (within the momentum resolution of the tracking detectors).

3.4 Λ, $\overline{\Lambda}$ and K^0_S reconstruction

In order to select K^0_S, Λ or $\overline{\Lambda}$ from the V^0 candidates, a number of selection criteria have been applied to minimize the number of false identified particles in the final samples. The selection criteria are set after a systematic study of the data sample. The cuts are introduced one by one, and finally every cut is checked by comparing the outcome with and without including the cut that is being studied. All other cuts are kept at the selected value. This is done to avoid overlapping cuts. Cut values are selected in such a way that as much background as possible is eliminated without reducing the signal level more than strictly necessary. One should also be careful not to introduce any systematic errors when making the cuts. This is discussed further in section 4.7.

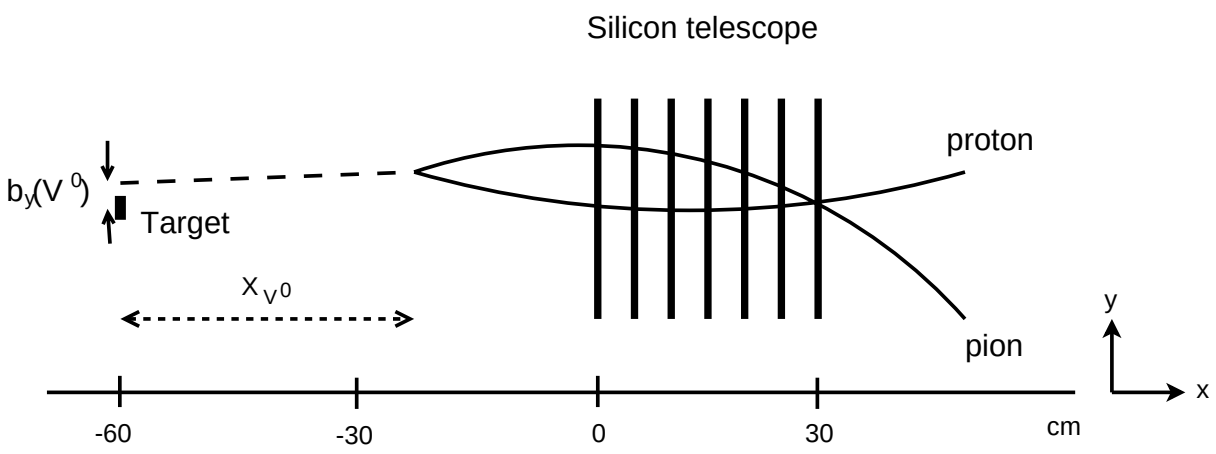

Figure 3.6: Illustration of x position of V^0 decay and impact parameter for V^0.

3.4.1 General description of selection criteria

The experimental conditions for the different periods of running are slightly different. As a result, the cuts are set at different values for different data samples. Although the values are different, the parameters used for the selection are mainly the same for all data samples. The general cuts for the selection of Λ, $\overline{\Lambda}$ and K^0_S in WA97 and NA57 are discussed, and the values for the 1998 lead data sample are presented. All cuts described here are made in addition to the selection criteria for the V^0 candidates described in section 3.3.

X position of V^0 decay

A cut is made in the x position of the V^0 decay, x_{V^0}, shown in figure 3.6. The coordinate system used is the Goliath reference system. This has its center in the center of the magnet. In the period of running discussed here, the target was located at $x = -60$ cm. A lot of charged particles are produced in the target region, and the risk that two uncorrelated tracks coming from the target can be combined to a fake V^0 is therefore large. To remove this background from the data sample, only V^0 candidates with an x position of the decay at a certain distance from the target are selected, here $x_{V^0} \geq -30$ cm. The first plane of the silicon telescope is positioned at $x = 0$. Particles interacting inside the telescope can produce charged particles that are identified as V^0s. The charged tracks are also required to pass through all the detector planes in the compact part of the telescope. It is therefore required that $x_{V^0} \leq -0.5$ cm.

In figure 3.7a) the x position of the decay of a selection of Λ and $\overline{\Lambda}$ candidates from Pb-Pb collisions is shown. The correlation to the invariant mass M(p,π) for the same candidates is shown in figure 3.7b). In both figure a) and b) all other final cuts (described in the following sections) are included, only the cut described here is left out. A cut at $x_{V^0} \geq -50$ (10 cm from the target) is already done in the ORHION program. The mass of Λ and $\overline{\Lambda}$ is 1115.683 ± 0.006 MeV [3]. The figure shows that the distribution is centred around this value. The cuts are indicated by lines in the figure. Only particles with x_{V^0}

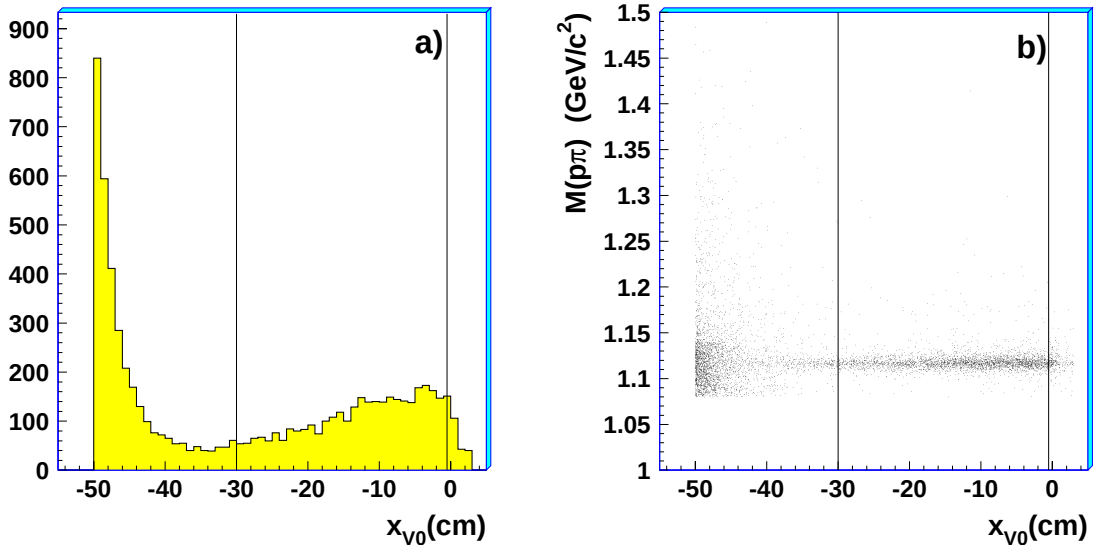

Figure 3.7: In a), the distribution of the decay vertex of the V^0 for the Λ and $\overline{\Lambda}$ candidates. In b), the correlation between the invariant mass, $M(p\pi)$, and the decay vertex of the V^0. The selection criteria are indicated by vertical lines.

between the two lines are selected.

Distance of closest approach

This cut is already described in section 3.3 and is illustrated in figure 3.3. A loose cut is made in the ORHION program, but a tighter cut is needed in order to eliminate background for the different particles. Figure 3.8 shows a) the distribution of the distance of closest approach for a selection of Λ and $\overline{\Lambda}$ candidates from Pb-Pb collisions, and b) the correlation to the invariant mass M(p,π) for the same candidates. The cut applied to this data sample is indicated by a line in the figure. Only candidates with a distance of closest approach smaller than 0.03 cm are selected.

Impact parameter for V^0

The decay vertex of the V^0 candidate is determined by the distance of closest approach. The momenta of the charged tracks are calculated from the curvature of the tracks. The momentum of the V^0 is calculated from the momenta of the charged tracks. Knowing the decay point and the momentum of the track, the 'invisible' track from the V^0 is extrapolated back to the target plane, and the impact parameter is found. The y and z components of the impact parameter are denoted b_{yV^0} and b_{zV^0}. The parameter is illustrated in figure 3.6. In figure 3.9 the V^0 impact parameter is plotted for a selection of Λ and $\overline{\Lambda}$ candidates.

Rather than making a square cut in the y and z direction of this parameter an elliptic cut is made, illustrated by the ellipse in the figure. σ_y and σ_z are the same as $\sigma_{y_{run}}$ and $\sigma_{z_{run}}$ for the primary vertex calculation described in section 3.2. The selection criterion

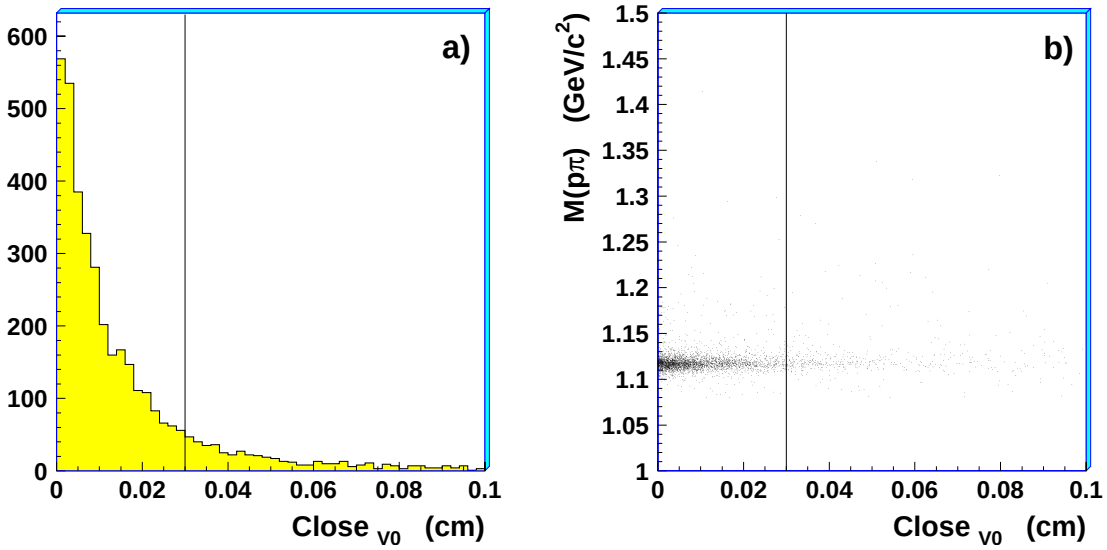

Figure 3.8: In a), the distribution of the distance of closest approach for the V^0 decay tracks for the Λ and $\overline{\Lambda}$ candidates is shown. In b), the correlation between the invariant mass, $M(p\pi)$, and the distance of closest approach for the V^0 decay tracks is shown. The selection criterion is indicated by a vertical line in each figure.

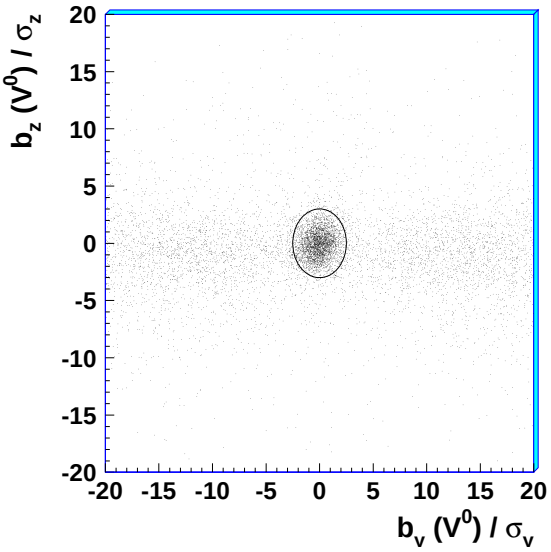

Figure 3.9: Distribution of the impact parameter for V^0 line of flight for the Λ and $\overline{\Lambda}$ candidates. The elliptic cut is indicated in the figure.

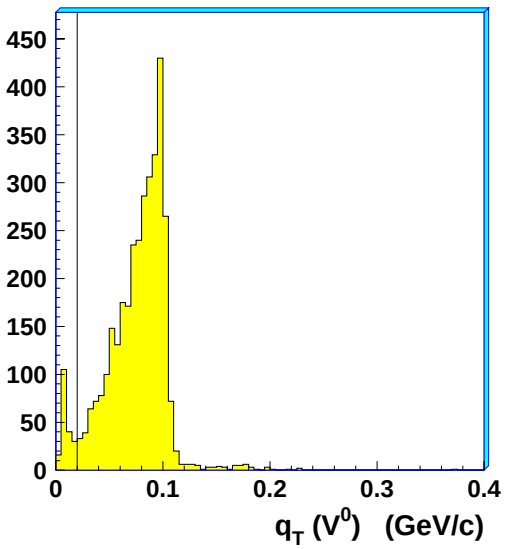

Figure 3.10: Distribution of the transverse momentum of the decay tracks relative to the momentum of the V^0 for Λ and $\overline{\Lambda}$ candidates. The selection criterion for the lower value is indicated by the vertical line in the figure.

is here

$$\left[\frac{b_{yV^0}}{2.5 \cdot \sigma_{y_{run}}}\right]^2 + \left[\frac{b_{zV^0}}{3.0 \cdot \sigma_{z_{run}}}\right]^2 < 1 \tag{3.2}$$

Impact parameter of the charged tracks

The impact parameter of a charged track is found by extrapolating it back to the target plane and calculating the distance from the intersection point to the primary vertex. No cut was made in the impact parameters for the charged decay tracks from Λs and $\overline{\Lambda}$s in the 1998 data sample, but was introduced for the selection of K^0_S (see section 3.4.4).

Transverse momentum of the decay tracks

The transverse momentum of the charged particles with respect to the line of flight of the V^0, q_T, is already discussed in section 3.3. In addition to the upper cut at 0.4 GeV/c discussed earlier, a cut at low q_T is introduced at this stage to remove V^0 candidates coming from gamma conversions, $\gamma \rightarrow e^+e^-$. As shown in figure 3.10, the selection criterion is $q_T \geq 0.02$ GeV/c. The upper cut at 0.4 GeV/c introduced before the geometrical cuts should have been omitted, and would probably not have be necessary after the geometrical cuts.

Internal decay angles

In order to define the internal decay angles of a V^0, a new coordinate system $x'y'z'$ is defined such that x' is in the direction of the V^0 line of flight. The y' axis is chosen to be

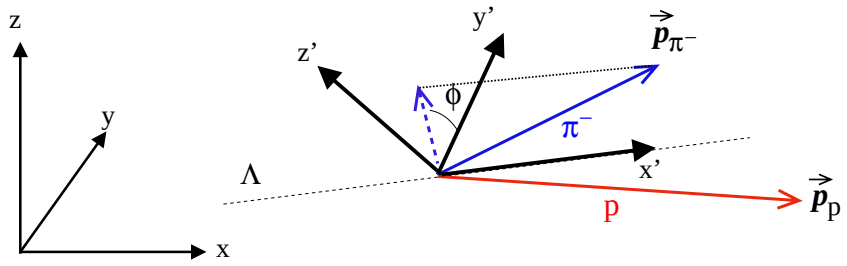

Figure 3.11: Definition of the internal decay angle, ϕ, in the case of a Λ decay.

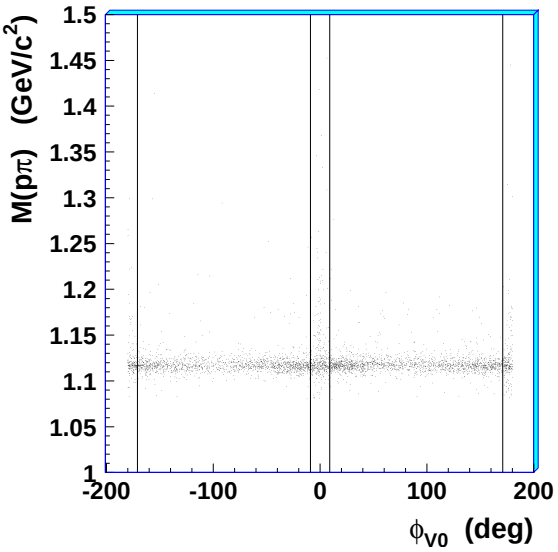

Figure 3.12: The correlation between the invariant mass, $M(p\pi)$, and the internal decay angle, ϕ_{V^0}, for the two polarities of the magnetic field plotted together. The selection criteria are indicated by vertical lines.

parallel to the original xy plane. The direction of z' is such that the coordinate system is right handed. The internal azimuthal decay angle of the V^0, ϕ_{V^0}, is defined as the angle between the projection of the momentum of the negative track in the $y'z'$ plane and the y' axis (see figure 3.11). The cuts at $|\phi_{V^0}| > 9°$ (magnetic field pointing downwards) and at $|\phi_{V^0}| < 171°$ (magnetic field pointing upwards) are illustrated in figure 3.12, where the correlation between $|\phi_{V^0}|$ and the invariant mass, $M(p\pi)$, is plotted for a set of Λ candidates.

3.4.2 Selection of K^0_S, Λ and $\overline{\Lambda}$

All cuts in the previous subsection are general cuts for K^0, Λ and $\overline{\Lambda}$, and do not distinguish between these particles. The values referred to are those used for Λ and $\overline{\Lambda}$ in the lead data sample from 1998. The values for K^0 are similar (see section 3.4.4). In order to

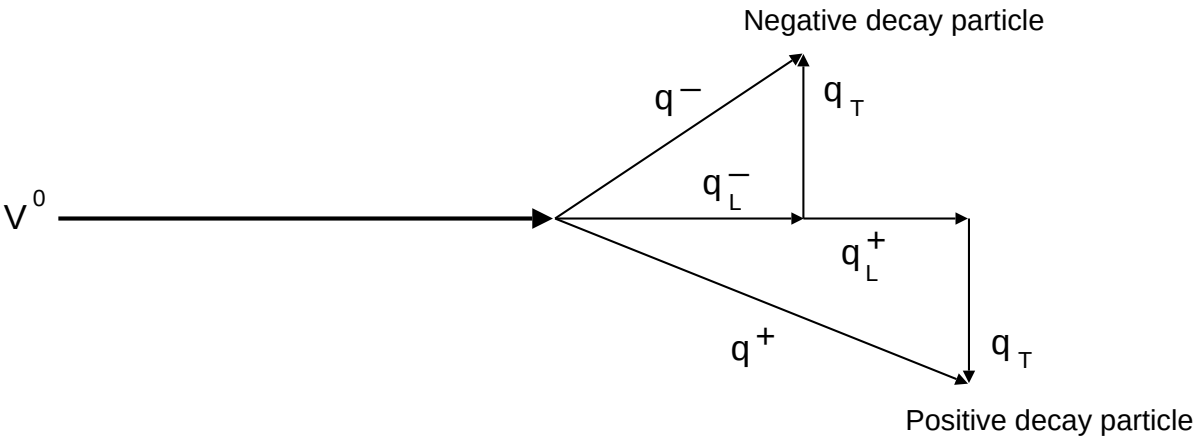

Figure 3.13: V^0 decay kinematics.

identify the candidates as Λ, $\overline{\Lambda}$ or K^0, the Podolanski-Armenteros variables α and q_T [83] are used. The variable α is defined as

$$\alpha = \frac{q_L^+ - q_L^-}{q_L^+ + q_L^-} \tag{3.3}$$

where q_L^+ is the momentum of the positive decay track along the V^0 line of flight, and q_L^- is the momentum of the negative decay track along the V^0 line of flight. q_T is the momentum of the decay track transverse to the V^0 line of flight. An illustration of the V^0 decay kinematics is given in figure 3.13.

A Λ is identified from the decay into a proton and a π^-. Since the mass of the proton is much larger than the mass of the π^-, the momentum of the proton is much larger than the momentum of the π^- in the laboratory system, and therefore α is positive. An $\overline{\Lambda}$ decays into an antiproton and a π^+, so the momentum of the positive track is smaller than the momentum of the negative track in the laboratory system, and α is negative. This separates Λs from $\overline{\Lambda}$s. K^0 decays into a π^- and a π^+. For K^0s, α has a distribution centred around $\alpha = 0$ as illustrated in figure 3.14.

Figure 3.15 shows an experimental Podolanski-Armenteros plot for a selection of V^0 candidates from the 1998 Pb-Pb data sample. Λs are selected requiring $\alpha > 0.45$, and $\overline{\Lambda}$s requiring $\alpha < -0.45$. In figure 3.15 the V^0 candidates at low q_T originating from gamma conversions are not excluded. All other previously described cuts are applied to the presented data sample.

$\mathbf{K^0}$ mass cut

As seen from figure 3.15, there is a considerable amount of $\mathrm{K^0}$s in the sample of Λ and $\overline{\Lambda}$ candidates. A cut around the $\mathrm{K^0}$ mass is therefore applied in the Λ and $\overline{\Lambda}$ selection. Figures 3.16 a) and b) show the invariant mass for the $\mathrm{K^0}$ hypothesis, $M(\pi^+, \pi^-)$, for Λ and $\overline{\Lambda}$ candidates respectively. The $\mathrm{K^0}$ mass cut is indicated by lines in the figures. The plots show only Λ and $\overline{\Lambda}$ candidates where $0.45 < |\alpha| < 0.65$. In this interval the Λs and the $\overline{\Lambda}$s are relatively well separated from the $\mathrm{K^0}$s, so the decision on where to make the

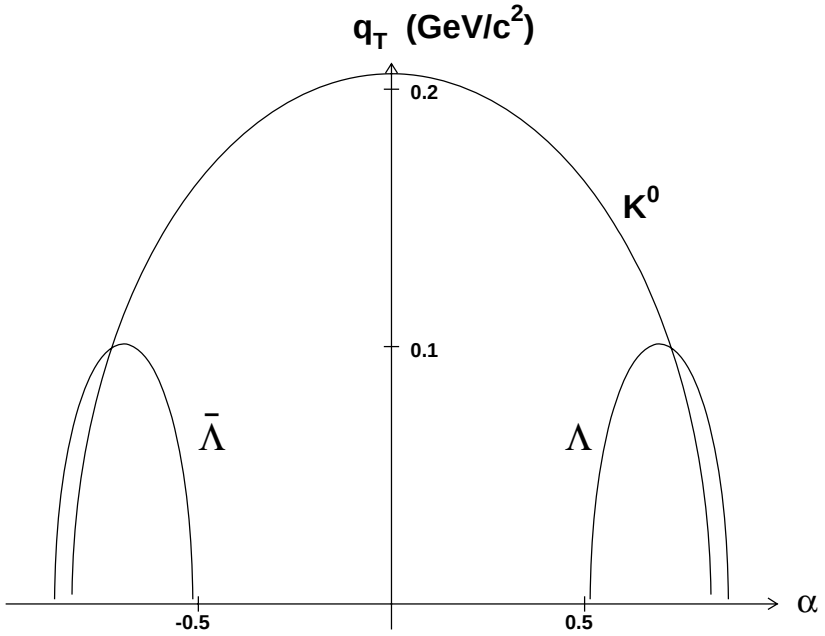

Figure 3.14: Podolanski-Armenteros curves for K^0, Λ and $\overline{\Lambda}$.

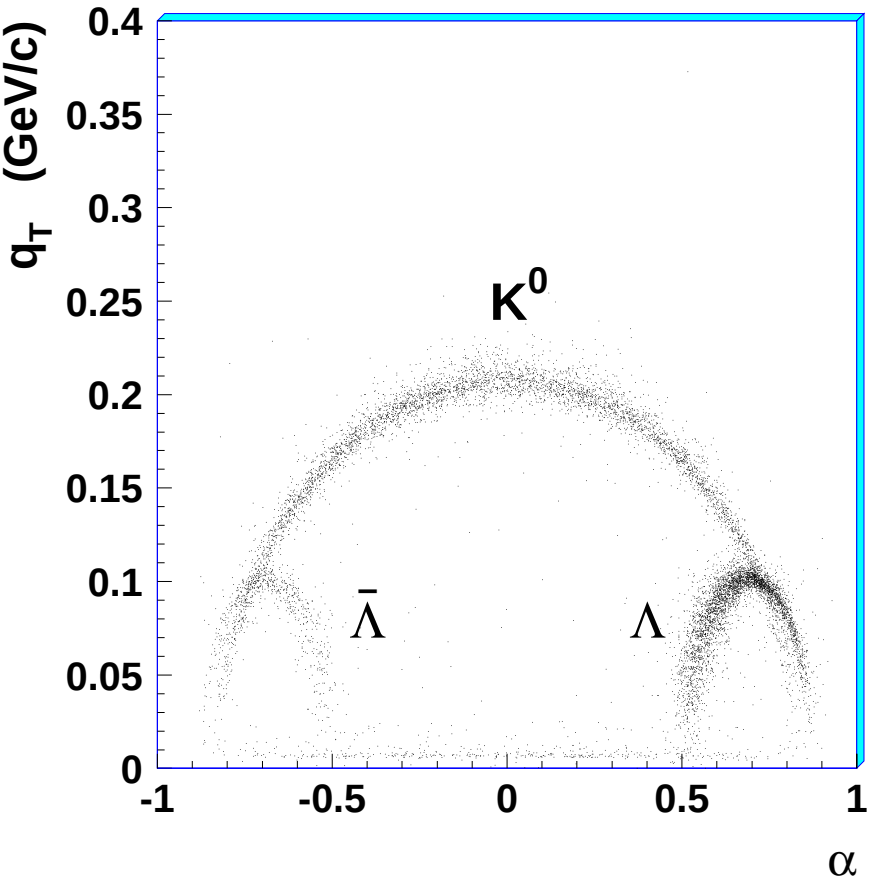

Figure 3.15: Experimental Podolanski-Armenteros plot for V^0 candidates.

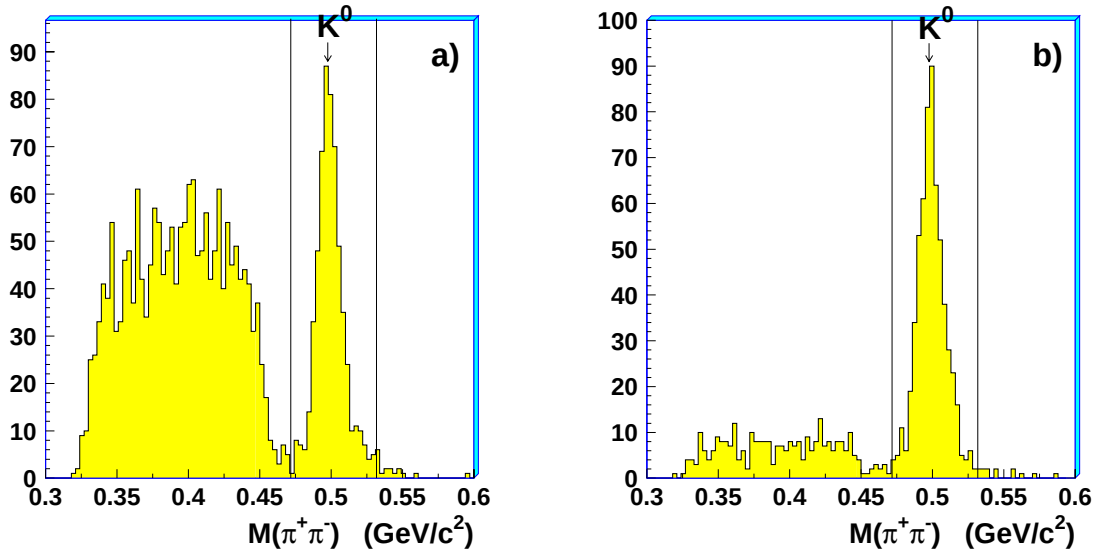

Figure 3.16: The invariant mass $M(\pi^+, \pi^-)$ for a selection of a) Λ and b) $\overline{\Lambda}$ candidates. A cut around the K^0 mass is indicated.

K^0 mass cut becomes easier. The reconstructed K^0 mass is slightly shifted compared to the table value. A similar shift has been observed by several other Omega experiments. Due to this systematic error, the cut is slightly asymmetric around the table value of the K^0 mass.

As seen from figure 3.16, the cut is especially important for the $\overline{\Lambda}$ selection. In figure 3.17 the invariant mass for the Λ or $\overline{\Lambda}$ hypothesis, $M(p, \pi)$ is plotted as a function of the invariant mass for the K^0 hypothesis, $M(\pi^+, \pi^-)$. The cut around the K^0 mass is again indicated by vertical lines. Both Λ and $\overline{\Lambda}$ candidates are included in this plot. In the 1998 Pb-Pb data sample it is required that $M(\pi^+, \pi^-) > m_{K^0} + 0.034\,\mathrm{GeV}/c^2$ and that $M(\pi^+, \pi^-) < m_{K^0} - 0.026\,\mathrm{GeV}/c^2$, where $m_{K^0} = 497.65$ MeV/c^2 is the table value of the mass of the K^0 [3].

Figure 3.18 shows the final Λ and $\overline{\Lambda}$ samples after all cuts, including the low q_T cut and the K^0 mass cut.

3.4.3 Final selection of Λ and $\overline{\Lambda}$

The selection criteria for Λ and $\overline{\Lambda}$ from the Pb-Pb data sample collected by the NA57 experiment in 1998 are summarized here:

- Both decay tracks pass through the first and the last plane in the compact part of the telescope
- The distance of closest approach is smaller than 0.03 cm
- Only cowboy topology is accepted
- The decay is in the interval -30 cm $< x_{V^0} <$ -0.5 cm

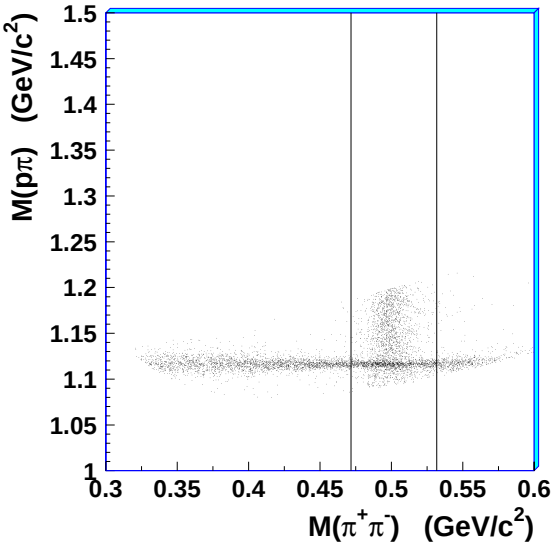

Figure 3.17: The invariant mass $M(p,\pi)$ plotted as a function of the $M(\pi^+,\pi^-)$ for Λ and $\overline{\Lambda}$ candidates. A cut around the K^0 mass is indicated by vertical lines.

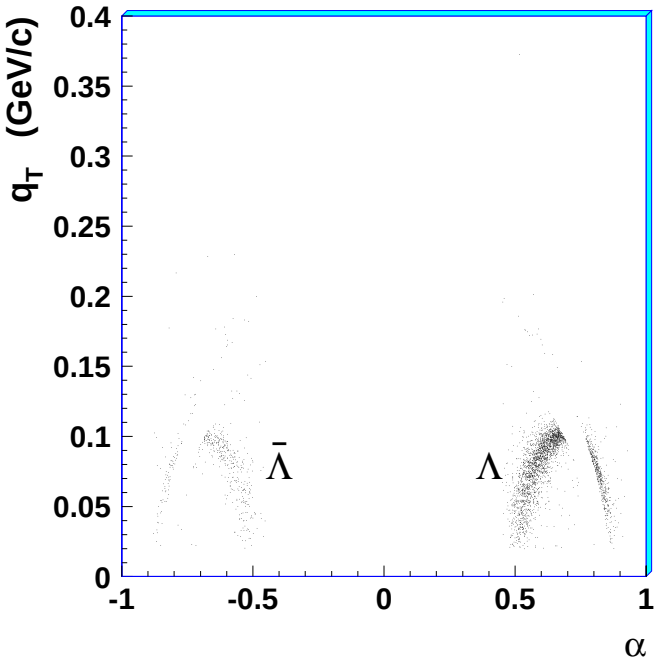

Figure 3.18: Podolanski-Armenteros plot for the final Λ and $\overline{\Lambda}$ sample.

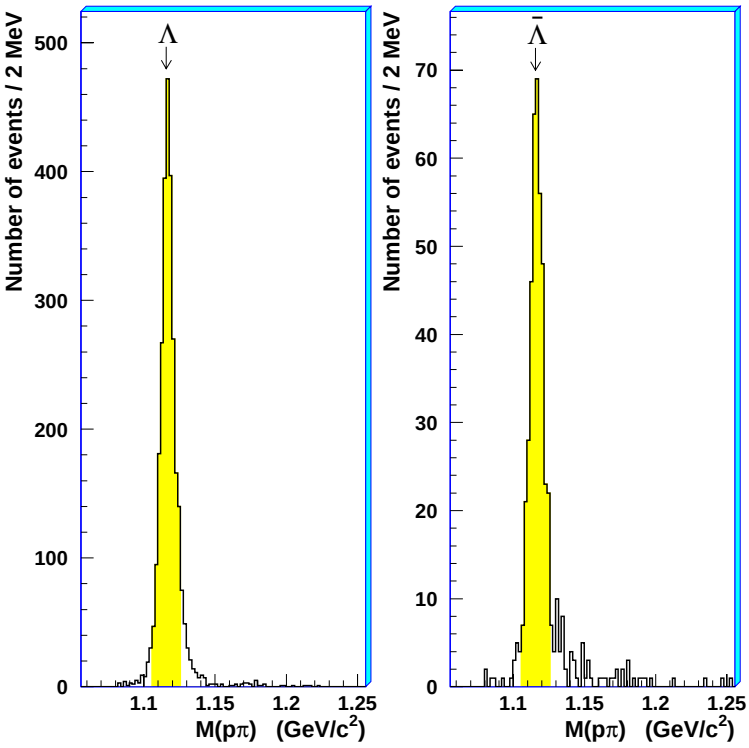

Figure 3.19: Final invariant mass plots for Λ (left) and $\overline{\Lambda}$ (right).

- The V^0 trajectory points back to the target, $\left[\frac{b_{yV^0}}{2.5 \cdot \sigma_{y_{run}}}\right]^2 + \left[\frac{b_{zV^0}}{3.0 \cdot \sigma_{z_{run}}}\right]^2 < 1$
- The transverse momentum of the charged tracks relative to the momentum of the V^0 is in the interval $0.02\ \mathrm{GeV}/c < q_T < 0.4\ \mathrm{GeV}/c$
- The internal decay angle $|\phi_{V^0}| > 9^\circ$ (magnetic field pointing downwards) or $|\phi_{V^0}| < 171^\circ$ (magnetic field pointing upwards)
- The Podolanski-Armenteros variable $\alpha > 0.45$ (Λ) or $\alpha < -0.45$ ($\overline{\Lambda}$)
- Exclude K^0s, $M(\pi^+, \pi^-) > m_{K^0} + 0.034\,\mathrm{GeV}/c^2$ or
  $M(\pi^+, \pi^-) < m_{K^0} - 0.026\,\mathrm{GeV}/c^2$

The invariant mass plots for the selection of Λ and $\overline{\Lambda}$ are shown in figure 3.19. As seen from the figure, the residual background is very low. For the final selection of particles used for further analysis, a cut in the invariant mass is included. For the 1998 Pb-Pb data sample, particles fulfilling the criterion $|M(p,\pi) - m_\Lambda| < 0.010\,\mathrm{GeV}/c^2$ are selected. This is indicated by the yellow (shaded) area in the histogram.

3.4.4 Final selection of K^0

The selection criteria for K^0_S from the Pb-Pb data sample collected by the NA57 experiment in 1998 is summarized here:

- Both decay tracks pass through the first and the last plane in the compact part of the telescope
- The distance of closest approach is smaller than 0.035 cm
- Only cowboy topology is accepted
- The decay is in the interval -42 cm $< x_{V^0} <$ -0.5 cm
- The V^0 trajectory points back to the target, $\left[\frac{b_{yV^0}}{2.5\cdot\sigma_{yrun}}\right]^2 + \left[\frac{b_{zV^0}}{2.5\cdot\sigma_{zrun}}\right]^2 < 1$
- The charged tracks do not point back to the target and is on the correct side of the target, $\pm b_{y_{\pi^+}} < -0.2$ cm and $\pm b_{y_{\pi^-}} > 0.2$ cm,
  where the sign is positive for positive magnetic field and negative for negative magnetic field
- The transverse momentum of the charged tracks relative to the momentum of the V^0 is in the interval 0.04 GeV/$c < q_T <$ 0.4 GeV/c
- The internal decay angle $|\phi_{V^0}| > 9^\circ$ (magnetic field pointing downwards) or $|\phi_{V^0}| < 171^\circ$ (magnetic field pointing upwards)

The invariant mass plot for the selection of K^0 is shown in figure 3.20. For the final selection of particles used for further analysis, a cut in the invariant mass is included. The experimental mass peak for K^0 is slightly shifted, and the cut is therefore asymmetric around the table value of the K^0 mass. For the 1998 Pb-Pb data sample, particles fulfilling the criterion $m_{K^0} - 0.0134\,\mathrm{GeV}/c^2 < M(\pi^+,\pi^-) < m_{K^0} + 0.0166\,\mathrm{GeV}/c^2$ are selected. This is indicated by the yellow (shaded) area in the histogram.

3.5 Cascade reconstruction

This section contains a summary of the selection criteria for Ξ and Ω identification in the WA97 and NA57 experiments. The cuts are defined similar to the Λ and K^0 cuts. The specific values of the cuts are those used in the analysis of the Pb-Pb data sample from 1998. For other data samples, similar cuts are applied.

3.5.1 Ξ identification

A Ξ has to satisfy these selection criteria:

- All three decay tracks pass through the first and the last plane of the compact part of the telescope

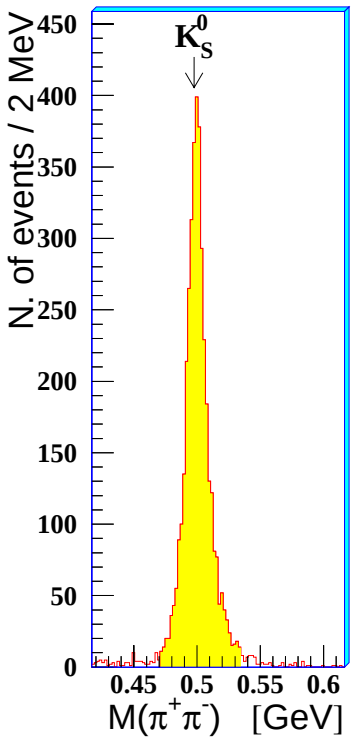

Figure 3.20: Final invariant mass plot for K^0.

- The distance of closest approach between the trajectory of the pion and the line of flight of the V^0 is smaller than 0.05 cm
- Only cowboy topologies are accepted for the Ξ decay
- The Ξ decay is in the interval -40 cm $< x_\Xi <$ -3 cm
- The Ξ decays before the V^0, $x_\Xi < x_{V^0}$
- The Ξ trajectory points back to the primary vertex position,

$$\left[\frac{b_{y\Xi}}{3\cdot\sigma_{y_{run}}}\right]^2 + \left[\frac{b_{z\Xi}}{3\cdot\sigma_{z_{run}}}\right]^2 < 1$$

- The impact parameter of the V^0 is different from the Ξ impact parameter and is on the correct side:

$$(b_{yV^0} - b_{y\Xi})\cdot(\pm 1) < -0.2\,cm \;\; (\Xi^-) \quad or \quad (b_{yV^0} - b_{y\Xi})\cdot(\pm 1) > 0.2\,cm \;\; (\overline{\Xi}^+)$$

  The sign is positive when the magnetic field points upwards, and negative when the field points downwards

- The impact parameter of the π is on the correct side of the Ξ impact parameter:

$$(b_{y\pi} - b_{y\Xi})\cdot(\pm 1) > 0cm \;\; (\Xi^-) \quad or \quad (b_{y\pi} - b_{y\Xi})\cdot(\pm 1) < 0cm \;\; (\overline{\Xi}^+)$$

  The sign is positive when the magnetic field points upwards, and negative when the field points downwards

- The internal decay angle of the Ξ $\cos\theta^*_\Xi > -0.9$, where θ^* is the angle between the momentum of the Λ and the line of flight of the Ξ
- Internal decay angles of the Ξ and V^0 $|\phi_{V^0}| > 0.2$ rad or $|\phi_\Xi| > 0.2$ rad

In addition, to select the Λ of the Ξ decay, these criteria were applied to the V^0 candidates:

- The distance of closest approach between the trajectories of the two charged decay tracks < 0.035 cm
- Only cowboy topology is accepted for the V^0 decay
- The V^0 decay is in the interval -30 cm $< x_{V^0} <$ 0 cm
- The transverse momentum of the charged tracks relative to the momentum of the V^0 is in the interval $0.02\ \mathrm{GeV}/c < q_T < 0.4\ \mathrm{GeV}/c$
- Select Λs or $\overline{\Lambda}$s: $\alpha > 0.45$ (Ξ^-) or $\alpha < -0.45$ $(\overline{\Xi}^+)$
- The invariant mass for the Λ $(\overline{\Lambda})$ candidate, $M(p,\pi)$, is in the interval $m_\Lambda - 0.012\,\mathrm{GeV}/c^2 < M(p,\pi) < m_\Lambda + 0.015\,\mathrm{GeV}/c^2$

The invariant mass plots for Ξ^- and $\overline{\Xi}^+$ after the above selection criteria, are shown in figure 3.21. The final selection of particles used for further analysis requires the invariant mass $M(\Lambda,\pi)$ to be in the interval $m_\Xi - 0.015\,\mathrm{GeV}/c^2 < M(\Lambda,\pi) < m_\Xi + 0.020\,\mathrm{GeV}/c^2$ where $m_\Xi = 1321$ MeV. The interval is indicated by the yellow (shaded) area in the figure.

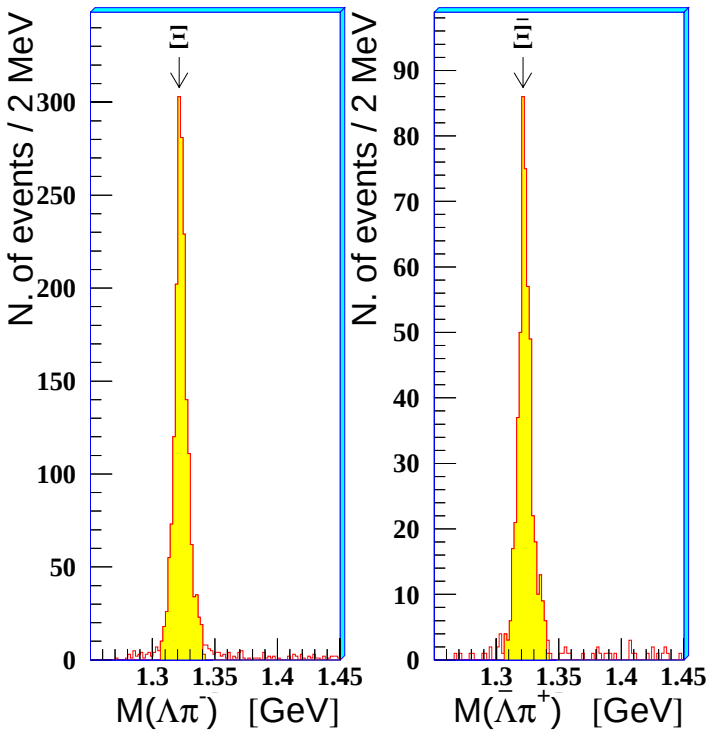

Figure 3.21: Final invariant mass plots for Ξ^- (left) and $\overline{\Xi}^+$ (right).

3.5.2 Ω identification

An Ω has to satisfy these selection criteria:

- All three decay tracks pass through the first and the last plane of the compact part of the telescope
- The distance of closest approach between the trajectory of the kaon and the line of flight of the V^0 is smaller than 0.03 cm
- Only cowboy topologies are accepted for the Ω decay
- The Ω decay is in the interval -40 cm $< x_\Omega <$ 0 cm
- The Ω decays before the V^0, $x_\Omega < x_{V^0} - 0.2$ cm
- The Ω trajectory points back to the primary vertex position,

$$\left[\frac{b_{y\Omega}}{3 \cdot \sigma_{y_{run}}}\right]^2 + \left[\frac{b_{z\Omega}}{3 \cdot \sigma_{z_{run}}}\right]^2 < 1$$

- The internal decay angle of the Ω $\cos\theta^*_\Omega < 0.8$, where θ^* is the angle between the momentum of the Λ and the line of flight of the Ω
- Internal decay angles of the V^0 and the Ω $|\phi_{V^0}| > 0.15$ rad or $|\phi_\Omega| > 0.15$ rad
- Transverse momentum of the decay tracks from the Ω relative to the Ω line of flight $q_{T_\Omega} > 0.12$ GeV/c
- Deselection of Ξs, $M(\Lambda,\pi) < m_\Xi - 0.020\,\mathrm{GeV}/c^2$ or $M(\Lambda,\pi) > m_\Xi + 0.030\,\mathrm{GeV}/c^2$

In addition, to select the Λ of the Ω decay, these criteria were applied to the V^0 candidates:

- The distance of closest approach between the trajectories of the two charged decay tracks $<$ 0.025 cm
- Only cowboy topology is accepted for the V^0 decay
- The V^0 decay is in the interval -27 cm $< x_{V^0} <$ 0 cm
- The transverse momentum of the charged tracks relative to the momentum of the V^0 is in the interval 0.03 GeV/c $< q_{T_{V^0}} <$ 0.4 GeV/c
- Select Λs or $\overline{\Lambda}$s: $\alpha > 0.45$ (Ω^-) or $\alpha < -0.45$ ($\overline{\Omega}^+$)
- The invariant mass $M(p,\pi)$ is in the interval $|M(p,\pi) - m_\Lambda| < 0.008\,\mathrm{GeV}/c^2$

The invariant mass plots for Ω^- and $\overline{\Omega}^+$ after the above selection criteria, are shown in figure 3.22. The final selection of particles used for further analysis requires the invariant mass $M(\Lambda,K)$ to be in the interval $|M(\Lambda,K) - m_\Omega| < 0.017\,\mathrm{GeV}/c^2$. The interval is indicated by the yellow (shaded) area in the figure. The figure includes Ωs from the 158 GeV/c data collected in 1998 and in 2000.

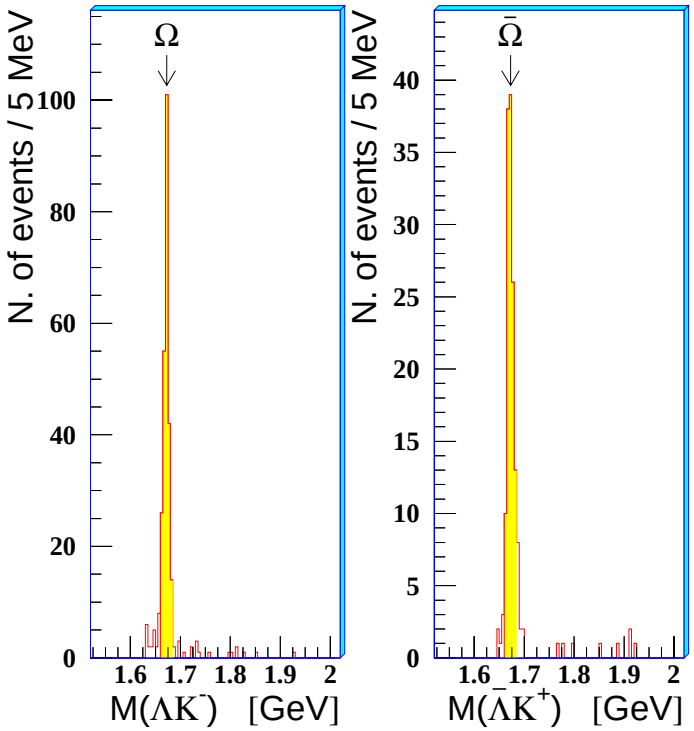

Figure 3.22: Final invariant mass plots for Ω^- (left) and $\overline{\Omega}^+$ (right).

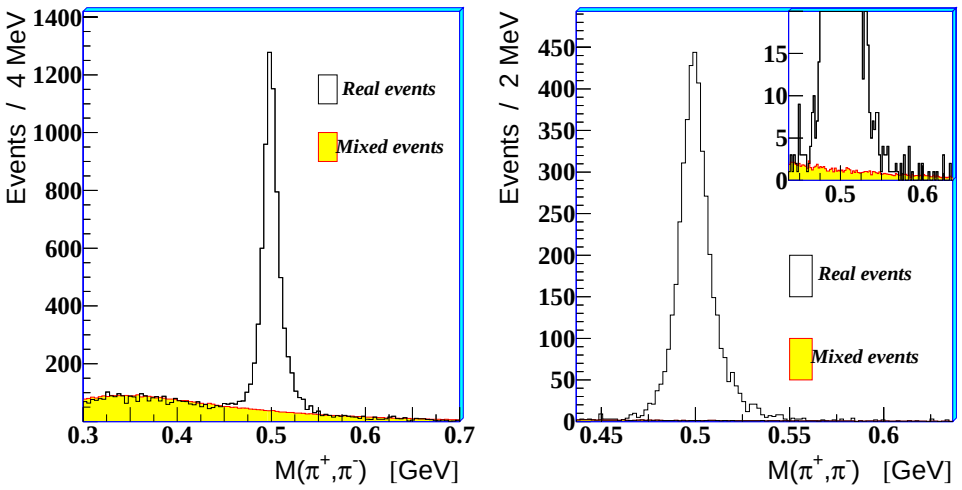

Figure 3.23: The invariant mass distribution $M(\pi^+, \pi^-)$ for real and mixed events before (left) and after (right) analysis cuts.

3.6 Estimation of background

The mass spectra shown in the previous section show a very low background. Still, a detailed study has been done to estimate the residual combinatorial background. For K^0 Λ and $\overline{\Lambda}$ fake V^0s have been created by pairing all negative particles from one event with all positive particles from another event (event mixing). The two events have similar multiplicities. The fake V^0s are analysed as normal events with the analysis programs described earlier in this chapter and shown in figure 4.1. This provides an estimate of the combinatorial background. Absolute normalization is fixed by the number of pairs of oppositely charged particles in real and mixed events.

Figure 3.23 shows the invariant mass plot, $M(\pi^+, \pi^-)$, for K^0 candidates before (left) and after (right) the final analysis cuts are applied. The plots contain both real and mixed events. The estimated residual background after the analysis cuts is shown to be very small. Using the event mixing method, the total amount of combinatorial background is estimated to be 0.7% for K^0_S, 0.3% for Λ and 1.2% for $\overline{\Lambda}$. The residual background for the Ξ and Ω has been estimated using a similar technique, and is found to be less than 4% for Ξ and less than 6% for Ω. The residual background has been neglected in the further analysis.

Chapter 4

Corrections

In the collisions studied by WA97 and NA57 a number of particles are produced, ranging from only a few in p-Be collisions, to some thousand in Pb-Pb collisions at 158 GeV/c per nucleon. The WA97 and NA57 detectors are covering only a small part of the total phase space, i.e. only a small fraction of the produced particles actually pass through the detectors. The number of produced particles not measured experimentally is estimated and corrected for in the final results.

A perfect detector would give a signal for all particles passing through it. The silicon pixel detectors used by WA97 and NA57 started out being 98-99% efficient. After being used many times, the overall efficiency is reduced to 80-90%. In addition, the analysis programs are not able to identify all tracks made by real particles, and some fake tracks from noise or wrong combinations of hits are found. The detector and tracking inefficiencies are corrected for in the final results.

Another correction factor comes from feed-down. An example of feed-down is a Ξ^- decaying into a Λ and a π^-. This Λ could be reconstructed as a particle coming directly from the interaction, and therefore be counted as a Λ even if it is a secondary particle. Ideally one should only count Λs that are produced in the reaction zone, and not Λs that are decay products produced after chemical freeze-out. In the WA85 experiment [84] feed-down corrections were important because of the relatively long distance between the target and the tracking detectors. Correcting for feed-down leads to an increase of the measured $\overline{\Xi}^+/\overline{\Lambda}$ ratio. In WA97 and NA57 however, the distance between the target and the tracking detectors was so short that the effects of feed-down are neglected. In addition, part of the feed-down is removed by requiring that the Λ comes from the target. Since the position resolution of WA97/NA57 is much better than for WA85, this also improves the WA97/NA57 results. For WA97 the feed-down for Λ and $\overline{\Lambda}$ is estimated to be less than 5% and 10% respectively. The Λ sample is not corrected for feed-down from $\Sigma^0 \rightarrow \Lambda + \gamma$.

4.1 Correction procedure

In the previous experiments, WA85 and WA94, corrections for geometrical acceptance and efficiencies were done by applying two separate correction factors. One factor containing the geometrical acceptance, and one containing the reconstruction efficiencies,

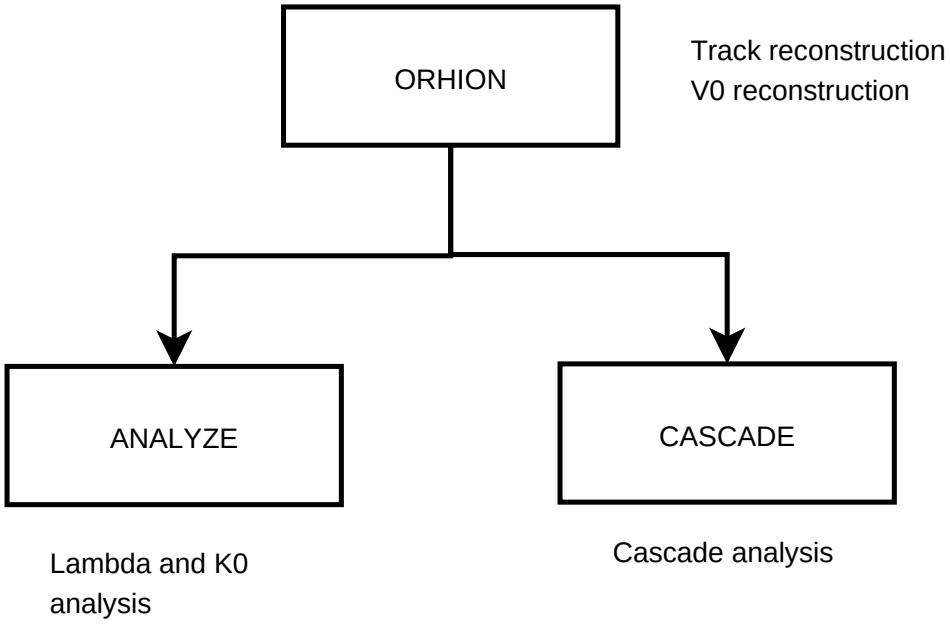

Figure 4.1: Sketch showing analysis programs used by WA97/NA57.

depending on the detector efficiencies (see e.g. [85]). These two experiments used wire chambers and silicon strip detectors which provided two-dimensional readout. When the hit multiplicity increased, the number of combinations of points possible for making a track increased dramatically. The reconstruction efficiencies therefore depended heavily on the multiplicity of the event, and the efficiencies were given as a function of the event multiplicity. The efficiencies depended only weakly on other parameters, for instance rapidity or transverse momentum. These parameters influenced the geometrical acceptance only.

The WA97 and NA57 experiments used pixel detectors for reconstructing the tracks. WA97 also use silicon strip detectors, but only for improving the quality of the track already found by the pixels. The pixel detectors give information about all three space coordinates. The three-dimensional track finding is much less depending on the hit multiplicity than the two-dimensional track finding was. Instead, the detector efficiencies become important, since they vary over the sensitive region of a plane. The most important parameter is now the exact position of the hit in the telescope, and not the density of hits. This is difficult to correct for when using only acceptance and efficiency tables. The strategy for correcting the WA97 and NA57 results is therefore changed compared to the earlier experiments. Individual correction factors are calculated for each identified particle.

Correction factors, weights, are calculated for each identified particle using simulations in combination with the normal analysis programs. The normal analysis is described in chapter 3, and figure 4.1 shows a sketch of the applied programs. The programs used for weight calculation are shown in figure 4.2, and described in this chapter.

The particle species, the rapidity and the transverse momentum are given as input to the chain of programs. By using the GEANT package [86], a number of particles

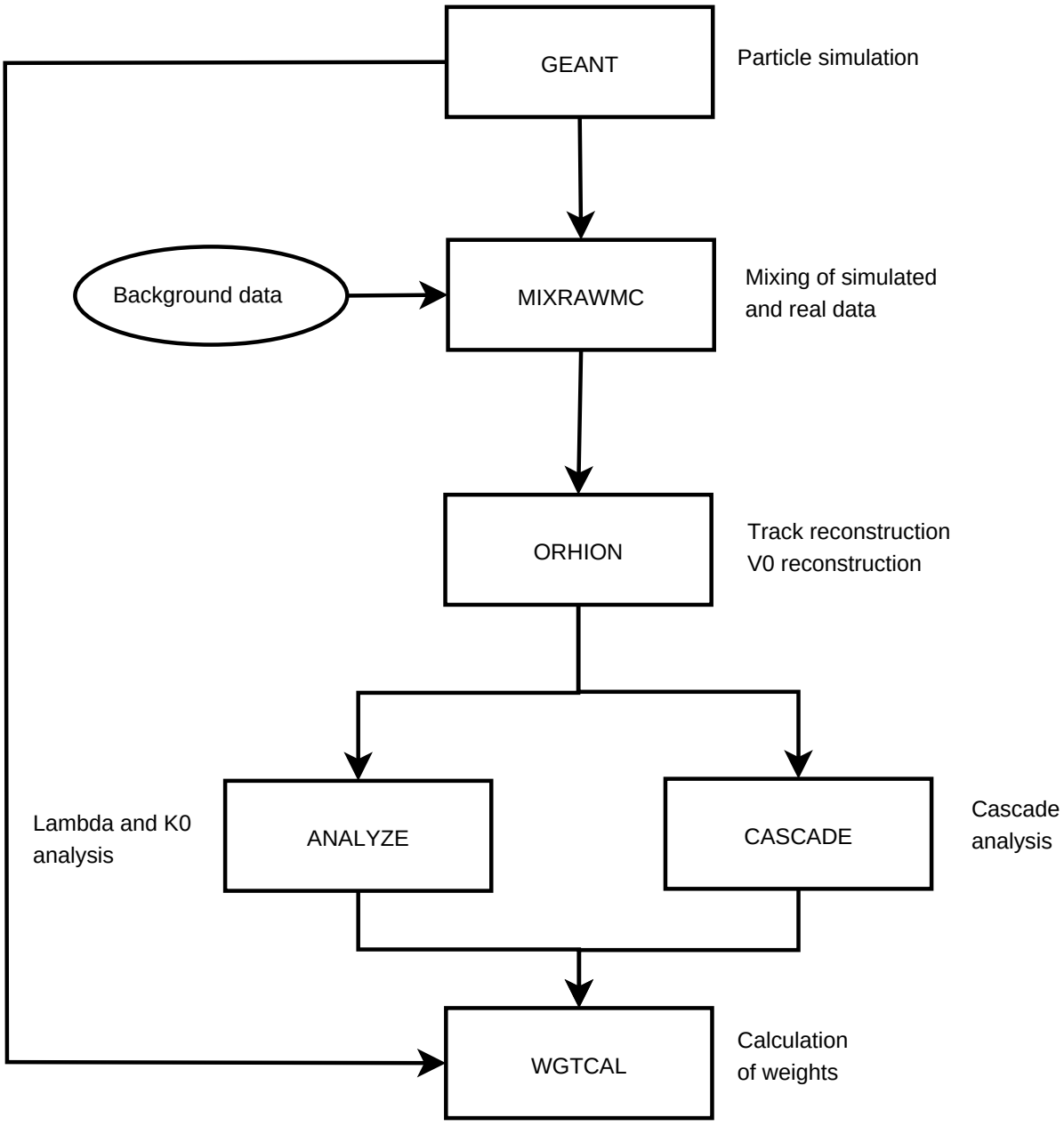

Figure 4.2: Sketch showing weight analysis programs used by WA97/NA57.

with the given rapidity and transverse momentum are simulated and traced through the detector volumes. At this stage the detector inefficiencies are also taken into account. In the MIXRAWMC program the simulated tracks are embedded in normal events with a similar multiplicity to the event where the actual particle was found. The mixed events look like any other event, and are analysed by the analysis programs used in the normal analysis. The simulated particles are found if they pass all the criteria described in chapter 3. A weight is calculated from the ratio of the number of particles simulated by GEANT, to the number of simulated particles that are found by the analysis programs.

4.2 Detector inefficiency and noise subtraction

The silicon pixel detectors started out being ∼100% efficient. After being used in several data taking periods, some of the pixels are damaged from radiation. Some pixels are dead or noisy. The overall efficiency is reduced to 80-90%. The efficiencies are calculated as an average number for each readout chip (see section 2.1.4). The pixel efficiencies are calculated for each calibration period and stored in the experimental database.

The effect of a noisy pixel is the same as a dead pixel. A 'hit' in a noisy pixel should not be used during the track finding. Information about noisy pixels is therefore stored in noise tables. These tables are calculated each day during the run and are used to subtract some of the noise from the data during analysis. Some parts of the pixel detectors are especially noisy. If more than two columns are noisy, the whole chip is marked as noisy in order to reduce the size of the tables. Some readout chips are not working correctly, producing dead areas on the detector surface. Entire chips flagged as noisy effectively increase the number of dead chips in the analysis.

4.3 Simulation using GEANT

Monte Carlo (MC) simulations play an essential role in the calculation of correction factors. A particle may be simulated given the particle type and momentum at the primary vertex. The particle is traced through the different detector volumes, and knowledge of the lifetime of the particle, decay modes and branching ratios makes it possible to simulate the particle decay by using random numbers. The decay vertex is then known and the secondary particles are assigned momenta, again using random numbers. In the same way as the original particle, the secondary particles are traced through the detector volumes and might also decay according to their lifetimes. The MC simulation gives information about the position of the particle at any time, and how the particle passes through the detectors, and this is transformed into the kind of information that we normally get from a detector, e.g. pixel number in a plane in the silicon telescope in NA57, described in section 2.1.4.

In GEANT, the general parameters, like lifetimes, decay modes and branching ratios, are included in the general program. Experiment specific parameters, like for instance the size, geometry and building material of the detectors, have to be given specifically for the experiment. Also the detector efficiencies for the experiment enters as input to GEANT. In the WA97 and NA57 experiments, when a simulated particle passes through the pixel

detectors, the program checks the detector efficiency for each particular detector that is hit to find the probability that the particle is registered by the detector. The program also estimates the energy loss for the particle in the detector, independent of whether a hit is stored or not. In this way the particle is traced through all detectors on its way through the experiment, and hit information is stored for later analysis.

For each 'real' particle that is identified by the analysis programs in the experiment, a number of particles of the same type and with the same rapidity and transverse momentum are simulated. The number of simulated particles is compared to the number of particles identified by the analysis programs. GEANT tracking of particles through the experimental setup is a very time consuming task. To save CPU time, the simulation study is limited to particles that actually pass trough the experimental setup. Other particles are counted as simulated particles that can not be detected in the experiment, but they are not traced. A particle that pass through the experimental setup has to be emitted from the primary vertex with a certain angle. By limiting this emission angle, less time is spent on tracking particles that never hit the main detectors.

A lot of CPU time can also be saved by simulating only the decay channels measured by the experiment, i.e. only decays into charged particles as described in the beginning of chapter 3. There is e.g. no point in spending time on simulating a Λ decaying into neutron and a π^0 (BR = 35.8%) since neutral particles are not detected in the experiment. This is easily corrected for in the final weight calculation by dividing the weight with the branching ratio for the selected decay channel.

Cuts that are similar to those used in the analysis chain (chapter 3) can also be introduced in GEANT. However, they must be checked carefully to make sure that the particles that are not stored for further analysis can under no circumstance be found by the analysis programs. In the analysis all tracks are required to pass through the first and the last plane in the compact part of the telescope. In the simulation it is therefore required that the track has to pass through a certain number of pixel planes. For instance, if the particle only passes through the first two planes, this particle can not be reconstructed by the analysis programs, so the information about the particle is not stored for further analysis, only counted as simulated.

In NA57, the primary vertex position is also simulated by GEANT. The experimentally observed run-by-run vertex positions, y_{run} and z_{run} (see section 3.2), are given as input together with the observed gaussian spread of this position, $\sigma_{y_{run}}$ and $\sigma_{z_{run}}$. The primary vertex position is simulated according to these values so that the simulated events have the same distribution as the real events. This method was not used by the WA97 experiment. More details are given in section 5.5. Figure 4.3 shows a simulated particle from GEANT analysed by the ORHION program. Only the compact part of the silicon telescope is shown.

The correction factors are calculated requiring 2500-5000 particles from GEANT stored for further analysis.

4.4 Mixing with real data

The particles simulated by GEANT are added to a real event with tracks and noise, making the conditions the same as for real particles. The real events are here referred

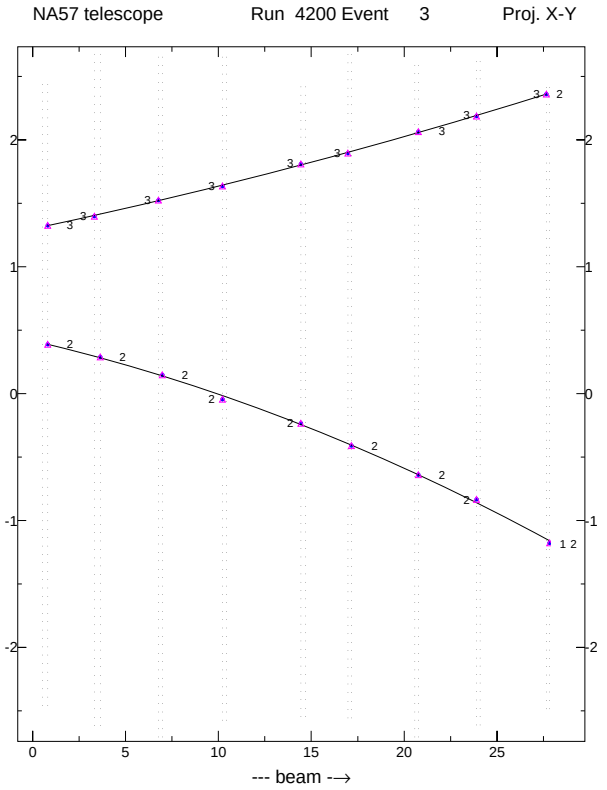

Figure 4.3: Simulated Λ in NA57.

to as background events. Background events are selected from the whole running period where the real particle was found. A running period is here defined as a continuous period where the running conditions are similar. The magnetic field is always the same in a running period, and the variation of the detector efficiencies is small. The selection of background events is done in a periodic manner, i.e. every 200th event.

Further more, when selecting background events for mixing with a simulated particle, events with a similar hit multiplicity in the telescope as the event where the real particle was found, are chosen. It is more difficult to find a particle in a high multiplicity event than in a low multiplicity event, and this should be reflected by the weights. The weight is therefore slightly higher for a particle found in a high multiplicity event than for a particle found in a low multiplicity event. This effect is much smaller for WA97 and NA57 where there is three dimensional hit information, than for WA85 and WA94 where wire chambers and silicon microstrips gave only two dimensional hit information.

To add a simulated particle into a background event, the GEANT information about the particle is converted into the same format as used in a raw data file. For instance, GEANT gives information of which pixels that are hit by the particle by giving a pixel number (in y and z direction), ladder number and chip number. Basically, the same information is given in a raw data file, but the format is completely different. In WA97, which uses the EPIO (Experimental Physics Input Output Package) format [87], a pixel hit is stored in four 16 bit words. In the NA57 experiment, the EPIO format was exchanged with the newer DATE format [81] which is developed for the ALICE experiment. DATE

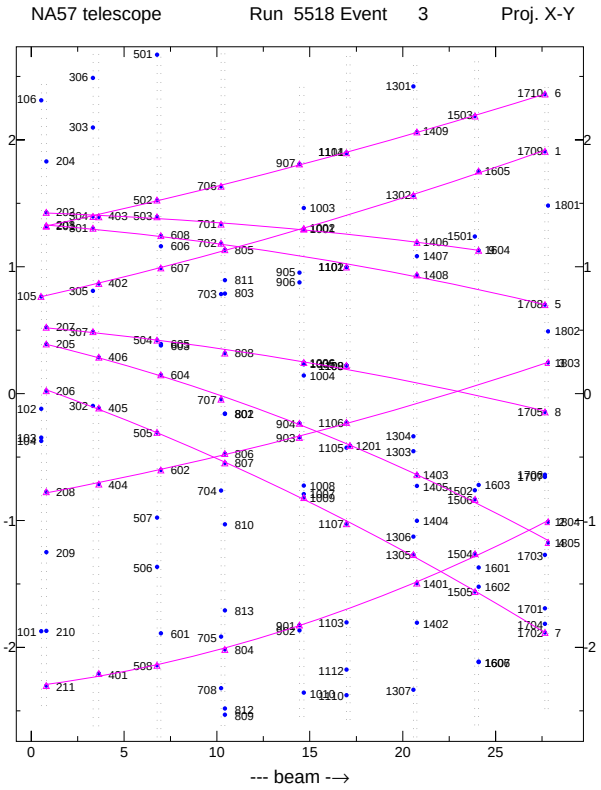

Figure 4.4: A simulated Λ in NA57 added to a background event.

uses 32 bit words, and a single pixel hit is stored in two words. In both the EPIO and the DATE formats, the pixel hits are stored ordered by planes, since information about the plane number the hit belongs to is not given in the two/four words representing a hit. Therefore, the simulated hits have to be added to the raw data file in the correct place. The vertex position with its spread used when simulating the event in GEANT, is stored in the mixed event and used during the later analysis.

Figure 4.4 shows an event display with the simulated particle from figure 4.3 mixed into a background event from NA57. The background event without the implanted particle is shown in figure 3.2.

4.5 Analysis

The further analysis of the mixed events is almost identical to the analysis of the real data. This is already described in detail in chapter 3. The charged particle multiplicity of the mixed event is not found at this stage, since this is already known from the original analysis. As the primary vertex, the position used by GEANT is taken from the mixed event, and is not recalculated using tracks from the background event. ORHION is used for track finding and selection of V^0 candidates, and ANALYZE/CASCADE is used for selecting the particles under study. The different programs are shown in figure 4.2. The output from this is a Data Summary Tape (DST) where information about the identified particles is given, e.g. rapidity and particle momentum.

4.6 Calculation of weights

A weight for each 'real' particle is calculated. The weight, W, is defined as

$$W = \frac{360^\circ}{\Delta\phi} \cdot \frac{N_{gen}}{N_{found}} \cdot \frac{1}{BR} \tag{4.1}$$

where $\Delta\phi$ is the interval for the azimuthal angle where particles are generated, N_{gen} is the number of generated (simulated) particles, N_{found} is the number of particles found by the analysis program, and BR is the branching ratio for the decay channel that was used during the simulation. In this way, the particles that were not simulated by GEANT since they could not be found by the analysis programs, are accounted for. A fraction P is defined as

$$P = \frac{N_{found}}{N_{gen}} \tag{4.2}$$

The error on the weight is then calculated as

$$e_W = W \cdot \frac{e_P}{P} = \frac{W}{P}\sqrt{\frac{P(1-P)}{N_{gen}}} \tag{4.3}$$

Mean weights for particles from Pb-Pb collisions with a beam momentum of 158 GeV/c are given in table 4.1.

Particle	Mean weight $< W >$
K^0_S	986 ± 52
Λ	1517 ± 38
$\overline{\Lambda}$	1552 ± 36
Ξ^-	26090 ± 719
$\overline{\Xi}^+$	25590 ± 1365
Ω^-	20740 ± 1360
$\overline{\Omega}^+$	19245 ± 1770

Table 4.1: Mean weights for particles from Pb-Pb collisions at 158 GeV/c.

4.7 Comparison between Monte Carlo and real data in NA57

A number of checks have been performed to make sure that the simulations used for calculating the correction factors in NA57 give the same distributions as the real data. If the simulations are not reproducing the distributions from the real data, it indicates that the cuts in the analysis have a different effect on the simulated data compared to the real data. The consequence might be that too many or too few simulated particles are found by the analysis programs. As a result, the calculated weights are underestimated or overestimated, which affects the final yields (see chapter 5).

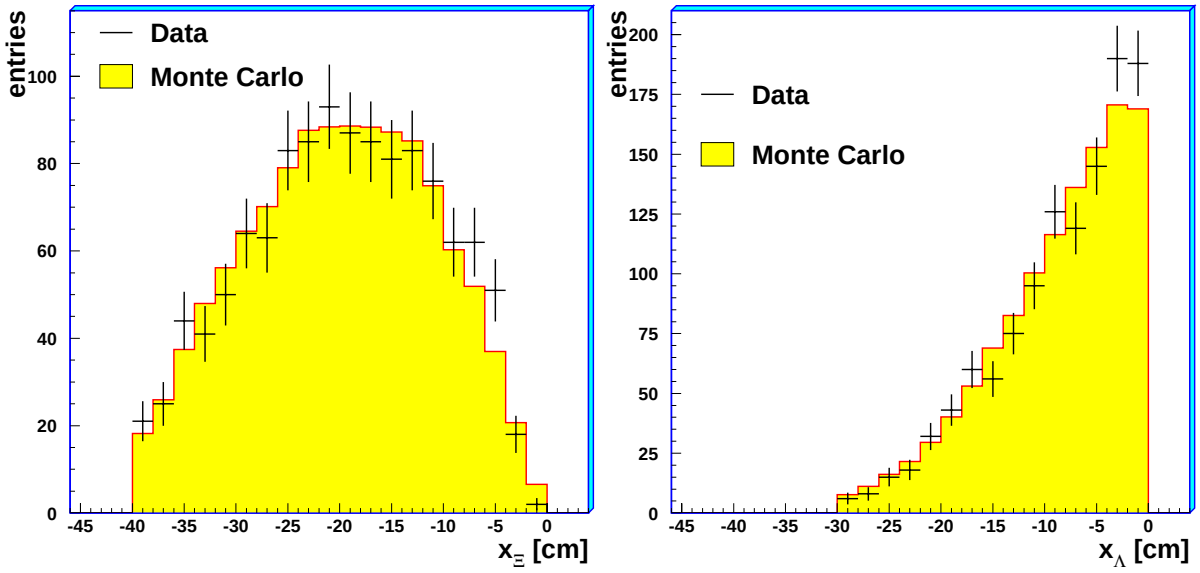

Figure 4.5: Comparison between real data and Monte Carlo simulations for (left) the decay length of the Ξ, and (right) the decay length of the Λ coming from the Ξ decay.

Some comparisons between simulations and real data for Ξ measurements are presented here:

- The decay length of the Ξ (see figure 4.5 (left))
- The decay length of the Λ from a Ξ decay (see figure 4.5 (right))
- The π impact parameter with respect to the primary vertex (see figure 4.6 (left))
- The Λ impact parameter with respect to the decay vertex of the Ξ (see figure 4.6 (right))
- The internal decay angles in the Ξ reference system: $cos(\theta^*)$, where θ^* is the angle between the Λ and the Ξ lines of flight in the Ξ reference system, and ϕ is the azimuthal angle (see figure 4.7)
- The closest distance in space between the extrapolated π and proton tracks coming from the Λ decay (see figure 4.8)

As seen in the figures, all tests show agreement between simulated and real data. Some similar plots for K^0_S, Λ and Ω are presented in [16].

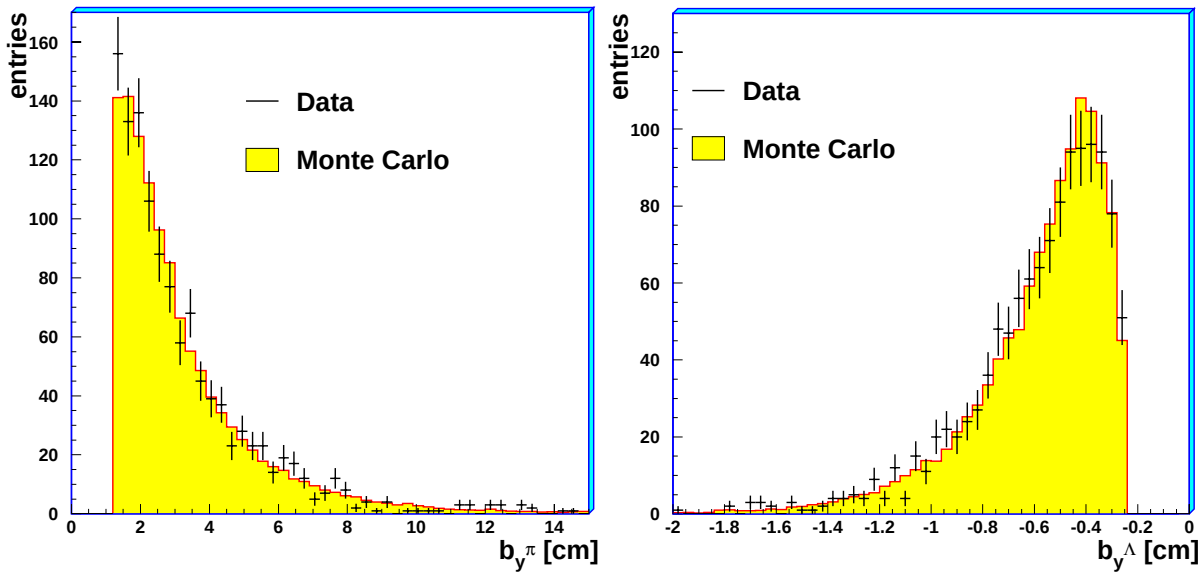

Figure 4.6: Comparison between real data and Monte Carlo simulations for (left) the π impact parameter with respect to the primary vertex and (right) the Λ impact parameter with respect to the decay vertex of the Ξ.

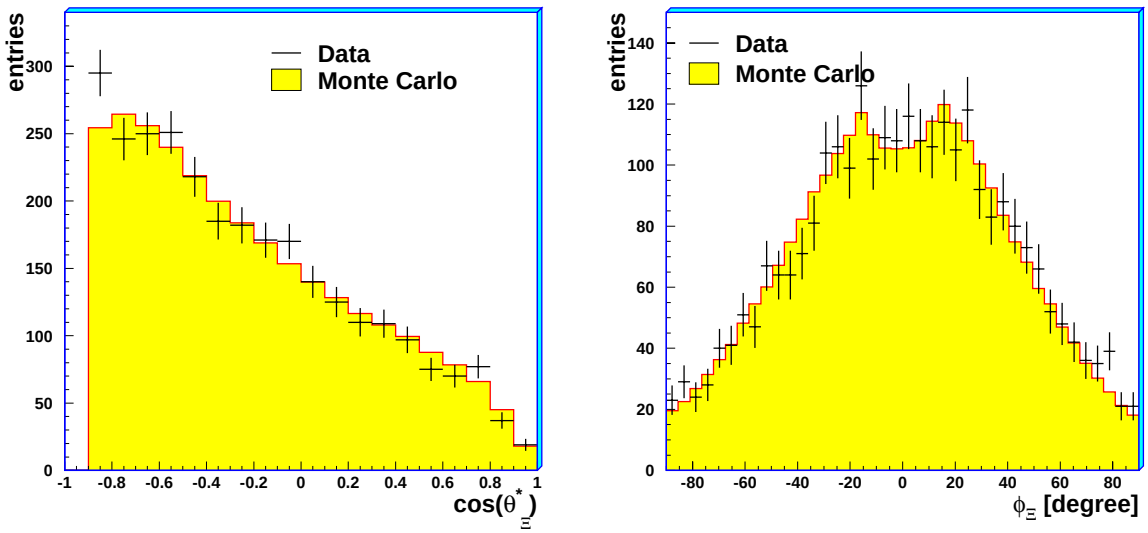

Figure 4.7: Comparison between real data and Monte Carlo simulations for the internal decay angles in the Ξ reference system, $cos(\theta^*)$ (left) and ϕ (right).

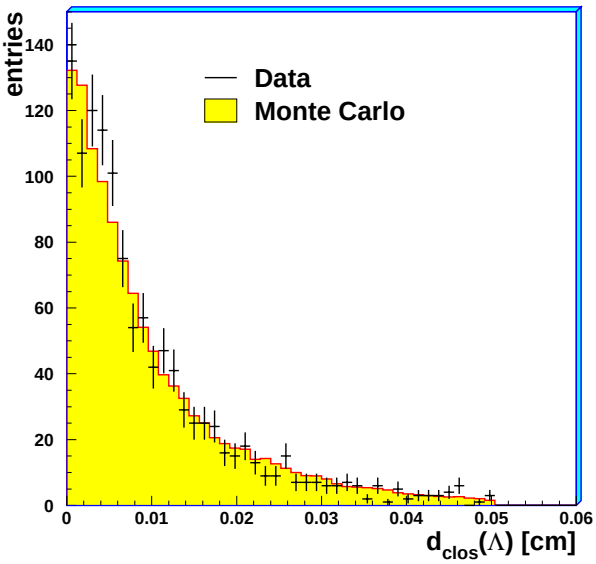

Figure 4.8: Comparison between real data and Monte Carlo simulations for the closest distance in space between the extrapolated π and proton tracks coming from the Λ decay

Chapter 5

Analysis and results

5.1 Acceptance regions

After all the events have been weighted, a window of good geometrical acceptance in p_{T} and rapidity is selected. Figure 5.1 shows the selected regions for K^0s, Λs, Ξs and Ωs from Pb-Pb collisions at 158 A GeV/c collected in 1998. The shape of the acceptance regions are related to the area of the telescope and its inclination angle with respect to the beam line. The edges of the acceptance window correspond to the edges of the telescope. In the weighting procedure, particles generated close to the edges of the telescope due to smearing effects sometimes hit inside the telescope and sometimes outside. The weights for these particles are therefore higher than for particles hitting well inside the telescope. In order to select a good acceptance window, a region is selected such that the highest weights are excluded from the acceptance area. Normally, weights up to about ten times the size of the smallest weight are accepted inside the final acceptance window[1]. The region is selected by choosing a minimum and a maximum p_{T}, and a minimum value of the rapidity. The left and right curves in the acceptance window are related to the angle of inclination of the telescope. The acceptance windows are the same for particles and antiparticles.

A study of the sensitivity to the selection of the acceptance window is performed. As an example, the result for the Ξ acceptance region is shown in figure 5.2. The left figure shows the different acceptance windows being studied for Ξ^- and $\overline{\Xi}^+$. In the right figure the particle production yields per event for Ξ^- and $\overline{\Xi}^+$ are plotted as a function of the selected acceptance windows. (The calculation of particle yields is described in section 5.4.) The number 0 corresponds to the acceptance window drawn with a thick line. Negative numbers corresponds to the smaller acceptance windows, while positive numbers corresponds to the larger windows. As seen in the figure, the final yields are stable with respect to the selection of acceptance window.

[1]For particles with a small statistical sample, the acceptance regions are defined by a Monte Carlo study.

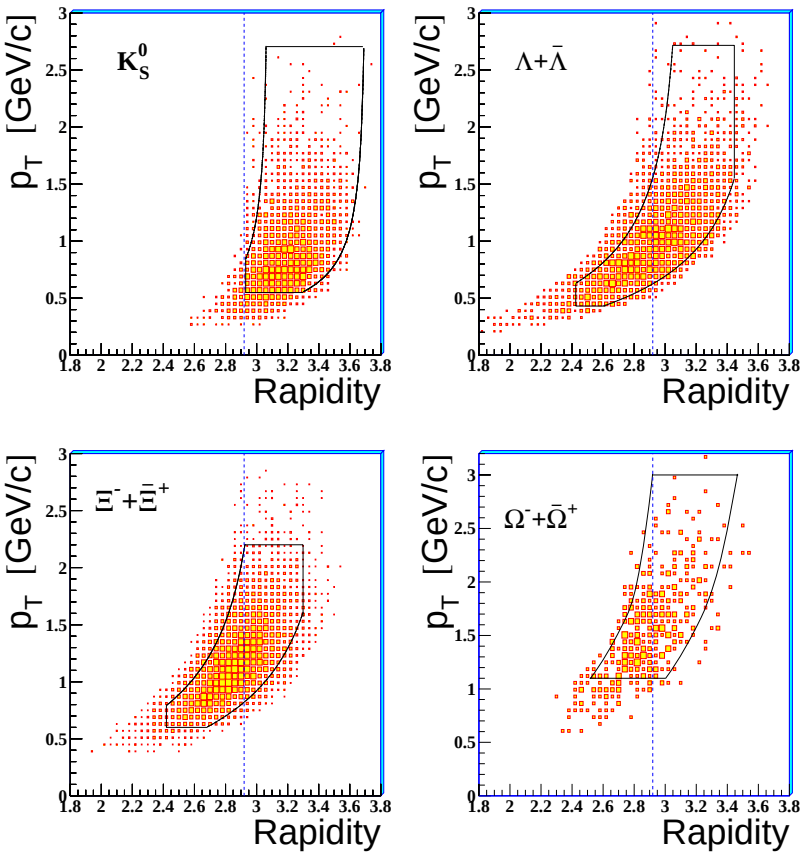

Figure 5.1: Acceptance regions for Pb-Pb collisions at 158 A GeV/c.

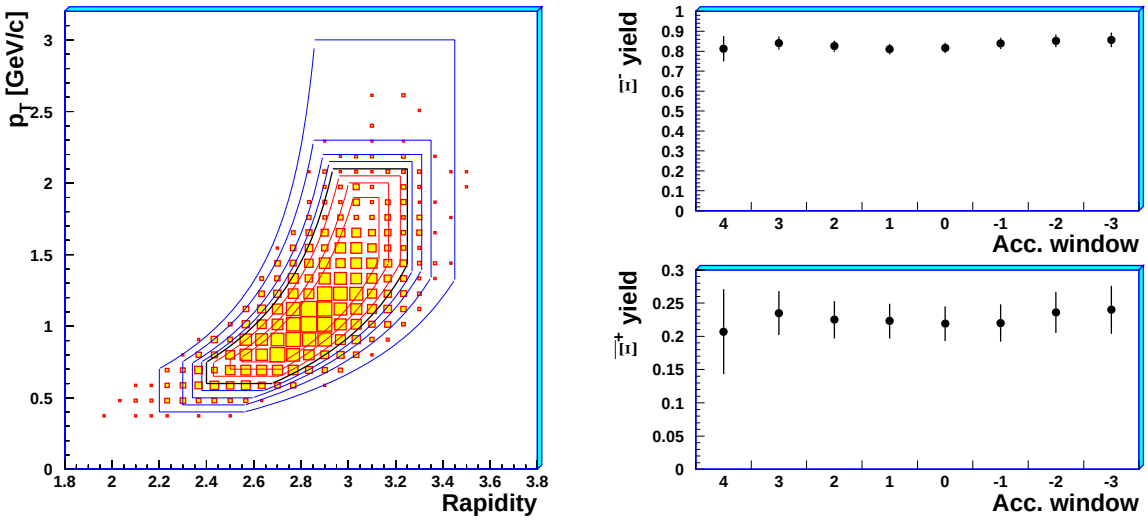

Figure 5.2: Stability of the Ξ^- and $\overline{\Xi}^+$ yields (right) for different acceptance windows (left).

5.2 Centrality

The centrality of a collision can not be measured directly, but can be estimated e.g. from measured transverse energy or the multiplicity of charged particles. WA97 and NA57 measure the charged particle multiplicity. The centrality of a collision can be estimated by the number of participants. The number of participants increases with the centrality of the collision. The number of participants is here defined as the number of wounded nucleons (N_{wound}), i.e. the nucleons which take part in the initial collisions, calculated from the Glauber model [88]. The Glauber model is a simple geometrical model describing the collision between two nuclei. In this model the projectile nucleons traverse the target nucleus in a straight line and collide with several nucleons in the target. The nucleons inside a nucleus are assumed to be independent, and the nucleus-nucleus collisions are regarded as a superposition of independent sequential nucleon-nucleon interactions. Cross sections are interpreted as geometric areas, and when two nucleons overlap they are assumed to interact.

In both the WA97 and NA57 experiments, the charged particle multiplicity is measured using two planes of silicon microstrip detectors (MSD, see section 2.1.3). The two planes together cover the pseudorapidity region $2 < \eta < 4$. In the setup at 40 A GeV/c there is an overlap between the pseudorapidity coverage of the two planes, corresponding to the region $2.4 < \eta < 3$. In this region the multiplicity is determined from an average of the multiplicities measured in the two planes. By analysing the data from these detectors (see [89] for details), the distribution of the total hit multiplicity in the two planes is found. The contribution of interactions in the air or other material along the beam line, the *empty target contamination*, is evaluated using events collected with no target in the experiment. This contamination is subtracted from the final MSD data. The empty target contamination corresponds to about 17% for WA97 and about 6% for the NA57 experiment.

In order to obtain the final charged particle multiplicity, the hit multiplicity in the MSD is corrected for delta-rays and background hits, geometrical acceptance, detector response (efficiencies, double hits, charge sharing between contiguous strips), secondary interactions and gamma ray conversions. This is done using the VENUS model [90] and the GEANT package. The charged particle distribution for NA57 measured at 158 A GeV/c is shown in figure 5.3. The drop at low multiplicities is the effect of the scintillator petals centrality trigger suppressing low multiplicity events. The NA57 multiplicity distribution is divided into five classes (0, 1, 2, 3 and 4), 4 being the most central class. The WA97 experiment had a stricter centrality trigger and measured only the four most central classes (1 to 4). The most peripheral class (0) is therefore accessible only to NA57.

The number of wounded nucleons (N_{wound}) is calculated assuming that the mean number of charged particles is proportional to N_{wound}^{α}. In WA97 $\alpha = 1$ was used, which means that the average charged particle multiplicity is proportional to the number of wounded nucleons. The measured multiplicity spectrum in NA57, is compatible with values of α between 1.02 and 1.09. Varying α within this range has a minor effect on the WA97 data, at most 7%. No significant change in the centrality dependence of the hyperons is observed.

In NA57 another method for determining the number of wounded nucleons was chosen. This method is based on the measured trigger cross section, and is much less dependent

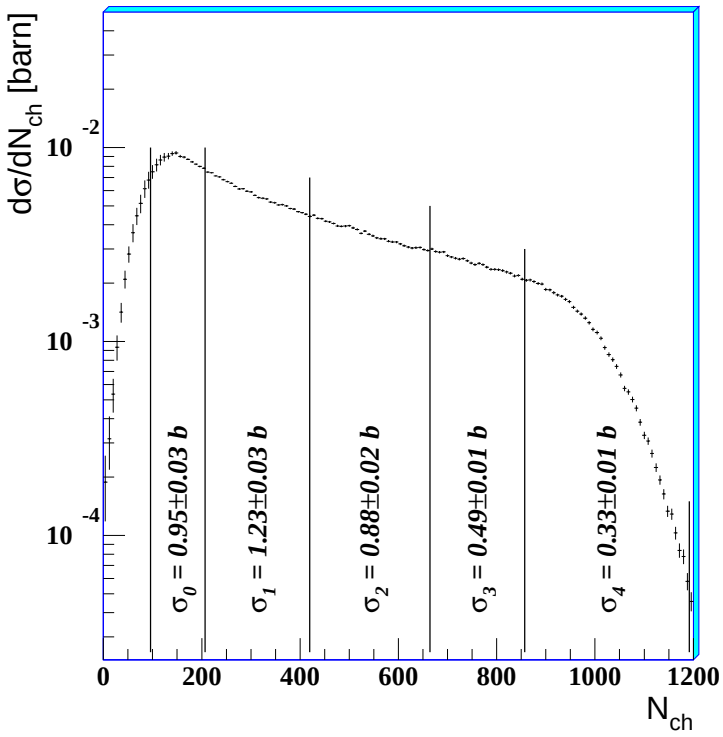

Figure 5.3: Multiplicity distribution for charged particles and centrality classes for Pb-Pb collisions at 158 A GeV/c.

on the relation between the number of wounded nucleons and the number of charged particles. The centrality classes for the model has been chosen in such a way that they represent the same absolute cross section as the data. The fraction of the total inelastic cross section for the five centrality classes, and the average number of wounded nucleons for each class, are given in table 5.1.

Class	0	1	2	3	4
σ/σ_{inel} (%)	40-53	23-40	11-23	4.5-11	0-4.5
$\langle N_{wound} \rangle$	62 ± 4	121 ± 4	209 ± 3	290 ± 2	349 ± 1

Table 5.1: Inelastic cross section and number of wounded nucleons for the five centrality classes.

5.3 Transverse mass distributions

The double-differential (y, m_{T}) distributions for each type of particle has been fitted to an exponential function using the maximum likelihood method. The distributions are parametrized using the expression

$$\frac{1}{m_{\mathrm{T}}} \frac{\mathrm{d}^2 N}{\mathrm{d}m_{\mathrm{T}} \mathrm{d}y} = f(y) \exp(-\frac{m_{\mathrm{T}}}{T}) \tag{5.1}$$

where m_{T} is the transverse mass defined in equation 1.4. The rapidity distribution is assumed to be flat ($f(y) = const.$) within the experimental acceptance region. The inverse slope parameter, T, is left as a free parameter and is extracted by fitting the equation to the experimental data. Figure 5.4 shows experimental transverse mass spectra for K^0_S, Λ, Ξ and Ω particles measured by NA57. The lines show the inverse slope parameter T obtained by the maximum likelihood fits. For Ω^- and $\overline{\Omega}^+$, the open points are not used in the fit. The best fit values are given in table 5.2. The fit is done for the whole centrality range of NA57, i.e. the 53% most central collisions. For each particle species, the inverse slope parameter is found to be in good agreement with that of the antiparticle.

The same fits are done for data from WA97 on about the 40% most central collisions [91]. The values are in agreement with the values found by NA57.

5.4 Particle yields

For each particle species and for each centrality class, the particle production yield per event, Y, is calculated. The particle production yield is defined by the integral

$$Y = \int_{m}^{\infty} \mathrm{d}m_{\mathrm{T}} \int_{y_{cm}-0.5}^{y_{cm}+0.5} \frac{\mathrm{d}^2 N}{\mathrm{d}m_{\mathrm{T}} \mathrm{d}y} \mathrm{d}y \tag{5.2}$$

where y_{cm} is the mid-rapidity. For the 158 A GeV/c data the mid-rapidity is at $y_{cm} = 2.92$. The particle production yields per event are extrapolated to a common phase space

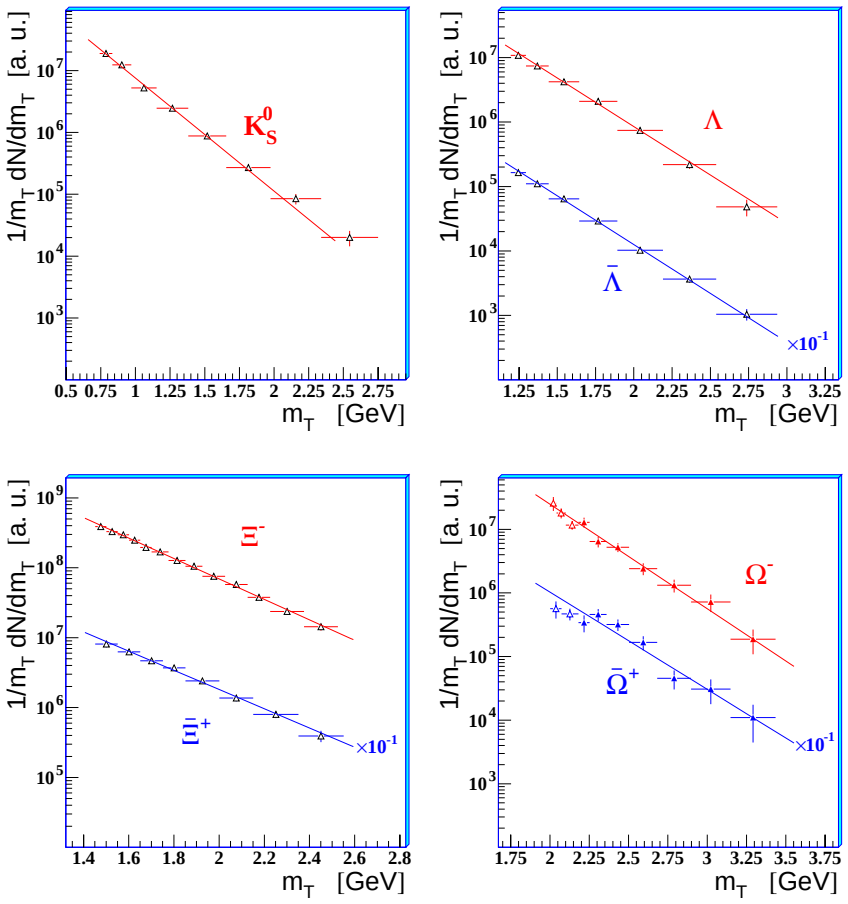

Figure 5.4: Transverse mass distributions measured at 158 A GeV/c. The exponential functions have inverse slopes obtained by the maximum likelihood fits. The open points in the Ω^- and $\overline{\Omega}^+$ spectra are not used in the fit.

Particle	T (MeV)
K^0_S	$237 \pm 4 \pm 24$
Λ	$289 \pm 7 \pm 29$
$\overline{\Lambda}$	$287 \pm 6 \pm 29$
Ξ^-	$297 \pm 5 \pm 30$
$\overline{\Xi}^+$	$316 \pm 11 \pm 30$
Ω^-	$264 \pm 19 \pm 27$
$\overline{\Omega}^+$	$284 \pm 28 \pm 27$

Table 5.2: Inverse slope parameters, T, of strange particles measured in Pb-Pb collisions. Statistical (first) and systematic (second) errors.

	Yield (Y)	Extrapolation factor (S)
K^0_S	9.0 ± 0.6	3.4
Λ	7.8 ± 0.2	2.6
$\overline{\Lambda}$	1.17 ± 0.03	2.6
Ξ^-	0.819 ± 0.026	3.4
$\overline{\Xi}^+$	0.220 ± 0.014	3.4
Ω^-	0.118 ± 0.011	7.1
$\overline{\Omega}^+$	0.054 ± 0.007	7.1

Table 5.3: Total yields and extrapolation factors for the 1998 Pb-Pb data sample at 158 A GeV/c.

window using equation 5.1, assuming that the fitted value of the inverse slope parameter T is not changing inside this window. The common window covers one unit of rapidity around the central value and the full m_{T} range.

The total particle production yield for a particle species in the extrapolated phase space window can be written as the yield in the acceptance window for the experiment, Y_{Acc}, times an extrapolation factor S,

$$Y = Y_{Acc} \cdot S. \tag{5.3}$$

The extrapolation factor can be defined as

$$S = \frac{I_{Tot}}{I_{Acc}} \tag{5.4}$$

where $I_{Tot} = Y$ is the total integral (from equation 5.2) over the full extrapolated phase space and I_{Acc} is the corresponding integral in the acceptance window of the experiment. The error on the total yield can then be found by

$$e_Y = \sqrt{(S \cdot e_{Y_{Acc}})^2 + (e_S \cdot Y_{Acc})^2} \tag{5.5}$$

where $e_{Y_{Acc}}$ is the error on Y_{Acc}, and e_S is the error on S. The error on the yield in the acceptance window is calculated by

$$e_{Y_{Acc}} = \frac{\sqrt{\sum_i (W_i^2 + e_{W_i}^2)}}{N_{ev}} \tag{5.6}$$

The weight, W, and the error on the weight, e_W, are discussed in section 4.6. N_{ev} is the total number of analysed events corrected for empty target contamination. The error on the extrapolation factor is found by

$$e_S = \frac{\mathrm{d}S}{\mathrm{d}T} \cdot e_T \tag{5.7}$$

where e_T is the error on the fitted value of the inverse slope parameter T. Total yields and extrapolation factors for the 158 A GeV/c Pb-Pb data sample collected in 1998 are listed in table 5.3.

Particle production yields for the hyperons from the analysis of NA57 data collected at a beam momentum of 158 A GeV/c are listed in table 5.4. To find the strangeness enhancement, the particle yields found in Pb-Pb collisions are compared to the yields found in p-Be and p-Pb collisions where creation of a quark gluon plasma is not expected. However, such collisions have not been studied by NA57 at this energy. The NA57 Pb-Pb yields are therefore compared to the p-Be and p-Pb yields from WA97 [92], here listed in table 5.5. All errors presented here are statistical only.

System $\rightarrow$	**Pb-Pb**				
$< \mathbf{N_{wound}} > \rightarrow$	**62** (0)	**121** (1)	**209** (2)	**290** (3)	**349** (4)
K^0_S	2.96 ± 0.54	7.17 ± 0.85	15.2 ± 2.4	19.6 ± 2.4	25.3 ± 3.5
Λ	2.30 ± 0.22	5.19 ± 0.29	9.5 ± 0.5	15.0 ± 0.8	18.5 ± 1.1
$\overline{\Lambda}$	0.417 ± 0.035	0.82 ± 0.04	1.60 ± 0.07	1.84 ± 0.10	2.47 ± 0.14
Ξ^-	0.181 ± 0.013	0.52 ± 0.02	1.07 ± 0.04	1.80 ± 0.07	2.08 ± 0.09
$\overline{\Xi}^+$	0.045 ± 0.007	0.14 ± 0.01	0.29 ± 0.02	0.37 ± 0.03	0.51 ± 0.04
$\Omega^- + \overline{\Omega}^+$	0.037 ± 0.017	0.095 ± 0.017	0.23 ± 0.03	0.33 ± 0.05	0.47 ± 0.07

Table 5.4: Particle productions yields per event for hyperons in Pb-Pb collisions at 158 A GeV/c from NA57. The centrality classes are included in parenthesis.

System $\rightarrow$	**p-Be**	**p-Pb**
$< \mathbf{N_{wound}} > \rightarrow$	**2.5**	**4.75**
Λ	0.0344 ± 0.0005	0.060 ± 0.02
$\overline{\Lambda}$	0.0111 ± 0.0002	0.015 ± 0.001
Ξ^-	0.0015 ± 0.0001	0.0030 ± 0.002
$\overline{\Xi}^+$	0.00068 ± 0.0001	0.0012 ± 0.0001
$\Omega^- + \overline{\Omega}^+$	0.00016 ± 0.00006	0.000263 ± 0.000078

Table 5.5: Particle productions yields per event for hyperons in p-Be and p-Pb collisions at 158 A GeV/c from WA97.

Figure 5.5 shows the hyperon enhancement factors, E, as a function of the number of wounded nucleons, $< N_{wound} >$. Enhancement is defined as

$$E = \left(\frac{Y}{< N_{wound} >} \right)_{Pb-Pb} / \left(\frac{Y}{< N_{wound} >} \right)_{p-Be} \tag{5.8}$$

for Pb-Pb collisions. Enhancement factors for p-Pb collisions are normalized to p-Be collisions in the same way as for Pb-Pb collisions. The enhancement factors are presented in two separate figures. The left figure shows the enhancement for Λ and Ξ^-, particles that have at least one valence quark in common with the colliding nucleons. In the figure to the right, the enhancement factors for $\overline{\Lambda}$, $\overline{\Xi}^+$ and $(\Omega^- + \overline{\Omega}^+)$ are shown. These particles have no quarks in common with the incoming nucleon, i.e. all quarks have to be created

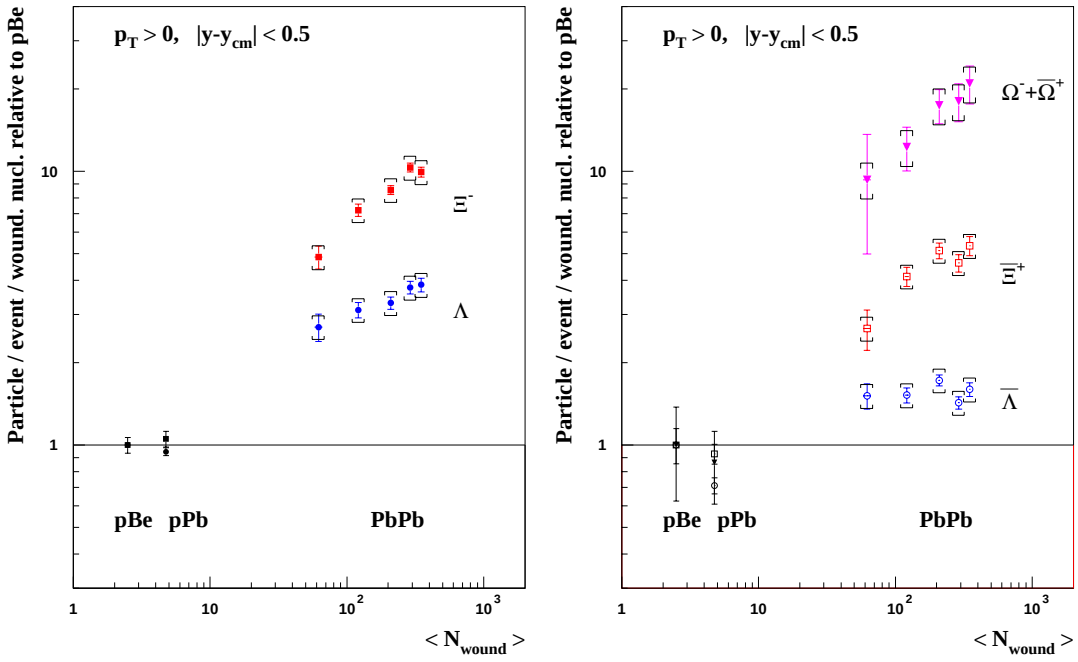

Figure 5.5: Yields per wounded nucleon relative to the p-Be yields as a function of the number of wounded nucleons, for Λ and Ξ^- (left) and for $\overline{\Lambda}$, $\overline{\Xi}^+$ and $\Omega^- + \overline{\Omega}^+$ (right) measured by NA57 at 158 A GeV/c.

in the collision. The horizontal line represents the predicted centrality dependence if the yields were to increase proportionally to the number of wounded nucleons all the way from p-Be to central Pb-Pb collisions. The deviation from this line shows the enhancement. The Ω^- and the $\overline{\Omega}^+$ are combined in one enhancement factor due to the low statistical sample from the data using a proton beam. The figure shows that all strange particle yields are enhanced in Pb-Pb collisions compared to p-Be and p-Pb collisions, and that the enhancement grows with the strangeness content of the particle, up to a factor of about 20 for the $(\Omega^- + \overline{\Omega}^+)$ at the most central collisions. While the enhancement may have saturated for the $\overline{\Lambda}$, the other particles show no such saturation.

5.5 Differences between WA97 and NA57 results

The NA57 yields presented in the previous section are found to be 20-30% larger than the WA97 yields. There is no obvious reason why the results should be different for the two experiments. A number of tests of the analysis programs used by WA97 and NA57 have been performed. The methods used in the analysis and in the correction procedure, the stability of our analysis and the software have all been tested. All tests referred to here are for Ξ^- and $\overline{\Xi}^+$, but similar tests have also been performed for the other particle species.

The knowledge of the position of the interaction vertex is used for various kinematic cuts in the analysis. There is a difference in the methods used by the two experiments

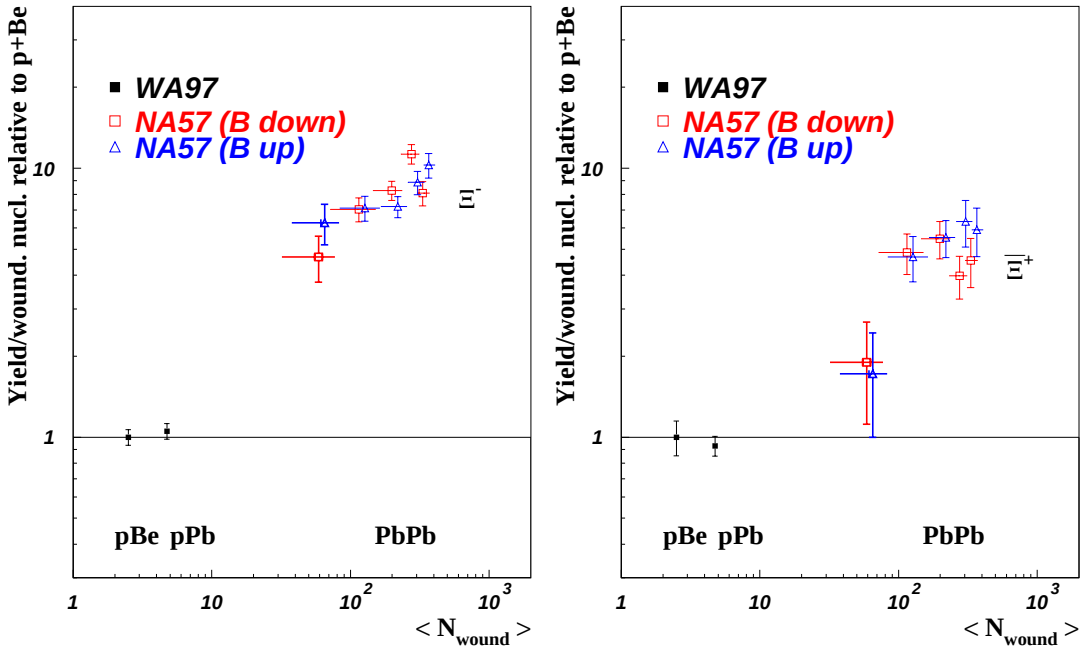

Figure 5.6: NA57 Ξ^- and $\overline{\Xi}^+$ yields per wounded nucleon relative to the p-Be yields measured by WA97. Events with different magnetic field polarities are separated. The points are slightly shifted with respect to each other.

for determining this position. As described in section 3.2, the primary vertex position in WA97 is determined event by event by extrapolating the reconstructed tracks to the target plane. The primary vertex position used in NA57, is instead an average vertex position for each run, calculated using only the high multiplicity events. Both the average vertex position and the spread of the position is found. The two methods should be equivalent if treated correctly in the correction procedure. However, in WA97 the measured event by event primary vertex position, without introducing any spread, was used in the simulation when calculating the correction factors. As a result, the correction factors in WA97 are underestimated, and the Pb-Pb particle yields are systematically shifted down by about 10%. The effect shows no multiplicity dependence. This problem does not affect the p-Be results used in the calculation of enhancement factors for NA57 (158 A GeV/c), since a completely different method was used in the analysis of the WA97 p-Be data, where the position of the beam was reconstructed using a beam telescope [93].

In order to check the stability of our analysis, the NA57 Ξ^- and $\overline{\Xi}^+$ yields were recalculated and corrected for acceptance and efficiency, using different selection criteria. No significant changes in the NA57 results were seen.

The Ξ^- and $\overline{\Xi}^+$ yields have also been studied in different time periods, for different magnetic field polarities (see figure 5.6), and in different acceptance windows (see figure 5.2) without observing any systematic shift in the final results.

To check the program chain used for calculating correction factors, the Ξ^-s and $\overline{\Xi}^+$s identified in WA97 are weighted using the NA57 chain of programs. The result is, within statistical uncertainties, the same as the previous WA97 result. The NA57 Monte Carlo

simulations have also been checked carefully as described in section 4.7. Due to a larger background in the NA57 invariant mass plots than in WA97, a study using event mixing was also performed (see section 3.6) to estimate the background. It is found that the slightly larger background has little influence on the results. In summary, all tests show that the NA57 results are stable.

Overall, the experimental conditions were better in NA57 than in WA97. The beam was more stable and cleaner due to the improved beam line, more pixels were used, and much more tests of the analysis programs were performed. The outcome of all the checks gave confidence in the NA57 results.

5.6 Results from 40 A GeV/c data

Figure 5.7 shows the Λ, $\overline{\Lambda}$, Ξ^-, $\overline{\Xi}^+$, Ω^- and $\overline{\Omega}^+$ signals for the complete sample of Pb-Pb central events at 40 A GeV/c. The total data sample consists of 240M events. The analysis of the data set is presented in reference [94]. Figure 5.8 shows the Λ, $\overline{\Lambda}$ and Ξ^- signals for 2/3 of the data sample from p-Be collisions at 40 A GeV/c, about 110M events. The complete analysis is presented in reference [95].

The 40 A GeV/c Pb-Pb data are separated in the same five centrality classes as the 158 A GeV/c data (see section 5.2). The analysis follows the same procedure as earlier described for the Pb-Pb data at 158 A GeV/c. Figure 5.9 shows the enhancement factors for the 40 A GeV/c data sample. The limited statistics allows only enhancement factors for Λ, $\overline{\Lambda}$ and Ξ^- to be presented. A lower limit to the $\overline{\Xi}^+$ enhancement in the four most central classes at a 95% confidence level is indicated in the figure. A significant enhancement of the production of hyperons when going from p-Be to Pb-Pb collisions is observed also for the 40 A GeV/c data. The enhancement also follows the same hierarchy as in the 158 A GeV/c data sample when looking at the strangeness content of the particle, $E(\Xi^-) > E(\Lambda)$ and $E(\overline{\Xi}^+) > E(\overline{\Lambda})$.

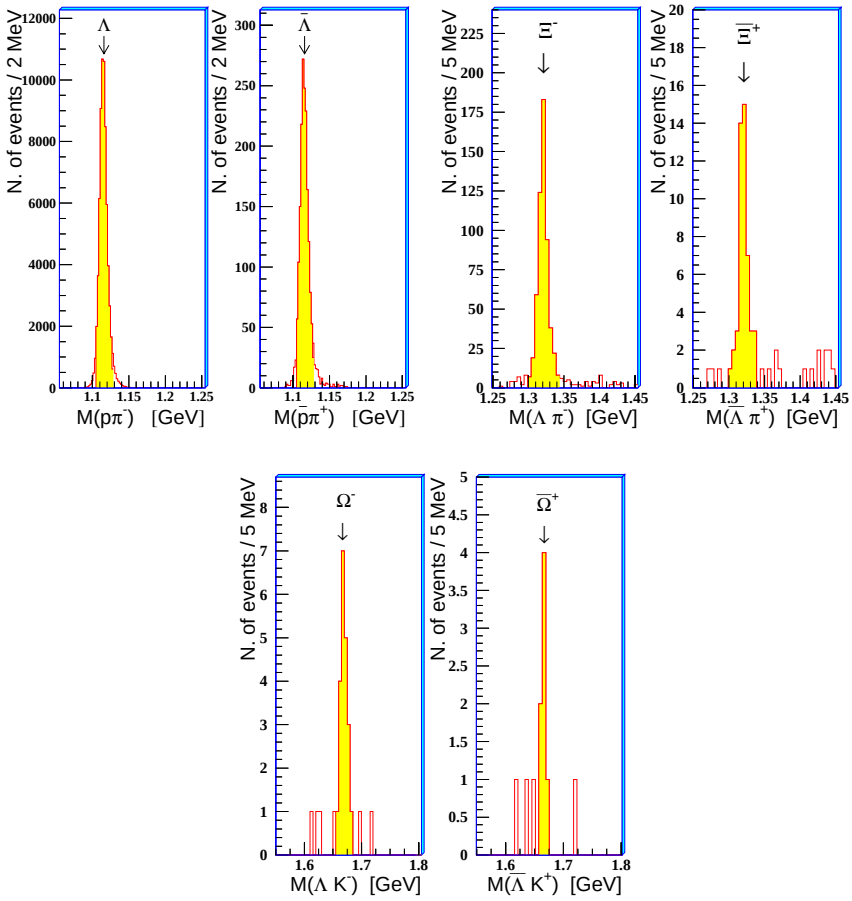

Figure 5.7: Invariant mass plots for Λ, Ξ and Ω in Pb-Pb collisions using a beam momentum of 40 A GeV/c.

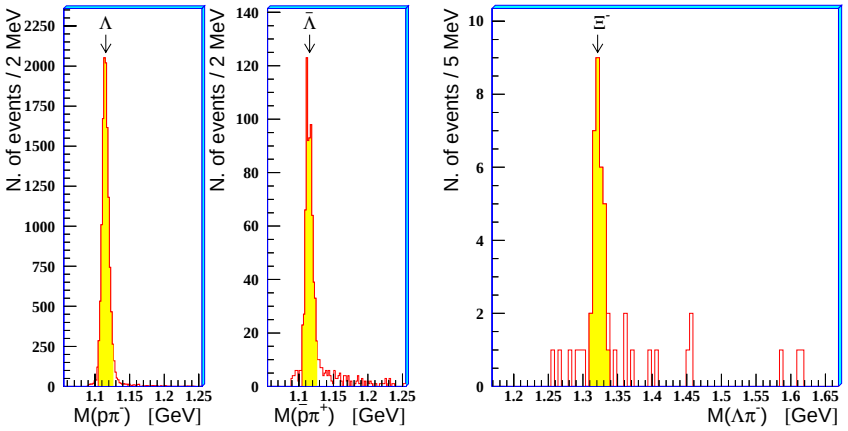

Figure 5.8: Invariant mass plots for Λ, $\overline{\Lambda}$ and Ξ^- for p-Be collisions using a beam momentum of 40 A GeV/c.

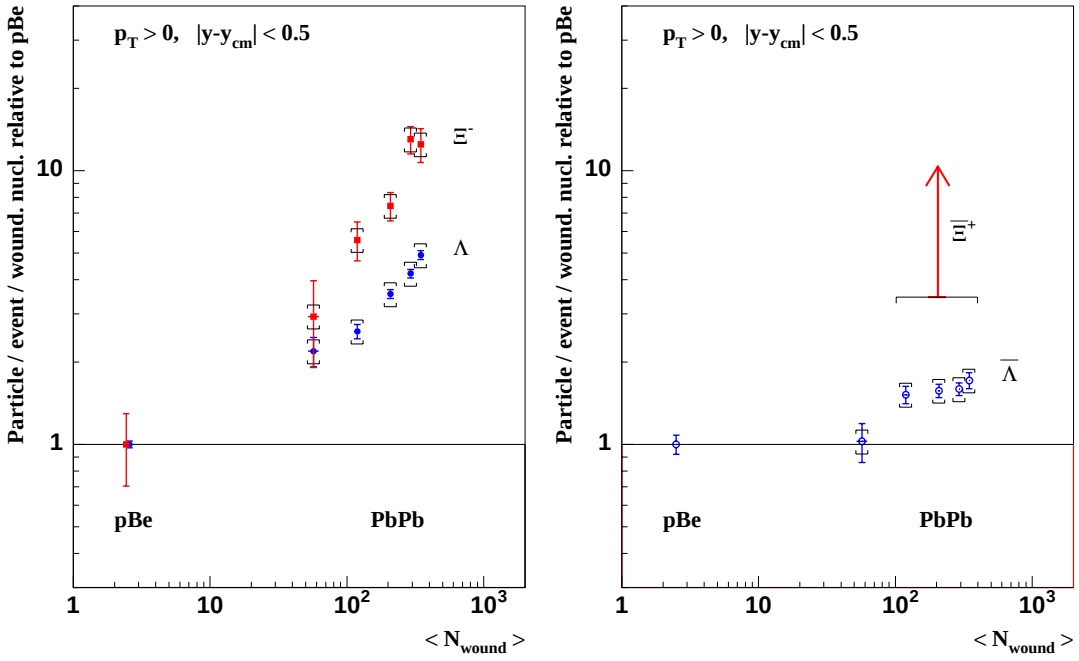

Figure 5.9: Hyperon enhancements E as a function of number of wounded nucleons at 40 A GeV/c. The lower limit on the $\overline{\Xi}^+$ enhancement in the four most central classes at a 95% confidence level is indicated.

Chapter 6

Discussion

In this chapter the WA97/NA57 results are discussed and compared to results from other experiments at the SPS and RHIC. Some recent results from NA57 on the description of the m_{T} spectra and high p_{T} suppression are included.

6.1 Energy dependence

The particle production yields found by NA57 for Pb-Pb collisions at 40 and 158 A GeV/c beam momentum are plotted in figure 6.1 together with the yields found by the STAR collaboration at RHIC. The STAR results are measured at mid-rapidity in $\sqrt{s_{NN}} =$ 130 GeV Au-Au collisions [96, 97, 98, 99]. The NA57 results are here presented in the same centrality ranges as the ones used by STAR which is the most central 6%, 5%, 10% and 11% collisions for K^0_S, Λ, Ξ and Ω respectively. This leads to rather large error bars in the $\overline{\Xi}^+$ and Ω yields from NA57. All presented yields are calculated at one unit of rapidity around the central rapidity. The Λ and Ξ^- yields do not vary much with energy, while a clear energy dependence is seen for K^0_S, $\overline{\Lambda}$, $\overline{\Xi}^+$ and $\overline{\Omega}^+$.

The antihyperon to hyperon ratios are shown in figure 6.2 for the two SPS energies and at $\sqrt{s_{NN}} = 130$ GeV at RHIC [100]. Again, there are large error bars in the $\overline{\Omega}^+/\Omega^-$ ratio because the NA57 data sample is restricted to the centrality range covered by STAR. At all three energies, the ratios increase with increasing strangeness content of the particle. The ratios also increase with increasing centrality of the collision, but the energy dependence is weaker for particles with higher strangeness content. These results are consistent with a lower baryon density at mid-rapidity with increasing energy.

Figure 6.3 shows the enhancement factors for Λ, $\overline{\Lambda}$ and Ξ^- separately, comparing the results from 40 and 158 A GeV/c measured by NA57. For the most central collisions (class 3 and 4) the enhancement factors are higher at 40 than at 158 A GeV/c, and the increase with the number of wounded nucleons is steeper at the lower energy.

STAR has also measured enhancement factors for Λ and Ξ as a function of centrality at $\sqrt{s_{NN}} = 200$ GeV [101] (see figure 6.4), similar to the WA97 and NA57 measurements at SPS energies. None of the particles show any sign of reaching a plateau at the top RHIC energy. The enhancement factors are similar to the factors measured at SPS both at 40 and at 158 A GeV/c. In statistical models including canonical suppression in small colliding systems, the strangeness enhancement is predicted to be decreasing

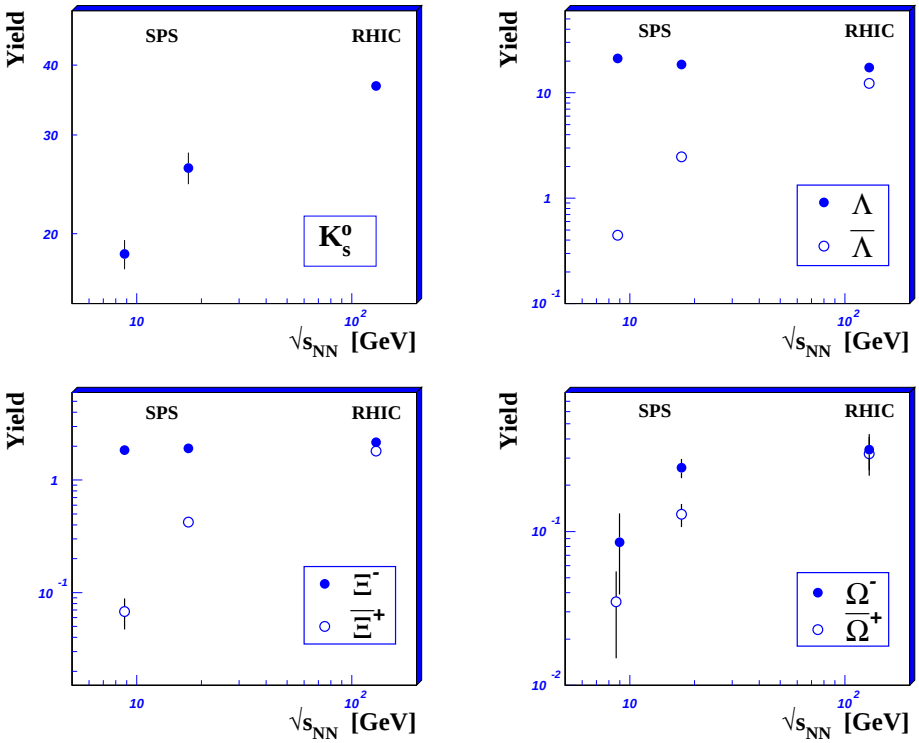

Figure 6.1: Comparison of strange particle yields at central rapidity at SPS and RHIC energies.

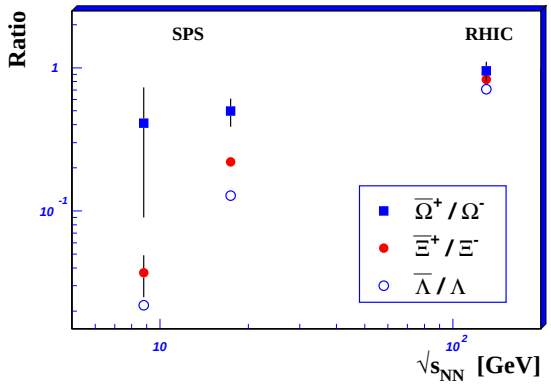

Figure 6.2: Comparison of antihyperon to hyperon ratios measured at SPS and at RHIC.

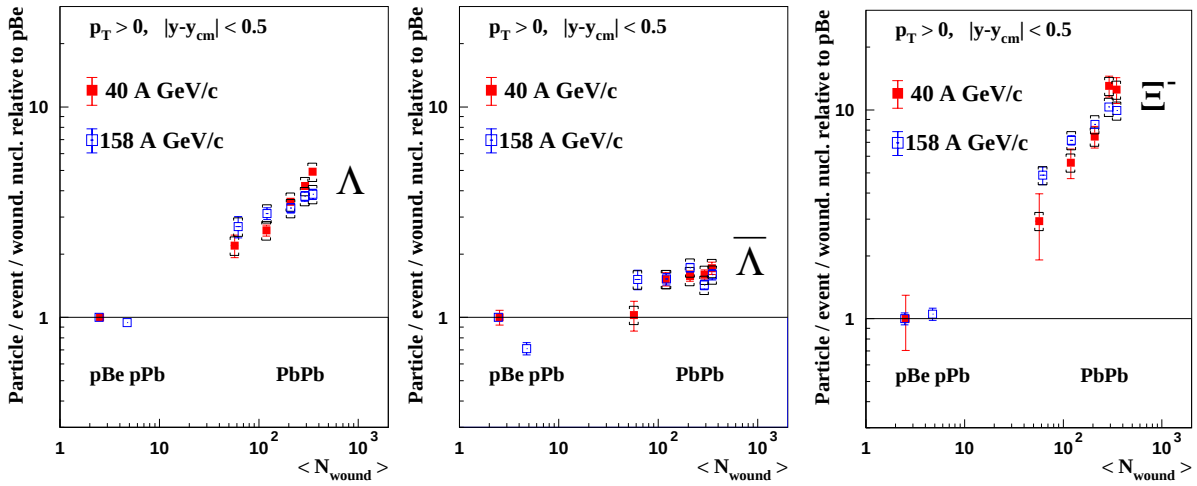

Figure 6.3: Λ, $\overline{\Lambda}$ and Ξ^- yields at 40 A GeV/c compared to yields measured at 158 A GeV/c.

with increasing collision energy, reaching a plateau at a certain energy [102]. The data are compatible with canonical suppression, but neither the plateau or the decreasing enhancement with increasing energy are seen in the data. A possible explanation is that the volume of the system is not proportional to the number of participants as assumed in the calculations.

6.2 Comparison with NA49

The hyperon yields measured by NA57 at a beam momentum of 40 and 158 A GeV/c are compared with the corresponding results from the NA49 experiment [103, 104, 105, 106, 107]. For comparison, the centrality ranges are restricted to those of NA49. The NA49 yields of K^0_S are extracted from their charged kaon yields. The comparison shows a systematic discrepancy between the two experiments. The yields measured by NA49 are found to be about 30% lower than the yields measured by NA57 at both energies [108]. The particle ratios are found to be compatible within statistical uncertainties, since the differences in the absolute yields cancel in the ratios. The differences between the two experiments are so far not understood.

6.3 Blast-wave description of the m_{T} spectra

A statistical hadronization model [14] is used to describe the m_{T} distributions (see also section 1.4.1). The model assumes a system in local thermal equilibrium that expands both in the longitudinal and in the transverse direction. By fitting the model to the experimental spectra the thermal freeze-out temperature T and the average transverse flow velocity $\langle\beta_\perp\rangle$ can be extracted. Assuming a uniform particle density, the average

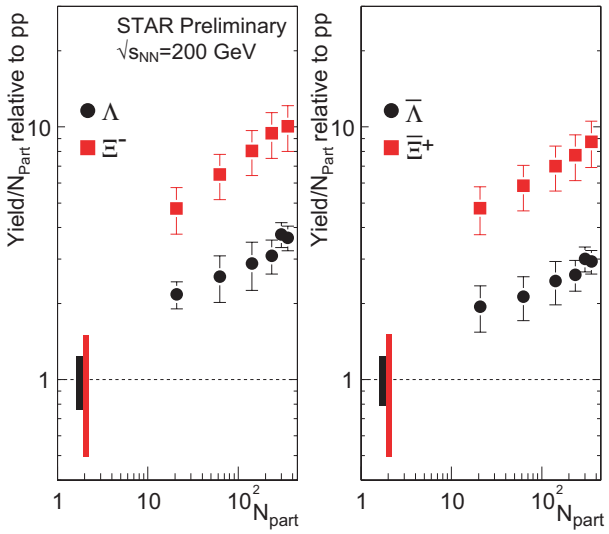

Figure 6.4: Strangeness enhancement factors as a function of number of participants measured by STAR at $\sqrt{s_{NN}} = 200$ GeV [101]. The range for the p-p results indicate the systematic uncertainty.

transverse flow velocity is given as [109]

$$\langle \beta_\perp \rangle = \frac{2}{2+n} \beta_S \tag{6.1}$$

where β_S is the is the transverse flow velocity of the surface. The model fit to the data points from all the strange particles simultaneously, using a linear ($n = 1$) r-dependence of the transverse flow velocity, is shown in figure 6.5. The model describes the experimental distributions well, with the values of T and $\langle \beta_\perp \rangle$ indicated in the figure. A detailed description of the analysis is found in [16].

Blast-wave fits for singly- and multi-strange particles separately have also been performed. The fits are shown in figure 6.6 together with the global fit. The figure shows the 1σ contours around the fitted values. Due to low statistics of the Ω it is not possible to make a separate fit on its spectrum. The $\Xi + \Omega$ contour is dominated by the Ξ and does basically not change if the Ω spectrum is removed from the fit. Therefore, it can only be concluded that the thermal freeze-out of the Ξ is compatible with that of the singly-strange particles.

A global fit to the spectra of each of the five centrality classes of NA57 is also performed. The 1σ confidence level contours of the fits are shown in figure 6.7. The general trend is that with increasing centrality, the thermal freeze-out temperature is decreasing and the average transverse flow is increasing. After a central collision, the system seems to expand explosively and then freeze out when the temperature is about 120 MeV and the average transverse flow velocity is about half the speed of light. At RHIC, PHENIX have measured the centrality dependence of the freeze-out parameters in Au-Au collisions at $\sqrt{s_{NN}} = 130$ GeV for singly-strange and non-strange particles [110]. They observe a similar centrality dependence as NA57.

Another RHIC experiment, STAR, has measured the freeze-out parameters for Ξ^-

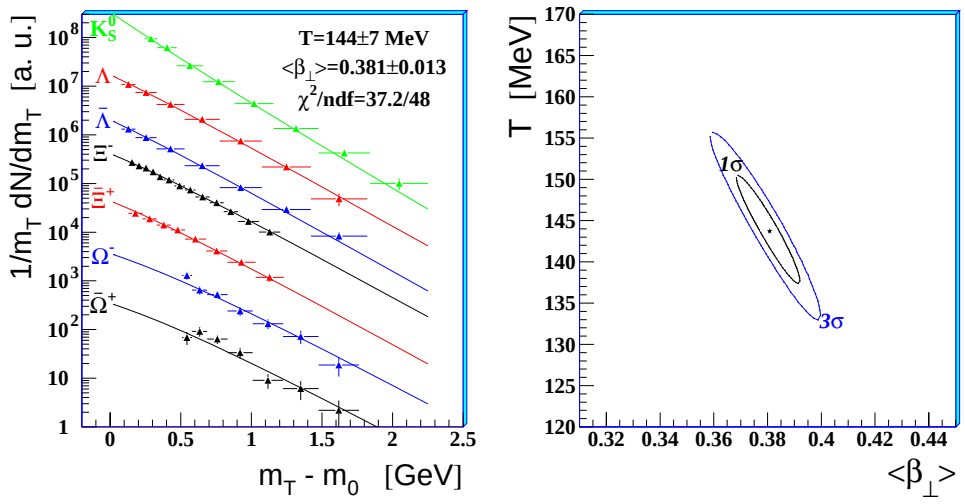

Figure 6.5: Left, transverse mass spectra at 158 A GeV/c with the fit from the blast-wave model. Right, the fit parameters with 1σ and 3σ confidence level contours.

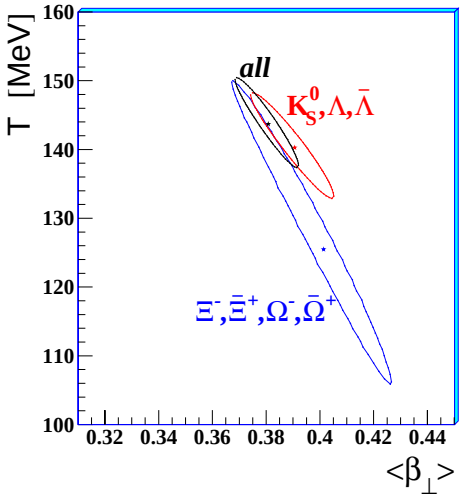

Figure 6.6: Thermal freeze-out temperature versus average transverse flow from the blast-wave fits where singly- and multi-strange particles are separated. 1σ contours are drawn around the fitted value.

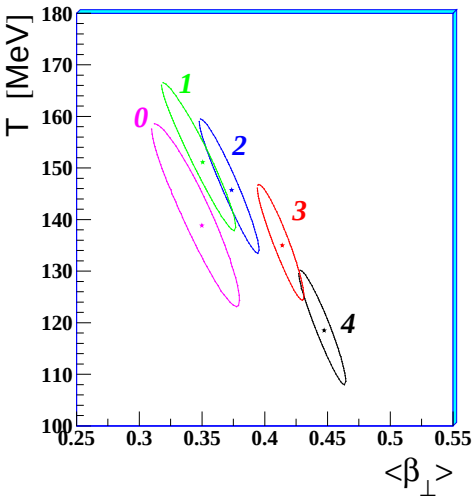

Figure 6.7: 1σ confidence level contours from blast-wave fits in each centrality class.

and $\overline{\Xi}^{+}$ for central Au-Au collisions at the same energy [111]. They find a final freeze-out temperature significantly higher than the value obtained for singly-strange and non-strange particles, and a lower transverse flow. This may indicate an earlier freeze-out of the Ξ than the singly-strange and non-strange particles at RHIC energies. They have also measured the freeze-out parameters for $\phi(s\overline{s})$ and Ω in central Au-Au collisions at $\sqrt{s_{NN}} = 200$ GeV [17] shown in figure 1.7. The observed freeze-out temperature for these particles is higher than for singly-strange and non-strange particles, indicating an earlier freeze-out of all multi-strange particles.

6.4 High p_{T} suppression

One of the main discoveries at RHIC is the high p_{T} suppression in central heavy ion collisions (see section 1.4.7). This effect is seen in the nuclear modification factor described in equation 1.13. If an AA collision is only a superposition of N_{coll} NN collisions, this leads to a nuclear modification factor $R_{AA}(p_{\mathrm{T}}) = 1$. The PHENIX [112] and STAR [113] collaborations measure a factor 4-5 suppression with respect to unity in $R_{AA}(p_{\mathrm{T}})$ for $p_{\mathrm{T}} \gtrsim 5$ GeV/c in central Au-Au collisions at $\sqrt{s_{NN}} = 200$ GeV.

A similar suppression at high p_{T} is measured for central-to-peripheral nuclear modification factors [114]. Central-to-peripheral nuclear modification factors are defined as

$$R_{CP}(p_{\mathrm{T}}) = \frac{\langle N_{coll}\rangle_P}{\langle N_{coll}\rangle_C} \times \frac{\mathrm{d}^2 N_{AA}^C/\mathrm{d}p_{\mathrm{T}}\mathrm{d}y}{\mathrm{d}^2 N_{pp}^P/\mathrm{d}p_{\mathrm{T}}\mathrm{d}y} \tag{6.2}$$

$\langle N_{coll}\rangle_P$ is the average number of NN collisions for AA collisions in centrality class P, and class P is a set of peripheral collisions that replaces the pp collisions used for reference. The suppression of high p_{T} particles is interpreted as energy loss of hard partons traversing the high-density QCD medium expected to be formed in high energy heavy ion collisions.

Nuclear modification is also measured at $\sqrt{s_{NN}} = 62.4$ GeV at RHIC. Preliminary results show an R_{AA} suppression of about a factor 3 [115, 116]. This indicates that the high p_{T} suppression at this energy is not much smaller than at $\sqrt{s_{NN}} = 200$ GeV. It is therefore interesting to look for effects of parton energy loss at even lower energies, e.g. SPS energies.

Recently, NA57 has calculated central-to-peripheral nuclear modification factors, R_{CP} for the p_{T} distributions of K^0_S, Λ, $\overline{\Lambda}$ and unidentified negatively charged particles (h^-), measured in Pb-Pb collisions at $\sqrt{s_{NN}} = 17.3$ GeV [117]. The data are divided in five centrality classes corresponding to 0-5%, 10-20%, 20-30%, 30-40% and 40-55% of the total inelastic cross section σ_{inel}^{Pb-Pb}. The number of participants, N_{part}, and the number of collisions, N_{coll}, are calculated from the Glauber model for each class. The class 40-55% of σ_{inel}^{Pb-Pb} is used as the peripheral reference class for the other 'central' classes. Figure 6.8 shows the result of this analysis. The systematic error on the $\langle N_{coll}\rangle_P/\langle N_{coll}\rangle_C$ ratio is indicated by the shaded bands around $R_{CP} = 1$. The R_{CP} values expected from scaling with the number of participants are indicated by the shaded bands at $R_{CP} < 1$. At low p_{T}, the R_{CP} for negatives, K^0_S and Λ are consistent with scaling with the number of participants. For $\overline{\Lambda}$ the ratio is found to increase even slower than the number of participants. The K^0_S R_{CP} pattern is slightly enhanced at $p_{\mathrm{T}} \gtrsim 1.2$ GeV/c in the less central classes compared to the most central one. Within errors the R_{CP} patterns for the other particles do not vary with the different centrality classes. It is also shown that the R_{CP} patterns for K^0_S, Λ and $\overline{\Lambda}$ measured at the SPS at $\sqrt{s_{NN}} = 17.3$ GeV are similar to those measured at RHIC at $\sqrt{s_{NN}} = 200$ GeV, but are moved upward by about 0.5 units [117].

Figure 6.9 shows the R_{CP} values for K^0_S measured by NA57 compared to predictions by Wang obtained from a perturbative QCD based calculation [118, 117]. The thick line shows the prediction including the in-medium parton energy loss, while the thin line shows the prediction excluding this energy loss. Without parton energy loss the 0-5%/40-55% R_{CP} is expected to increase with increasing p_{T} due to initial-state partonic intrinsic transverse momentum broadening (Cronin effect). This effect is expected to be larger for central than for peripheral collisions. Including parton energy loss, the 0-5%/40-55% R_{CP} is expected to decrease with increasing p_{T}. At this centrality class the prediction including parton energy loss describes the data better than the prediction excluding the energy loss. At less central collisions the predictions with and without energy loss are similar and both scenarios are compatible with the data.

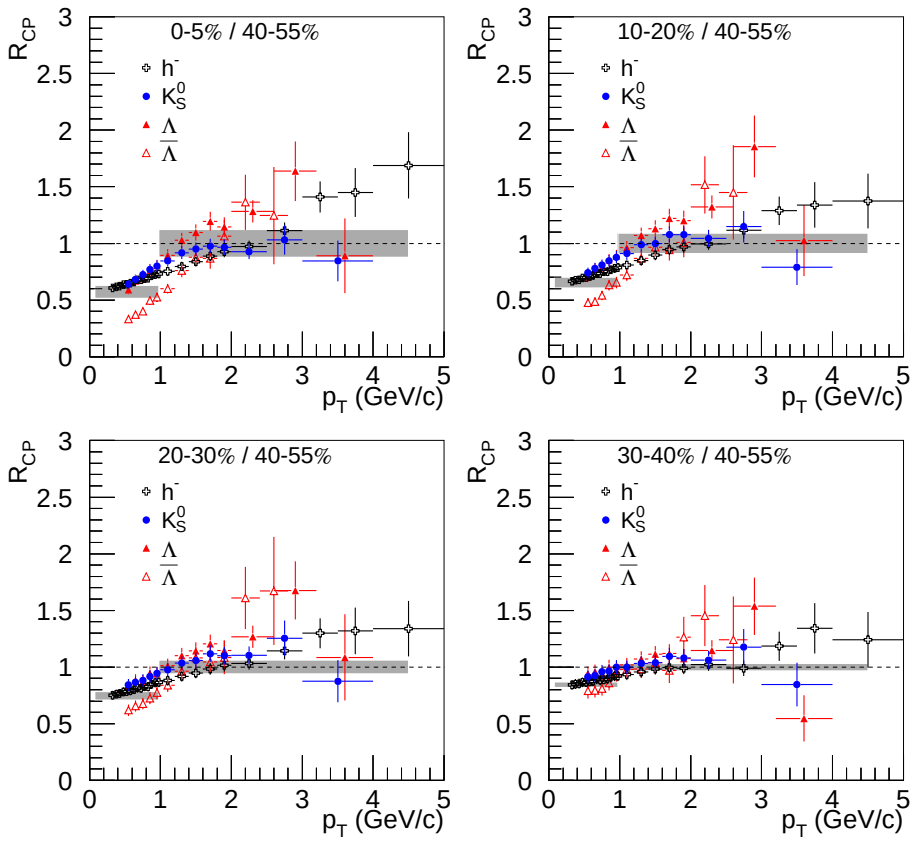

Figure 6.8: Centrality dependence of $R_{CP}(p_{\mathrm{T}})$ for h^-, K^0_S, Λ and $\overline{\Lambda}$ in Pb-Pb collisions at $\sqrt{s_{NN}} = 17.3$ GeV (158 A GeV/c beam momentum). Systematic errors on the ratio of $\langle N_{coll} \rangle$ (centred at $R_{CP} = 1$) and the values expected for scaling with the number of participants ($R_{CP} < 1$) are indicated by shaded bands.

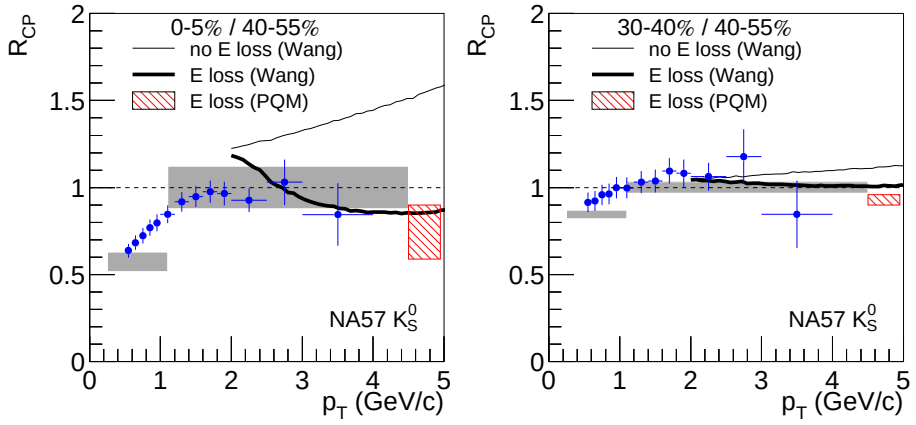

Figure 6.9: $R_{CP}(p_{\mathrm{T}})$ for K^0_S in Pb-Pb collisions at $\sqrt{s_{NN}} = 17.3$ GeV (158 A GeV/c beam momentum) compared to predictions with and without the effect of parton energy loss.

Chapter 7

Summary and outlook

7.1 Summary

The WA97 and NA57 collaborations have studied the production of strange particles, Λ, Ξ, Ω and K^0_S, in Pb-Pb, p-Pb and p-Be collisions at relativistic energies. Particle production is measured at one unit of rapidity around the central value and at high transverse momenta.

As first measured by WA97, and confirmed by NA57, strangeness production is enhanced in Pb-Pb collisions at 158 A GeV/c compared to proton induced collisions at the same beam momenta. The enhancement is increasing with the strangeness content of the particle. The largest enhancement is found for $\Omega^- + \overline{\Omega}^+$ which is enhanced by a factor 20 in the most central Pb-Pb collisions compared to p-Be collisions at 158 A GeV/c. Looking at all the five centrality classes from NA57, there is no sign of saturation in the enhancement factors when going to more central collisions, with the exception of $\overline{\Lambda}$.

The same enhancement pattern is found by NA57 in Pb-Pb collisions at 40 A GeV/c. At this energy the statistical sample is not large enough to present results from Ω^- and $\overline{\Omega}^+$. The enhancement factors for Λ and Ξ are similar to those measured at 158 A GeV/c, but show a faster increase with centrality. A comparison to STAR results at $\sqrt{s_{NN}} =$ 200 GeV shows that the enhancement factors for Λ and Ξ at this energy are similar to the SPS results. Statistical models with canonical suppression, which predicts decreasing enhancement with increasing collision energy, are quantitatively not compatible with the data. A possible explanation is that the volume of the system is not proportional to the number of participants as assumed in the calculations.

Transverse mass distributions are measured for the hyperons and K^0_S, and are presented here for the 158 A GeV/c data sample. The fitted inverse slope parameters for K^0_S and Λ fits in a picture where the inverse slope is increasing with the particle's rest mass. The Ω have a lower inverse slope parameter than expected from this picture. The hyperons are found to have similar inverse slope parameters, $T_\Omega \approx T_\Xi \approx T_\Lambda$.

The transverse mass spectra are also fitted with the blast-wave model, from which the freeze-out temperature and the average transverse flow velocity are extracted. At the top SPS energy, the common freeze-out temperature for all particles is found to be around 140 MeV and an average transverse flow around 0.4c. The temperature and transverse flow of the Ξ are found to be compatible with the parameters for the singly-strange

particles. A separate fit for the Ω is not presented due to the limited statistical sample. The average transverse flow is found to increase with increasing centrality of the collisions, while the temperature is decreasing.

Inspired by the results from RHIC, central to peripheral nuclear modification factors are measured by NA57. The R_{CP} patterns for K^0_S, Λ and $\overline{\Lambda}$ measured at the top SPS energy are found to be similar to those measured at $\sqrt{s_{NN}} = 200$ GeV at RHIC, but are shifted upward by about 0.5 units. The measured R_{CP} values for K^0_S are better described by a model including parton energy loss than the model without energy loss.

The large enhancement of Ω in Pb-Pb collisions compared to p-Be collisions is still difficult to explain by hadronic models, but fits nicely into a quark gluon plasma picture. The WA97/NA57 result therefore supports the assumption that a strongly coupled quark matter is created already at SPS energies.

7.2 Outlook

7.2.1 LHC and ALICE

In the future, relativistic heavy ion collisions will be studied at the Large Hadron Collider (LHC) at CERN in addition to the RHIC experiments. It is scheduled to start running in 2007. Nine months per year is dedicated to proton-proton collisions and one month to heavy ion runs. The first heavy ion run is scheduled in 2008.

ALICE is a general-purpose experiment optimized for heavy-ion physics. It is designed to measure and identify forward dimuons and mid-rapidity hadrons, leptons and photons that comes from the hot interaction zone. The experiment is being optimized to reconstruct tracks and identify particles in a wide range of p_{T}, from about 100 MeV/c to about 100 GeV/c. It will be possible to reconstruct short lived particles like hyperons and D mesons. Finally all track reconstruction and particle identification have to work in a high multiplicity environment with up to 8000 charged particles per unit of rapidity at mid-rapidity.

The detectors will be placed in an underground cavern about 50 metres below the ground. The experimental setup is shown in figure 7.1. The experiment consists of a central system covering mid-rapidity ($|\eta| \leq 0.9$, full azimuthal coverage) and several forward systems. The whole central system is placed inside a large solenoidal magnet with a magnetic field of ≤ 0.5 T. The magnet has a radius of 5 m, and a length of 12 m.

A detailed description of ALICE and the physics that can be studied using the experimental setup is given in [119]. In the LHC, the energy will be so high that a large amount of strange particles will be produced. This will make it possible to study strange particle spectra with small statistical errors even for relatively high transverse momenta. Simulation studies show that it will be possible to measure short lived resonances carrying strangeness, which is important when characterizing chemical equilibrium in heavy ion collisions.

At LHC energies, production of heavy quarks like charm and bottom becomes increasingly important, and will take over some of the role that strange quarks play at SPS energies.

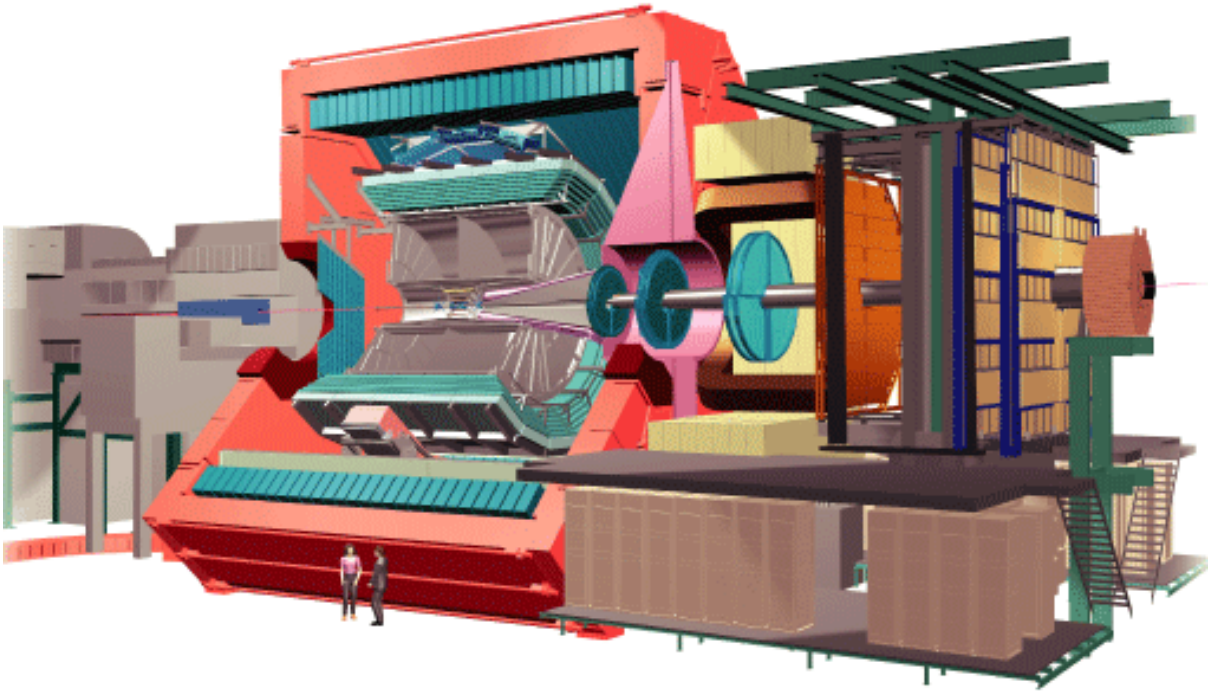

Figure 7.1: ALICE experimental setup.

Appendix A

List of publications

A.1 Publications in refereed journals

1. S. Abatzis *et al.* (WA94 Collaboration) (... K. Fanebust, 58 authors),
   Strange particle production in sulphur-sulphur interactons at 200 GeV/c per nucleon,
   Nucl. Phys. **A590** (1995) 317c

2. G. Alexeev *et al.* (WA97 Collaboration) (... K. Fanebust, 124 authors),
   First Results from the 1994 Lead Beam Run of WA97,
   Nucl. Phys. **A590** (1995) 139c

3. S. Abatzis *et al.* (WA94 Collaboration) (... K. Fanebust, 57 authors),
   A study of cascade and strange baryon production in sulphur-sulphur interactions at 200 GeV/c per nucleon,
   Phys. Lett. **B354** (1995) 178

4. H. Helstrup *et al.* (WA97 Collaboration) (... K. Fanebust, 114 authors),
   WA97 results on strangeness production in lead-lead collisions at 158 A GeV/c,
   Nucl. Phys. **A610** (1996) 165c

5. S. Abatzis *et al.* (WA94 Collaboration) (... K. Fanebust, 57 authors),
   Study of charged particle production using Omega RICH in WA94 experiment,
   Nucl. Instr. Meth. **A371** (1996) 22

6. S. Abatzis *et al.* (WA94 Collaboration) (... K. Fanebust, 59 authors),
   Hyperon Production in Proton-Sulphur Collisions at 200 GeV/c,
   Phys. Lett. **B400** (1997) 239

7. A. Andrighetto *et al.* (WA94 Collaboration) (... K. Fanebust, 55 authors),
   Charged particle production in S-S collisions at 200 GeV/c per nucleon,
   Phys. Lett. **B412** (1997) 148

8. M. Venables *et al.* (WA94 Collaboration) (... K. Fanebust, 59 authors),
   Strangeness production in the WA94 experiment at CERN,
   J. Phys. **G23** (1997) 1857

9. A. K. Holme *et al.* (WA97 Collaboration) (... K. Fanebust, 106 authors), *Production of multi-strange particles in Pb-Pb interactions at 158 A GeV/c*, J. Phys. **G23** (1997) 1851

10. E. Andersen *et al.* (WA97 Collaboration) (... K. Fanebust, 100 authors), *Λ, Ξ and Ω production in Pb-Pb collisions at 158 A GeV/c*, Nucl. Phys. **A638** (1998) 115c

11. E. Andersen *et al.* (WA97 Collaboration) (... K. Fanebust, 103 authors), *Enhancement of central Λ, Ξ and Ω yields in Pb-Pb collisions at 158 A GeV/c*, Phys. Lett. **B433** (1998) 209

12. L. Šándor *et al.* (WA97 Collaboration) (... K. Fanebust, 106 authors), *Multistrange Baryon Production in Pb-Pb and p-Pb Collisions*, Nucl. Phys. B **71** (1999) 270

13. R. Lietava *et al.* (WA97 Collaboration) (... K. Fanebust, 99 authors), *Λ, Ξ and Ω production at central rapidity in Pb-Pb and p-Pb collisions at 158 A GeV/c*, J. Phys. **G25** (1999) 181

14. R. Caliandro *et al.* (WA97 Collaboration) (... K. Fanebust, 99 authors), *K^0 and negative particle production at central rapidity in p-Pb and Pb-Pb collisions at 158 A GeV/c*, J. Phys. **G25** (1999) 171

15. D. Evans *et al.* (WA85/WA94 Collaborations) (... K. Fanebust, 60 authors), *Enhancement of strange and multi-strange hyperons and anti-hyperons in S-S and S-W interactions at 200 GeV/c*, J. Phys. **G25** (1999) 209

16. T. Virgili *et al.* (WA97 Collaboration) (... K. Fanebust, 99 authors), *Strange baryon production in p-Pb collisions at 158 A GeV/c: a comparison with VENUS model*, J. Phys. **G25** (1999) 345

17. A. Jacholkowski *et al.* (WA97 Collaboration) (... K. Fanebust, 99 authors), *Di-Lambda events in Pb-Pb collisions at 158 A GeV/c*, J. Phys. **G25** (1999) 423

18. V. Manzari *et al.* (NA57 Collaboration) (... K. Fanebust, 102 authors), *Experiment NA57 at the CERN SPS*, J. Phys. **G25** (1999) 473

19. E. Andersen *et al.* (WA97 Collaboration) (... K. Fanebust, 98 authors): *Strangeness Enhancement at mid-rapidity in Pb-Pb collisions at 158 A GeV/c*, Phys. Lett. **B449** (1999) 401

20. F. Antinori *et al.* (WA97 Collaboration) (... K. Fanebust, 50 authors),
Production of strange and multistrange hadrons in nucleus-nucleus collisions at the SPS,
Nucl. Phys. **A661** (1999) 130c

21. L. Šándor *et al.* (WA97 Collaboration) (... K. Fanebust, 50 authors),
Transverse mass spectra of strange and multiply-strange particles in Pb-Pb collisions at 158 A GeV/c,
Nucl. Phys. **A661** (1999) 481c

22. D. Elia *et al.* (WA97 Collaboration) (... K. Fanebust, 50 authors),
Hyperon and negative particle production at central rapidity in proton-Beryllium interactions at 158 GeV/c,
Nucl. Phys. **A661** (1999) 476c

23. N. Carrer *et al.* (WA97 and NA57 Collaborations) (... K. Fanebust, 94 authors),
Determination of the number of wounded nucleons in Pb+Pb collisions at 158 A GeV/c,
Nucl. Phys. **A661** (1999) 357c

24. F. Antinori *et al.* (WA97 Collaboration) (... K. Fanebust, 51 authors),
Strangeness enhancement at midrapidity in Pb-Pb collisions at 158 A GeV/c: A comparison with VENUS and RQMD models,
Eur.Phys.J. **C11** (1999) 79

25. V. Manzari *et al.* (NA57 Collaboration) (... K. Fanebust, 94 authors),
Silicon pixel detectors for tracking in NA57,
Nucl. Phys. **A661** (1999) 716c

26. D. Evans *et al.* (WA97 Collaboration) (... K. Fanebust, 50 authors),
Enhancement of Strange and Multi-Strange Baryons in Central Pb-Pb Interactions at 158 GeV/c per Nucleon,
Nucl. Phys. **A663-664** (2000) 717c

27. F. Antinori *et al.* (WA97 Collaboration) (... K. Fanebust, 50 authors),
Transverse mass spectra of strange and multiply-strange particles in Pb-Pb collisions at 158 A GeV/c,
Eur.Phys.J. **C14** (2000) 633

28. F. Antinori *et al.* (NA57 Collaboration) (... K. Fanebust, 91 authors),
Probing the specific entropy produced in ultra-relativistiv heavy-ion collisions with a silicon pixel multplicity detector: a simulation study,
Nucl. Instr. and Meth. **A452** (2000) 323

29. F. Antinori *et al.* (WA97 and NA57 Collaborations) (... K. Fanebust, 96 authors),
Determination of the number of wounded nucleons in Pb+Pb collisions at 158 A GeV/c,
Eur.Phys.J. **C18** (2000) 57

30. F. Antinori *et al.* (NA57 Collaboration) (... K. Fanebust, 106 authors), *Study of production of strange and multi-strange particles in lead-lead interactions at the CERN SPS: the NA57 experiment*, Nucl.Phys. **A681** (2001) 165c

31. R. A. Fini *et al.* (WA97 Collaboration) (... K. Fanebust, 52 authors), *Strange baryon production in Pb-Pb collisions at 158 A GeV/c*, J. Phys. **G27** (2001) 375

32. N. Carrer *et al.* (WA97 and NA57 Collaborations) (... K. Fanebust, 95 authors), *Determination of the event centrality in the WA97 and NA57 experiments*, J. Phys. **G27** (2001) 391

33. V. Manzari *et al.* (NA57 Collaboration) (... K. Fanebust, 92 authors), *Status of the NA57 experiment at CERN SPS*, J. Phys. **G27** (2001) 383

34. F. Antinori *et al.* (WA97 Collaboration) (... K. Fanebust, 49 authors), *Centrality dependence of the expansion dynamics in Pb-Pb collisions at 158 A GeV/c*, J. Phys. **G27** (2001) 2325

35. R. A. Fini *et al.* (WA97 Collaboration) (... K. Fanebust, 50 authors), *Strange particle production in p-Be, p-Pb. Pb-Pb at 158 A GeV/c (WA97 Experiment)*, Nucl. Phys. **A681** (2001) 141c

36. H. Helstrup *et al.* (WA97 Collaboration) (... K. Fanebust, 52 authors), *Multistrange baryon production in heavy ion reactions at the SPS*, Nucl. Phys. **A685** (2001) 407

37. D. Elia *et al.* (NA57 Collaboration) (... K. Fanebust, 94 authors), *Results on 40 A GeV/c Pb-Pb collisions from the NA57 experiment*, Nucl. Phys. **A715** (2003) 514c

38. P.I. Norman *et al.* (NA57 Collaboration) (... K. Fanebust, 95 authors), *Hyperon production in 40 A GeV/c collisions from the NA57 experiment*, J.Phys. **G30** (2004) S199

39. D. Elia *et al.* (NA57 Collaboration) (... K.F. Hetland, 79 authors), *Energy dependence of K^0 and hyperon production at the CERN SPS*, J.Phys. **G30** (2004) S1329

40. G.E. Bruno *et al.* (NA57 Collaboration) (... K.F. Hetland, 79 authors), *New results from the NA57 experiment*, J.Phys. **G30** (2004) S717

41. F. Antinori *et al.* (NA57 Collaboration) (... K.F. Hetland, 94 authors), *Study of the transverse mass spectra of strange particles in Pb-Pb collisions at 158*

A GeV/c,
J.Phys. **G30** (2004) 823

42. F. Antinori *et al.* (NA57 Collaboration) (... K.F. Hetland, 94 authors), *Energy dependence of hyperon production in nucleus nucleus collisions at SPS*, Phys.Lett. **B595** (2004) 68

43. F. Carminati *et al.* (ALICE Collaboration) (... K. Fanebust, 886 authors), *ALICE: Physics Performance Report, Volume I*, J.Phys. **G30** (2004) 1517

44. L. Šándor *et al.* (NA57 Collaboration) (... K. Fanebust, 95 authors), *Strange Baryon Production in Pb-Pb Interactions at the CERN SPS*, Acta Physica Polonica **B35** (2004) 197

45. D. Elia *et al.* (NA57 Collaboration) (... K. Fanebust, 93 authors), *Hyperon production in 158 and 40 A GeV/c Pb-Pb and p-Be collisions from the NA57 experiment*, Nucl. Phys. **A734** (2004) 57

46. L. Šándor *et al.* (NA57 Collaboration) (... K.F. Hetland, 94 authors): *Strangeness at NA57: Energy Dependence*, J.Phys. **G31** (2005) S919

47. D. Elia *et al.* (NA57 Collaboration) (... K.F. Hetland, 94 authors), *Strange particle production in 158 and 40 A GeV/c Pb-Pb and p-Be collisions*, J.Phys. **G31** (2005) S135

48. G.E. Bruno *et al.* (NA57 Collaboration) (... K.F. Hetland, 94 authors), *Blast-wave analysis of strange particle $m_{\rm T}$ spectra in Pb-Pb collisions at the SPS*, J.Phys. **G31** (2005) S127

49. F. Antinori *et al.* (NA57 Collaboration) (... K.F. Hetland, 94 authors), *Multiplicity of charged particles in Pb-Pb collisions at SPS energies*, J.Phys. **G31** (2005) 321

50. F. Antinori *et al.* (NA57 Collaboration) (... H.F. Hetland, 94 authors), *Central-to-peripheral nuclear modification factors in Pb-Pb collisions at* $\sqrt{s_{NN}} =$ 17.3 *GeV/c*, Phys. Lett. **B623** (2005) 17

51. F. Antinori *et al.* (NA57 Collaboration) (... K.F. Hetland, 94 authors), *Rapidity distributions around mid-rapidity of strange particles in Pb-Pb collisions at 158 A GeV/c*, J. Phys. **G31** (2005) 1345

A.2 Conference contributions

1. *Production of multi-strange particles in lead-lead interactions at 158 GeV/c per nucleon*,
   Poster presented at the Fifteenth International Conference on Ultra-Relativistic Nucleus-Nucleus Collisions (Quark Matter 2001),
   Stony Brook, USA, January 15-20, 2001

2. *First results on strange baryon production from the NA57 experiment*,
   Talk at the North-West Europe Nuclear Physics Conference,
   Bergen, Norway, April 17-20, 2001

3. *Results on hyperon production from NA57*,
   Plenary talk at the 6th International Conference on Strange Quarks in Matter,
   Frankfurt, Germany, September 24-29 2001

A.3 Publications as primary author or contributor

1. N. Carrer *et al.* (NA57 Collaboration) (... K. Fanebust, 93 authors),
   First results on strange baryon production from the NA57 experiment,
   Nucl. Phys. **A698** (2002) 118c

2. K. Fanebust *et al.* (NA57 Collaboration) (96 authors),
   Results on hyperon production from NA57,
   Proceedings following the 6th International Conference on Strange Quarks in Matter, Frankfurt, Germany, September 24-29 2001,
   J. Phys. **G28** (2002) 1607

3. V. Manzari *et al.* (NA57 Collaboration) (... K. Fanebust, 94 authors),
   Hyperon yields in Pb-Pb collisions from the NA57 experiment,
   Nucl. Phys. **A715** (2003) 140c

4. L. Šándor *et al.* (NA57 Collaboration) (... K. Fanebust, 95 authors),
   Hyperon production at the CERN SPS: results from the NA57 experiment,
   J.Phys. **G30** (2004) S129

References

[1] M. Gell-Mann, Phys. Lett. **8** (1964) 214.

[2] G. Zweig, Preprints CERN-TH 401 and 412 (1964).

[3] S. Eidelman *et al.*, Phys. Lett. **B 592** (2004) 1.

[4] N. Cabibbo and G. Parisi, Phys. Lett. **59B** (1975) 67.

[5] Z. Fodor and S. D. Katz, JHEP **03** (2002) 014.

[6] Z. Fodor and S. D. Katz, JHEP **04** (2004) 050.

[7] B. Friman, J. Phys. G: Nucl. Part. Phys. **30** (2004) S895.

[8] L. D. Landau, Izv. Akad. Nauk. SSSR **17** (1953) 51.

[9] J. D. Bjorken, Phys. Rev. **D27** (1983) 140.

[10] BRAHMS Collaboration: I.G. Bearden *et al.*, Phys. Rev. Lett. **93** (2004) 102301.

[11] H. Caines, J. Phys. G: Nucl. Part. Phys. **31** (2005) S101.

[12] R. Hagedorn, Nuovo Cimento Suppl. **3** (1965) 147.

[13] NA44 Collaboration: N. Xu *et al.*, Nucl. Phys. **A610** (1996) 175c.

[14] E. Schnedermann, J. Sollfrank, and U. Heinz, Phys. Rev. **C48** (1993) 2462.

[15] H. van Hecke, H. Sorge, and N. Xu, Phys. Rev. Lett. **81** (1998) 5764.

[16] NA57 Collaboration: F. Antinori *et al.*, J. Phys G: Nucl. Part. Phys. **30** (2004) 823.

[17] The STAR collaboration: J. Adams *et al.*, Nucl. Phys. **A 757** (2005) 102.

[18] A. M. Poskanzer and S. A. Voloshin, Phys. Rev. **C 58** (1998) 1671.

[19] L. P. Csernai and D. Röhrich, Phys. Lett **B 458** (1999) 454.

[20] The STAR collaboration: J. Adams *et al.*, Phys. Rev. Lett. **92** (2004) 062301.

[21] NA49 Collaboration: C. Alt *et al.*, Phys. Rev. **C 68** (2003) 034903.

[22] STAR Collaboration: A. H. Tang *et al.*, J. Phys. G: Nucl. Part. Phys. **31** (2005) S35.

[23] STAR Collaboration: F. Wang *et al.*, Soft physics from star, in *Proceedings of the 18th International Conference on Nucleus-Nucleus Collisions*, Budapest, Hungary, 2005.

[24] R. Stock, J. Phys. G: Nucl. Part. Phys. **30** (2004) S633.

[25] R. Hanbury-Brown and R. Q. Twiss, Phil. Mag. **45** (1954) 633.

[26] G. Goldhaber, S. Goldhaber, W. Lee, and A. Pais, Phys. Rev. **120** (1960) 300.

[27] U. Heinz and B. V. Jacak, Ann. Rev. Nucl. Part. Sci. **49** (1999) 529.

[28] G. Bertsch, M. Gong, and M. Tohyama, Phys. Rev. **C37** (1988) 1896.

[29] S. Chapman, P. Scotto, and U. Heinz, Phys. Rev. Lett. **74** (1995) 4400.

[30] The STAR collaboration: J. Adams *et al.*, Phys. Rev. **C 71** (2005) 044906.

[31] D. H. Rischke, Nucl. Phys. **A610** (1996) 88c.

[32] D. H. Rischke and M. Gyulassy, Nucl. Phys. **A608** (1996) 479.

[33] J. Rafelski and B. Müller, Phys. Rev. Lett. **48** (1982) 1066.

[34] P. Koch, B. Müller, and J. Rafelski, Phys. Rep. **142** (1986) 167.

[35] P. Braun-Munzinger, J. Stachel, and C. Wetterich, Phys. Lett. **B 596** (2004) 61.

[36] T. Biró, P. Lévai, and B. Müller, Phys. Rev. **D42** (1990) 3078.

[37] P. Braun-Munzinger, K. Redlich, and J. Stachel, Particle production in heavy ion collisions, in *Quark-Gluon Plasma 3*, p. 788, World Scientific Publishing, Singapore, 2004, Preprint: arXiv:nucl-th/0304013.

[38] F. Becattini, M. Gazdzicki, A. Keränen, J. Manninen, and R. Stock, Phys. Rev. **C 69** (2004) 024905.

[39] P. Braun-Munzinger, I. Heppe, and J. Stachel, Phys. Lett. **B 465** (1999) 15.

[40] P. Braun-Munzinger, D. Magestro, K. Redlich, and J. Stachel, Phys. Lett. **B 518** (2001) 41.

[41] H. Satz, Nucl. Phys. **A715** (2003) 3c.

[42] K. Redlich and A. Tounsi, Eur. Phys. J. **C24** (2002) 589.

[43] S. Hamieh, K. Redlich, and A. Tounsi, Phys. Lett. **B 486** (2000) 61.

[44] NA49 Collaboration: V. Friese *et al.*, J. Phys. G: Nucl. Part. Phys. **31** (2005) S911.

[45] NA49 Collaboration: M. Botje *et al.*, NA49 energy scan results for central lead-lead collisions at the CERN SPS, in *Proceedings of 39th Recontres de Moriond on QCD and High Energy Hadronic Interactions*, La Thuile, Italy, 2004, Preprint: arXiv:nucl-ex/0407004.

[46] P. Braun-Munzinger, J. Cleymans, H. Oeschler, and K. Redlich, Nucl. Phys. **A697** (2002) 902.

[47] F. Becattini, J. Cleymans, A. Keränen, E. Suhonen, and K. Redlich, Phys. Rev. **C 64** (2001) 024901.

[48] BRAHMS Collaboration: M. Murray *et al.*, J. Phys. G: Nucl. Part. Phys. **30** (2004) S1129.

[49] BRAHMS Collaboration: D. Röhrich *et al.*, J. Phys. G: Nucl. Part. Phys. **31** (2005) S659.

[50] A. Wroblewski, Acta Phys. Pol. **B16** (1985) 379.

[51] J. Cleymans and K. Redlich, Phys. Rev. Lett. **81** (1998) 5284.

[52] D. K. Srivastava, Eur. Phys. J. **C 10** (1999) 487.

[53] WA98 Collaboration: M. M. Aggarwal *et al.*, Phys. Rev. Lett. **85** (2000) 3595.

[54] PHENIX Collaboration: J. Frantz *et al.*, J. Phys. G: Nucl. Part. Phys. **30** (2004) S1003.

[55] NA38 and NA50 Collaborations: M.C. Abreu *et al.*, Eur. Phys. J. **C 14** (2000) 443.

[56] NA60 Collaboration: E. Scomparin *et al.*, NA60: dimuon and charm production in p-A and In-In collisions at the CERN SPS, in *Proceedings of the 18th International Conference on Nucleus-Nucleus Collisions*, Budapest, Hungary, 2005.

[57] CERES/NA45 Collaboration: J. P. Wessels *et al.*, Nucl. Phys. **A715** (2003) 262c.

[58] T. Matsui and H. Satz, Phys. Lett. **B178** (1986) 416.

[59] NA38 Collaboration: M.C. Abreu *et al.*, Phys. Lett. **B449** (1999) 128.

[60] NA50 Collaboration: L. Ramello *et al.*, Nucl. Phys. **A715** (2003) 251c.

[61] NA38 Collaboration: C. Baglin *et al.*, Phys. Lett. **B220** (1989) 471.

[62] NA38 Collaboration: M.C. Abreu *et al.*, Phys. Lett. **B410** (1997) 337.

[63] A. P. Kostyuk, M. I. Gorenstein, H. Stöcker, and W. Greiner, Phys. Lett. **B 531** (2002) 195.

[64] A. Capella and D. Sousa, Eur. Phys. J. **C 30** (2003) 117.

[65] PHENIX Collaboration: R. G. de Cassagnac *et al.*, J. Phys G: Nucl. Part. Phys. **30** (2004) S1341.

[66] PHENIX Collaboration: H. Büsching *et al.*, Highlights from the PHENIX experiment – part 2, in *Proceedings of the 18th International Conference on Nucleus-Nucleus Collisions*, Budapest, Hungary, 2005.

[67] X.-N. Wang and M. Gyulassy, Phys. Rev. Lett. **68** (1992) 1480.

[68] The STAR collaboration: J. Adams *et al.*, Phys. Rev. Lett. **91** (2003) 072304.

[69] PHENIX Collaboration: C. Klein-Bösing *et al.*, J. Phys. G: Nucl. Part. Phys. **30** (2004) S975.

[70] T. K. Hemmick, J. Phys. G: Nucl. Part. Phys. **30** (2004) S659.

[71] E. V. Shuryak and I. Zahed, Phys. Rev. **C 70** (2004) 021901.

[72] WA97 Collaboration: G. Alexeev *et al.*, Nucl. Phys. **A590** (1995) 139c.

[73] NA57 Collaboration: V. Manzari *et al.*, J. Phys G: Nucl. Part. Phys. **25** (1999) 473.

[74] WA85 Collaboration: S. Abatzis *et al.*, Nucl. Phys. **A590** (1995) 307c.

[75] WA94 Collaboration: S. Abatzis *et al.*, Nucl. Phys. **A590** (1995) 317c.

[76] R. Fini *et al.*, J. Phys. G: Nucl. Part. Phys. **27** (2001) 375.

[77] E. H. M. Heijne *et al.*, Nucl. Instr. and Meth. **A 349** (1994) 138.

[78] F. Antinori *et al.*, Nucl. Instr. and Meth. **A 360** (1995) 91.

[79] NA57 Collaboration: V. Manzari *et al.*, Nucl. Phys. **A661** (1999) 716c.

[80] E. H. M. Heijne *et al.*, Nucl. Instr. and Meth. **A 383** (1996) 55.

[81] ALICE DAQ group, ALICE Internal Note **2002-36** (2002).

[82] P. Norman, *Hyperon Production in p-Be Interactions at 158 GeV/*c *per Nucleon at the WA97 CERN Experiment*, PhD thesis, University of Birmingham, 2000.

[83] J. Podolanski and R. Armenteros, Phil. Mag. **45** (1954) 13.

[84] WA85 Collaboration: S. Abatzis *et al.*, Phys. Lett. **B270** (1991) 123.

[85] A. K. Holme, *Strange and non-strange baryon and antibaryon production in sulphur-tungsten and sulphur-sulphur interactions at 200 A GeV/*c, PhD thesis, University of Bergen, 1995.

[86] GEANT, http://www.cern.ch/wwwasdoc/geant_html3/geantall.html.

[87] EPIO, http://www.cern.ch/wwwasdoc/WWW/epio/epiomain/epiomain.html.

[88] A. Białas, M. Bleszyński, and W. Czyż, Nucl. Phys. **B 111** (1976) 461.

[89] WA97 Collaboration: F. Antinori *et al.*, Eur. Phys. J. **C 18** (2000) 57.

[90] K. Werner, Phys. Rep. **232** (1993) 87.

[91] WA97 Collaboration: F. Antinori *et al.*, Eur. Phys. J. **C 14** (2000) 633.

[92] WA97 Collaboration: F. Antinori *et al.*, Nucl. Phys. **A661** (1999) 130c.

[93] WA97 Collaboration: D. Elia *et al.*, Nucl. Phys. **A661** (1999) 476c.

[94] NA57 Collaboration: D. Elia *et al.*, Nucl. Phys. **A715** (2003) 514c.

[95] NA57 Collaboration: G. E. Bruno *et al.*, J.Phys.G: Nucl. Part. Phys. **30** (2004) S717.

[96] The STAR collaboration: C. Adler *et al.*, Phys. Rev. Lett. **89** (2002) 092301.

[97] The STAR collaboration: J. Adams *et al.*, Phys. Rev. Lett. **92** (2004) 182301.

[98] The STAR collaboration: C. Suire *et al.*, Nucl. Phys. **715** (2003) 470.

[99] The STAR collaboration: C. Adler *et al.*, Phys. Lett. **B 595** (2004) 143.

[100] The STAR collaboration: J. Adams *et al.*, Phys. Lett. **B 567** (2003) 167.

[101] The STAR Collaboration: R. Witt *et al.*, J. Phys. G: Nucl. Part. Phys. **31** (2004) S863.

[102] A. Tounsi, A. Mischke, and K. Redlich, Nucl. Phys. **A715** (2003) 565c.

[103] NA49 Collaboration: S. V. Afanasiev *et al.*, Phys. Rev. **C 66** (2002) 054902.

[104] NA49 Collaboration: T. Anticic *et al.*, Phys. Rev. Lett. **93** (2004) 022302.

[105] NA49 Collaboration: S. V. Afanasiev *et al.*, Phys. Lett. **B 538** (2002) 275.

[106] NA49 Collaboration: C. Meurer *et al.*, J. Phys. G: Nucl. Part. Phys. **30** (2004) S175.

[107] NA49 Collaboration: M. Mitrovski *et al.*, J. Phys. G: Nucl. Part. Phys. **30** (2004) S357.

[108] NA57 Collaboration: D. Elia *et al.*, J. Phys. G: Nucl. Part. Phys. **30** (2004) S1329.

[109] S. Esumi, S. Chapman, H. van Hecke, and N. Xu, Phys. Rev. **C 55** (1997) 2163.

[110] The PHENIX collaboration: K. Adcox *et al.*, Phys. Rev. **C 69** (2004) 024904.

[111] The STAR collaboration: J. Adams *et al.*, Phys. Rev. Lett. **92** (2004) 182301.

[112] The PHENIX collaboration: K. Adler *et al.*, Phys. Rev. **C 69** (2004) 034910.

[113] The STAR collaboration: J. Adams *et al.*, Phys. Rev. Lett. **91** (2003) 172302.

[114] The STAR collaboration: J. Adams *et al.*, Phys. Rev. Lett. **92** (2004) 052302.

[115] PHENIX Collaboration: H. Büsching *et al.*, J. Phys. G: Nucl. Part. Phys. **31** (2005) S473.

[116] J. L. Klay, J. Phys. G: Nucl. Part. Phys. **31** (2005) S451.

[117] NA57 Collaboration: F. Antinori *et al.*, Phys. Lett. **B 623** (2005) 17.

[118] X.-N. Wang, Phys. Lett. **B595** (2004) 165.

[119] ALICE Collaboration: F. Carminati *et al.*, J. Phys G: Nucl. Part. Phys. **30** (2004) 1517.